

1
2

CONNECTING OBSERVED MICROBURST PRECIPITATION WITH ITS
SCATTERING MECHANISM

3

by

Mykhaylo Sergeevich Shumko

4

A dissertation submitted in partial fulfillment
of the requirements for the degree

of

Doctor of Philosophy

in

Physics

5

MONTANA STATE UNIVERSITY
Bozeman, Montana

October 2019

6

7

©COPYRIGHT

8

by

Mykhaylo Sergeevich Shumko

2019

All Rights Reserved

DEDICATION

⁹ I dedicate this to all MSU students who use L^AT_EX. Dedication is optional
¹⁰ and may be no longer than one page, single spaced, and should precede the
¹¹ acknowledgments page.

ACKNOWLEDGEMENTS

¹² I would like acknowledge the countless engineers, technicians, and scientists who
¹³ made the FIREBIRD, AC-6, and RBSP missions a success. This work was supported
¹⁴ by Montana State University and by NASA Headquarters under the NASA Earth and
¹⁵ Space Science Fellowship Program - Grant 80NSSC18K1204. **Add co-author support.**

TABLE OF CONTENTS

16	1. INTRODUCTION	1
17	Charged Particle Motion in Electric and Magnetic Fields	2
18	Particle Populations and Their Interractions in the Magnetosphere	7
19	Populations in the Inner Magnetosphere	10
20	Plasmasphere.....	11
21	Ring Current	13
22	Radiation Belts.....	13
23	Radiation Belt Particle Sources and Sinks	17
24	Adiabatic Heating	17
25	Wave Resonance Heating	18
26	Particle Losses	21
27	Microbursts	23
28	Scope of Reserach	28
29	2. CHAPTER TWO	
30	EVIDENCE OF MICROBURSTS OBSERVED NEAR THE EQUA-	
31	TORIAL PLANE IN THE OUTER VAN ALLEN RADIATION	
32	BELT	29
33	Contribution of Authors and Co-Authors	29
34	Manuscript Information	30
35	Key Points	31
36	Abstract	31
37	Introduction	31
38	Spacecraft Instrumentation	34
39	Observations	35
40	Analysis	38
41	Microburst and Source PSD	38
42	Motion of resonant electrons in phase space	41
43	Comparing the microburst PSD to diffusion theory	44
44	Discussion and Conclusions	46
45	Acknowledgments	47
46	3. CHAPTER THREE	
47	MICROBURST SCALE SIZE DERIVED FROM MULTIPLE BOUNCES	
48	OF A MICROBURST SIMULTANEOUSLY OBSERVED WITH	
49	THE FIREBIRD-II CUBESATS	49
50	Contribution of Authors and Co-Authors	49

TABLE OF CONTENTS – CONTINUED

51	Manuscript Information	50
52	Key Points	51
53	Abstract	51
54	Introduction	52
55	Spacecraft and Observation	54
56	Analysis.....	57
57	Electron Bounce Period	58
58	Microburst Energy Spectra	60
59	Microburst Scale Sizes	60
60	Discussion and Conclusions	63
61	Acknowledgments	65
62	4. CHAPTER FOUR	
63	MICROBURST SIZE DISTRIBUTION DERIVED WITH AEROCUBE-	
64	6	66
65	Contribution of Authors and Co-Authors	66
66	Manuscript Information	67
67	Key Points	68
68	Abstract	68
69	Introduction	69
70	Instrumentation.....	72
71	Methodology	73
72	Microburst Detection.....	73
73	Microburst Size Distribution in LEO and Magnetic Equator	75
74	Modeling the Distribution of Microburst Sizes	81
75	Monte Carlo and Analytic Models to Calculate $\bar{F}(s)$	81
76	Methods for estimating optimal θ parameters.....	82
77	Estimating optimal parameters for various microburst size models.....	85
78	Discussion	87
79	Conclusions	92
80	Acknowledgments	93
82	5. CONCLUSIONS AND FUTURE WORK	94
83	Future Work.....	95
84	REFERENCES CITED.....	99

TABLE OF CONTENTS – CONTINUED

⁸⁵	APPENDIX: Appendix A.....	109
⁸⁶	APPENDIX: Appendix B.....	112
⁸⁷	APPENDIX: Appendix C.....	120

LIST OF TABLES

Table		Page
88	C.1 Range of log-normal model parameters consistent 89 with the observed AC6 $\bar{F}(s)$	123
90	C.2 Range of Weibull model parameters consistent with 91 the observed AC6 $\bar{F}(s)$	123

LIST OF FIGURES

Figure	Page
92 1.1 The three periodic motions of charged particles 93 in Earth's dipole magnetic field. These motions 94 are: gyration about the magnetic field line, bounce 95 motion between the magnetic poles, and azimuthal 96 drift around the Earth. Figure from (Baumjohann 97 and Treumann, 1997).	3
98 1.2 Charged particle motion in a uniform magnetic field 99 \vec{B} . Panel (A) shows the geometry defining the 100 pitch angle, α . Panel (B) and (C) show two helical 101 electron trajectories with dashed lines assuming a 102 large and small α (corresponding to a small and large 103 parallel velocity $v_{ }$), respectively.	6
104 1.3 Contours of constant gyration, bounce, and drift 105 frequencies for electrons and protons in a dipole field. 106 Figure from Schulz and Lanzerotti (1974).	8
107 1.4 Macroscopic structures in the inner magnetosphere 108 most relevant to this dissertation. The plasmas- 109 phere, and the radiation belts are shown and ring 110 current is co-located there as well. Figure from 111 Baumjohann and Treumann (1997).	9
112 1.5 Equipotential lines and electric field arrows due to 113 the superposition of the co-rotation and convection 114 electric fields. Electrons in the shaded region execute 115 closed orbits. Outside of the shaded regions the 116 electrons are not trapped and will escape. The 117 region separating the two regimes is called the Alfvén 118 layer. Figure from Baumjohann and Treumann (1997)....	12

LIST OF FIGURES – CONTINUED

Figure	Page
119 1.6 The DST index during the St. Patrick's Day 2015 120 storm. This storm was caused by a coronal mass 121 ejection on March 15th, 2015. The storm phases 122 are: initial phase, main phase, and recovery phase. 123 The initial phase occurred when the Dst peaked at 124 +50 nT on March 17th during which the ring current 125 was eroded by the coronal mass ejection during the 126 interval shown by the red bar. Then the rapid 127 decrease to ≈ -200 nT was during the main phase 128 where many injections from the magnetotail pumped 129 up the ring current which reduced Earth's magnetic 130 field strength at the ground and is shown with the 131 green bar. Lastly, the recovery phase lasted from 132 March 18th to approximately March 29th during 133 which the ring current particles were lost and the 134 ring current returned to its equilibrium state. The 135 recovery phase is shown with the blue bar..... 136	14
136 1.7 The two radiation belts with a the locations of 137 various satelites and orbits. Figure from (Horne 138 et al., 2013). 139	15
140 1.8 The dynamics of the outer radiation belt in 1997 141 from the POLAR satellite. Top panel shows the 1.2- 142 2.4 MeV electron flux as a function of L and 1997 day 143 of year. The middle panel shows the DST index, and 144 bottom panel shows the solar wind velocity. Figure 145 from (Reeves et al., 2003). 146	16
146 1.9 The trajectories of an electron and a right-hand cir- 147 cularly polarized wave during a cyclotron resonance. 148 The electron's $v_{ }$ and the wave's $k_{ }$ are in opposite 149 directions such that the wave's frequency is Doppler 150 shifted to a integer multiple of the electron cyclotron 151 frequency. Figure from (Tsurutani and Lakhina, 1997). 152	19

LIST OF FIGURES – CONTINUED

Figure		Page
151 152 153 154 155 156 157	1.10 Various wave modes in the magnetosphere. Ultra low frequency waves occur through the magnetosphere. Chorus waves are typically observed in the 0-12 midnight-dawn region. EMIC waves are typically observed in the dusk MLT sector. Hiss waves are observed inside the plasmasphere. Figure from Millan and Thorne (2007).....	22
158 159 160 161 162 163 164	1.11 An example train of microbursts observed by FIREBIRD-II unit 4 on February 2nd, 2015. The colored curves show the differential energy channel count rates in six channels from ≈ 200 keV to greater than 1 MeV. The x-axis labels show auxiliary information such as time of observation and the spacecraft position in L, MLT, latitude and longitude coordinates.	25
165 166 167 168 169 170 171	1.12 Relativistic ($> 1\text{MeV}$) distribution of microburst occurrence rates as a function of L and MLT. The three panels show the microburst occurrence rate dependence on geomagnetic activity, parameterized by the auroral electrojet (AE) index for (a) $\text{AE} < 100$ nT, (b) $100 < \text{AE} < 300$ nT and (c) $\text{AE} > 300$ nT. Figure from Douma et al. (2017).....	26

LIST OF FIGURES – CONTINUED

Figure	Page
172 2.1 Electron and wave conditions from the MagEIS-A 173 and EMFISIS WFR sensors for the microburst time 174 interval. Panels (a), (b), and (c) are from RBSP-A 175 with its position information annotated in panel (a). 176 Panels (d), (e), and (f) are from RBSP-B with its 177 position information annotated in panel (d). Panel 178 (a) is the MagEIS-A high rate timeseries. Panels (b) 179 and (e) show the evolution of the MagEIS-A J as a 180 function of α_L from the ~ 40 to ~ 60 keV channel. 181 Every 10th point is shown in panel (b). The solid 182 black line in panels (a) and (b) mark the end of 183 the time period used for the PSD fit extrapolation 184 analysis explained in section 3. The dashed black 185 lines in panels (a) and (b) show the time interval 186 used for the observed microburst PSD. Panels (c) 187 and (f) show the EMFISIS WFR spectra, with the 188 available burst data superposed. The red, green, and 189 cyan traces are equatorial f_{ce0} , $f_{ce0}/2$, and $f_{ce0}/10$, 190 respectively.	37
191 2.2 Panel (a) shows the MagEIS-A high rate timeseries. 192 Panel (b) shows the RBSPICE EBR count rate 193 timeseries for $\gtrsim 19$ keV electrons. The microbursts 194 were observed between 11:17:10 - 11:17:12 UT and 195 are indicated with the vertical black arrows in panels 196 (a) and (b) for MagEIS-A times. Panel (c) shows the 197 RBSPICE EBR (family of relatively sparse sampled 198 curves) and MagEIS-A J from the 29-41 keV energy 199 channel (single curve) as a function of α_L . The 200 vertical dashed lines show the time interval for the 201 PSD analysis.....	39

LIST OF FIGURES – CONTINUED

Figure	Page
202 2.3 The colored annulus represents $f(p_\perp, p_\parallel)$ in normalized momentum space, parallel and perpendicular 203 to the background magnetic field. The microburst 204 $f(p_\perp, p_\parallel)$ is highlighted with the white circle. The 205 columns show different powers of the sine extrapolation, 206 and rows show the different magnetic latitudes 207 of the scattering. The white dotted traces represent 208 the boundary between the data and extrapolation. 209 The green, red, and white solid traces are the 210 resonance curves for $\omega = 0.2\Omega_{ce}$, $0.4\Omega_{ce}$, $0.6\Omega_{ce}$, 211 respectively. The cyan dashed traces are the diffusion 212 curves for a $\omega = 0.4\Omega_{ce}$ wave (waves of 213 other frequency have similar diffusion curves). The 214 magnetic latitude of the scattering, the ratio of the 215 plasma to the cyclotron frequency, and the power 216 of the sine extrapolation is annotated in each panel. 217 For the resonance and diffusion curves, the density 218 model assumed a $n_L = 1 e^-/cm^3$ and $\psi = -1$	42
220 3.1 HiRes data of the microburst observed at February 221 2nd, 2015 at 06:12:53 UT, smoothed with a 150 ms 222 rolling average. The subsequent bounces showed 223 some energy dispersion. As discussed in Appendix 224 B, a time correction of -2.28 s was applied to FU3. 225 While the flux from five energy channels is shown, 226 only channels with reasonable counting statistics 227 were used for the spatial scale analysis. Vertical 228 colored bars show the \sqrt{N} error every 10th data 229 point and vertical black bars are lined up with the 230 peaks in the 220-283 keV energy channel to help 231 identify dispersion.	56

LIST OF FIGURES – CONTINUED

Figure	Page
232 3.2 Observed and theoretical t_b for electrons of energies 233 from 200 to 770 keV. The solid black line is t_b 234 in a dipole magnetic field, derived in Schulz and 235 Lanzerotti (1974). The red dotted and cyan dashed 236 lines are the t_b derived using the T89, and T04 237 magnetic field models with IRBEM-Lib. Lastly, 238 the blue dot-dash curve is the t_b derived using the 239 Olson & Pfitzer Quiet model. The green and purple 240 rectangles represent the observed t_b for FU3 and 241 FU4 using a Gaussian fit, respectively. The blue 242 rectangles represent the observed t_b calculated with 243 the minima between the bounces. The width of the 244 boxes represent the width of those energy channels, 245 and the height represents the uncertainty from the fit.....	59
246 3.3 The topology of the FIREBIRD-II orbit and the 247 multiple bounces of the microburst projected onto 248 latitude and longitude with axis scaled to equal 249 distance. Attributes relating to FU3 shown in red 250 dashed lines, and FU4 with blue solid lines. The 251 spacecraft path is shown with the diagonal lines, 252 starting at the upper right corner. The labels P1- 253 4 for FU4 and P1-5 for FU3 indicate where the 254 spacecraft were when the N^{th} peak was seen in 255 the lowest energy channel in the HiRes data. The 256 stars with the accompanying energy labels represent 257 the locations of the electrons with that energy that 258 started at time of P1, and were seen at the last peak 259 on each spacecraft. The rectangles represent the 260 lower bound of the microburst scale size, assuming 261 that the majority of the electrons were in the upper 262 boundary of energy channel 4.....	62
263 4.1 AC6 mission properties for (a) spacecraft separation 264 and (b) number of simultaneous quality 10 Hz 265 samples as a function of L and MLT.....	73

LIST OF FIGURES – CONTINUED

Figure	Page
266 4.2 Examples of > 35 keV microbursts observed simultaneously by AC6-A in red and AC6-B in blue. Panels 267 (a), (c), (e), and (g) show the temporally-aligned 268 time series when AC6 were separated by $s = 5$, 269 16, 37, and 69 km, respectively. The corresponding 270 panels (b), (d), (f), and (h) show the spatially- 271 aligned time series which is made by shifting the 272 AC6-A time series in the above panels by the in- 273 track lag (annotated with dt) that show any spatially 274 correlated structures. The clear temporal correla- 275 tion and lack of spatial correlation demonstrates that 276 these events are microbursts.	76
278 4.3 Microburst size distribution in low Earth orbit. 279 Panel (a) shows the percent of microbursts observed 280 above that separation after normalizing for the 281 uneven AC6 sampling in separation. Panel (b) shows 282 the microburst probability density (size histogram) 283 as a function of separation. Lastly, panel (c) shows 284 the normalization, i.e. number of simultaneous 285 samples AC6 observed as a function of separation. 286 The colored lines show the distributions binned by 287 L, and the thick black curve for the entire radiation 288 belt ($4 < L < 8$). The gray shading around the 289 black curve shows the uncertainty due to counting 290 statistics.	79
291 4.4 Microburst size distribution mapped to the magnetic 292 equator in the same format as Fig. 4.3.	80

LIST OF FIGURES – CONTINUED

Figure	Page
293 4.5 Panels A-C show the varying geometries of the 294 analytic model. The two spacecraft are shown 295 as black dots. The enclosing black circle around 296 each spacecraft bounds the area where a microburst 297 will be observed by one or both AC6 units if the 298 microburst's center lies inside the circle. Panel 299 (A) shows the case where microburst diameter is 300 smaller than the AC6 separation and all microbursts 301 will be observed by either unit A or B and never 302 simultaneously. Panel (B) shows the intermediate 303 case where the microburst diameter is comparable to 304 the AC6 separation and some fraction of microbursts 305 will be observed simultaneously. The fraction of the 306 microbursts simultaneously observed is proportional 307 to the circle intersection area $A(r, s)$ and is shown 308 with grey shading. Panel (C) shows the case where 309 the microburst diameter is much larger than the 310 spacecraft separation and nearly all microbursts will 311 be observed by both spacecraft. Lastly panel (D) 312 shows $\bar{F}(s)$ from the AC6 data with a solid black 313 line, and modeled MC and analytic $\bar{F}(s)$ curves for 314 a single-sized microburst distribution with $d = 40$ km.....	83
315 4.6 Range of plausible microburst sizes assuming all 316 microbursts are one fixed size. Panel (a) shows the 317 posterior probability density function of microburst 318 diameters in black. The red, green, and blue vertical 319 lines at 38, 73, and 129 km represent the 2.5, 50, and 320 97.5 posterior percentiles, respectively. A uniform 321 prior between 0 and 200 km was assumed for this 322 MCMC run and is shown in cyan. Panel (b) shows 323 the percent of microbursts observed above an AC6 324 separation for $4 < L < 8$ in black. The 2.5, 50 325 and 97.5 size percentiles were estimated from the 326 posterior and plotted in red, green, and blue curves, 327 respectively.	88

LIST OF FIGURES – CONTINUED

Figure	Page
328 4.7 Plausible microburst percent curves assuming mi- 329 croburst size distribution is bimodal consisting of 330 two sizes d_0 and d_1 with a mixing term that quanti- 331 fies the relative occurrence of the d_0 to d_1 microburst 332 populations. Panel (a) shows the posterior distri- 333 bution for the microburst population mixing term, 334 a with a median value of 0.02. The a prior was 335 uniform between 0 and 0.2. Panel (b) shows the 336 posterior distribution for d_0 , the larger microburst 337 population estimated with a uniform prior between 338 50 and 200 km and the posterior median diameter of 339 122 km. Panel (c) shows the posterior distribution 340 for d_1 , the smaller microburst population, estimated 341 using a uniform prior between 0 and 50 km with a 342 median diameter of 28 km. Panel (d) is similar to 343 Fig. 4.6b and shows the AC6 microburst fraction for 344 $4 < L < 8$ in black. A set of 1000 random parameter 345 triples (a , d_0 , and d_1) were drawn from the posterior 346 and used to generate a family of $\bar{F}(s)$ curves. At 347 each s the range of consistent $\bar{F}(s)$ were quantified 348 by the 2.5, 50 and 97.5 percentiles and shown with 349 the red, green, and blue curves, respectively.	89
350 A.1 Panel (A) shows the magnetic power spectral density 351 as a function of frequency and time from the EMFI- 352 SIS WFR instrument on board RBSP-A. The “hiss- 353 like” wave used for the resonant diffusion analysis 354 was observed starting at 11:17:03 UT. In the same 355 format as panel (A), panel (B) shows the polar angle 356 of the wave vector for this time period. The wave 357 of interest had a normal wave vector, $\theta_k < 30^\circ$. 358 Since the results in panel (B) are valid only for high 359 planarity, panel (C) shows planarity in the same 360 format as panels (A) and (B). The wave of interest 361 was found to have a planarity of > 0.8 . Lastly, panel 362 (D) shows the available burst mode data.	110

LIST OF FIGURES – CONTINUED

Figure	Page
363 A.2 Ratio of the RBSPICE EBR at microburst times 364 indicated with the black vertical arrows in Fig. 2, 365 to the EBR at the same pitch angles one spin prior 366 (quiet time). The microburst flux was enhanced by 367 10-80% across $100^\circ < \alpha_L < 160^\circ$ PA, and appear to 368 be peaked closer to $\alpha_L = 90^\circ$	111
369 B.1 Cross-correlation time lag analysis applied to a train 370 of microbursts. Panel (a) and (b) show the count 371 rate from the lowest energy channel. Panel (c) shows 372 the cross-correlation coefficient as a function of time 373 lag. Panel (d) shows the shifted timeseries. Clock 374 difference was 2.23 s	114
375 B.2 Same analysis as Fig. B.1 on a different time period. 376 Clock difference was 2.21 s.....	115
377 B.3 Same analysis as Fig. B.1 on a different time period. 378 Clock difference was 2.25 s.....	116
379 B.4 Same analysis as Fig. B.1 on a different time period. 380 Clock difference was 2.27 s.....	117
381 B.5 Same cross-correlation time lag analysis applied to 382 stationary spatial structures. The cross-correlation 383 lag between these events is a sum of the clock differ- 384 ence and time lag due to the spacecraft separation. 385 The lag derived at this time was 4.95 s	118
386 B.6 Same analysis as Fig. B.5 applied to a different 387 stationary spatial feature. The lag derived at this 388 time was 5.01 s	119

NOMENCLATURE

L	L-Shell
MLT	magnetic local time
λ	magnetic latitude
α	pitch angle
α_L	local pitch angle at the spacecraft
α_{eq}	pitch angle maped to the magnetic equator
c	speed of light
R_E	Earth's radius
J	flux
f	phase space density
E	energy
E_0	exponential e-folding energy
p	momentum
\vec{E}	electric field
\vec{B}	magnetic field
B_w	wave amplitude
v	velocity
Ω_e	electron gyrofrequency
ω_{pe}	plasma frequency
k	wave vector
D_{xx}	diffusion coefficient
s	spacecraft separation
t_b	electron bounce period

389

390

INTRODUCTION

391 Above Earth's atmosphere are the a pair of Van Allen radiation belts, a complex
392 and dynamic plasma environment that affects our technology-driven society. These
393 effects include: a higher radiation dose for astronauts and cosmonauts, higher chance
394 of spacecraft failure due to single event upsets that can lead to catastrophic latchups,
395 degradation of silicon (changing the silicon doping) from an extended radiation dose
396 that can degrade a transistor to the point where it no longer function as a switch,
397 and the degradation of the ozone layer due to the chemical production of NO_X and
398 HO_X molecules. With these effects in mind, it is no surprise that the radiation belts
399 have been extensively studied since their discovery in the 1960s.

400 One natural phenomenon in the radiation belts that has been a topic of interest
401 in the space physics community is wave-particle interactions that, as we will explore
402 throughout this dissertation, can accelerate particles to very high energies (e.g. \approx
403 MeV for electrons) and scatter them into the atmosphere.

404 The goal of this dissertation is to study the wave-particle scattering mechanism
405 that scatters electron microbursts. Electron microbursts, henceforth referred to
406 as microbursts, are typically observed by low Earth orbiting spacecraft, sounding
407 rockets, and high altitude balloons as a sub-second impulse of electrons. Some of
408 the most intense microbursts are observed as a 10 to 100 fold increase of electrons
409 (for example see Fig. 7 in Blake et al. (1996)). Since they were first reported by
410 Anderson and Milton (1964), the short microburst duration and their impulsive nature
411 have compelled countless researchers to understand their properties and the physical
412 mechanism(s) that create microbursts. Microbursts are widely believed to be created

413 by wave-particle scattering between a plasma wave called whistler mode chorus
 414 and outer radiation belt electrons, although many details regarding the scattering
 415 mechanism are unconstrained or unknown.

416 This chapter serves as an introduction to the physics of charged particles, plasma
 417 waves, and the wave-particle interactions in Earth's magnetosphere. We will first
 418 derive the motion of individual charged particles in Earth's electric and magnetic
 419 fields. Then we will cover how various groups of charged particles coalesce to form
 420 the major particle populations in the magnetosphere. Then, we will cover the various
 421 mechanisms that accelerate particles in the magnetosphere. Lastly, we will review
 422 the basics of microbursts as a jumping-off point for the rest of the dissertation.

423 Charged Particle Motion in Electric and Magnetic Fields

A charged particle trapped in the magnetosphere will experience three types of periodic motion in Earth's nearly dipolar magnetic field. The three motions are ultimately due to the Lorentz force that a particle of momentum \vec{p} , charge q , and velocity \vec{v} experiences in an electric field \vec{E} and magnetic field \vec{B} and is given by

$$\frac{d\vec{p}}{dt} = q(\vec{E} + \vec{v} \times \vec{B}). \quad (1.1)$$

424 In the magnetosphere, the three periodic motions, in decreasing frequency, are
 425 gyration, bounce, and drift and are schematically shown in Fig. 1.1. Each of periodic
 426 these motions have a corresponding conserved quantity i.e. an adiabatic invariant.

The highest frequency periodic motion is gyration about a magnetic field of magnitude B . This motion is circular with a Larmor radius of

$$r = \frac{mv_{\perp}}{|q|B} \quad (1.2)$$

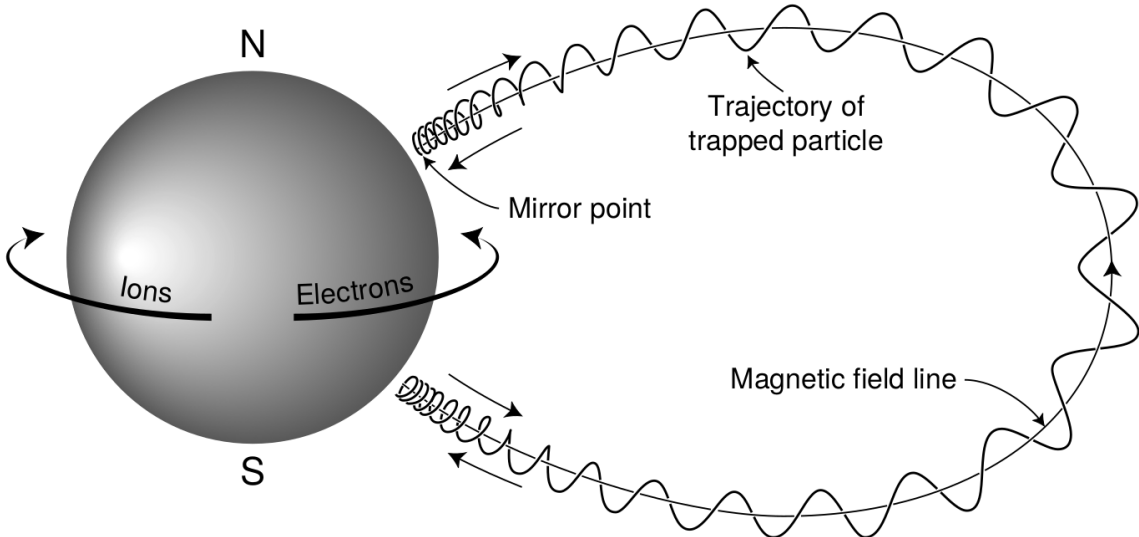


Figure 1.1: The three periodic motions of charged particles in Earth's dipole magnetic field. These motions are: gyration about the magnetic field line, bounce motion between the magnetic poles, and azimuthal drift around the Earth. Figure from (Baumjohann and Treumann, 1997).

where m is the mass and v_{\perp} the particle's velocity perpendicular to \vec{B} . This motion has a corresponding gyrofrequency

$$\Omega = \frac{|q|B}{m} \quad (1.3)$$

in units of radians/second. Inside the radiation belts the electron gyrofrequency, Ω_e is on the order of a kHz. The corresponding adiabatic invariant is found by integrating the particle's canonical momentum around the particle's path of gyration

$$J_i = \oint (\vec{p} + q\vec{A}) \cdot d\vec{l} \quad (1.4)$$

427 where J_i is the i^{th} adiabatic invariant and \vec{A} is the magnetic vector potential. This
428 integral is carried out by integrating the first term over the circumference of the gyro
429 orbit and integrating the second term using Stokes theorem to calculate the magnetic

430 flux enclosed by the gyro orbit. The gyration invariant is then $J_1 \sim v_{\perp}^2/B$, which is
 431 conserved when the frequency, ω of a force acting on the gyrating electron satisfies
 432 $\omega \ll \Omega_e$.

433 The second highest frequency periodic motion is bouncing due to a parallel
 434 gradient in \vec{B} . This periodic motion naturally arises in the magnetosphere because
 435 Earth's magnetic field is stronger near the poles, and artificially in the laboratory
 436 in magnetic bottle machines. To understand this motion we first we need to define
 437 the concept of pitch angle α as the angle between \vec{B} and \vec{v} which is schematically
 438 shown in Fig. 1.2a. The pitch angle relates v with v_{\perp} , and v_{\parallel} (the component of the
 439 particles velocity parallel to \vec{B}). As shown in 1.2b and c, a smaller (larger) α will
 440 increase (decrease) the distance that the charged particle travels parallel to \vec{B} , during
 441 one gyration.

Assuming the particle's kinetic energy is conserved, the conservation of J_1
 implies that given a particle's $v_{\perp}(0)$ and $B(0)$ at the magnetic equator (where Earth's
 magnetic field is usually at a minimum), we can calculate its $v_{\perp}(s)$ along the particle's
 path s by calculating $B(s)$ from magnetic field models. The particle's perpendicular
 velocity is then related via

$$\frac{v_{\perp}^2(0)}{B(0)} = \frac{v_{\perp}^2(s)}{B(s)} \quad (1.5)$$

442 which can be rewritten as

$$\frac{v^2 \sin^2 \alpha(0)}{B(0)} = \frac{v^2 - v_{\parallel}^2(s)}{B(s)} \quad (1.6)$$

443 and re-arranged to solve for $v_{\parallel}(s)$

$$v_{\parallel}(s) = v \sqrt{1 - \frac{B(s)}{B(0)} \sin^2 \alpha(0)} \quad (1.7)$$

⁴⁴⁴ which will tend towards 0 when the second term in the radical approaches 1.

⁴⁴⁵ The location where $v_{||}(s) = 0$ is called the mirror point and is where a particle
⁴⁴⁶ reverses direction. Since Earth's magnetic field is stronger towards the poles, the
⁴⁴⁷ mirroring particle will execute periodic bounce motion between its two mirror points
⁴⁴⁸ in the northern and southern hemispheres. The corresponding adiabatic invariant, J_2
⁴⁴⁹ is

$$J_2 = \oint p_{||} ds \quad (1.8)$$

where ds describes the particle path between the mirror points in the northern and southern hemispheres (see Fig. 1.1). J_2 is found by substituting Eq. 1.7 into Eq. 1.8 and defining the magnetic field strength at the mirror points as B_m where $\alpha(m) = 90^\circ$. The J_2 integral can be written as

$$J_2 = 2p \int_{m_n}^{m_s} \sqrt{1 - \frac{B(s)}{B(m)}} ds \quad (1.9)$$

⁴⁵⁰ where m_n and m_s are the northern and southern mirror points, respectively. The
⁴⁵¹ bounce period can be estimated (e.g. Baumjohann and Treumann, 1997) to be

$$t_b \approx \frac{LR_e}{\sqrt{W/m}} (3.7 - 1.6 \sin \alpha(0)) \quad (1.10)$$

⁴⁵² where L is the L -shell which describes the distance from the Earth's center to the
⁴⁵³ location where a particular magnetic field line crosses the magnetic equator, in units
⁴⁵⁴ of Earth radii, R_e . W is the particle's kinetic energy. As with gyration, the particle
⁴⁵⁵ will bounce between the mirror points as long as $\omega \ll \Omega_b$, where Ω_b is the bounce
⁴⁵⁶ frequency.

⁴⁵⁷ At this stage it is instructional to introduce the notion of the loss cone pitch

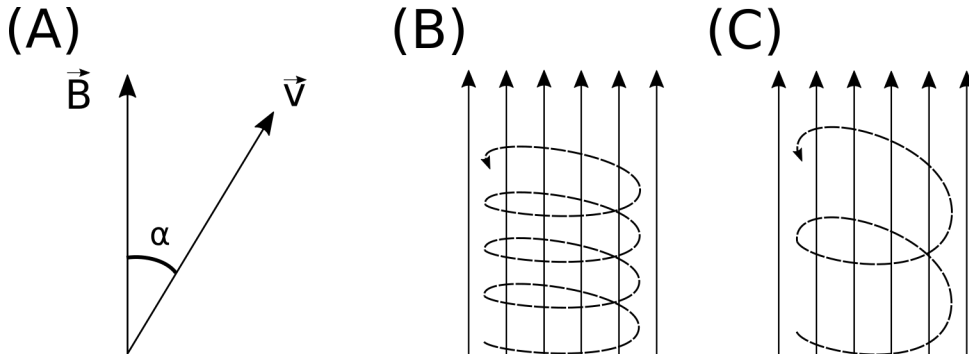


Figure 1.2: Charged particle motion in a uniform magnetic field \vec{B} . Panel (A) shows the geometry defining the pitch angle, α . Panel (B) and (C) show two helical electron trajectories with dashed lines assuming a large and small α (corresponding to a small and large parallel velocity $v_{||}$), respectively.

angle, α_L . A particle with $\alpha \leq \alpha_L$ will mirror at or below ≈ 100 km altitude in the atmosphere. A charged particle gyrating at those altitudes will encounter and Coulomb scatter with the dense atmosphere and be lost from the magnetosphere.

The slowest periodic motion experienced by charged particles in Earth's magnetic field is azimuthal drift around the Earth. This drift results from a combination of a radial gradient in \vec{B} and the curvature of the magnetic field. The radial gradient drift arises because Earth's magnetic field is stronger near the Earth where the particle's gyroradius radius of curvature is smaller as it gyrates towards stronger magnetic field, and larger when it gyrates outward. The overall effect is the particle gyro orbit does not close on itself and negatively charged particles drift east and positively charged particles drift west. The radial gradient drift is enhanced by the centrifugal force that a particle experiences as it bounces along the curved field lines. The drift adiabatic invariant, J_3 is found by integrating Eq. 1.4 over the complete particle orbit around the Earth. The shape of this drift orbit is otherwise known as a drift shell. For J_3 , the first term is negligible and the second term is the magnetic flux enclosed by the drift shell, Φ_m i.e. $J_3 \sim \Phi_m$.

₄₇₄ Figure 1.3 from Schulz and Lanzerotti (1974) shows contours of the gyration,
₄₇₅ bounce, and drift frequencies for electrons and protons in Earth's dipole magnetic
₄₇₆ field.

Up until now we have considered the three periodic motions due Earth's magnetic field and the absence of electric fields. If \vec{E} is present, a particle's center of gyration i.e., averaged position of the particle over a gyration, will drift with a velocity perpendicular to both \vec{E} and \vec{B} . The drift velocity can be solved directly from Eq. 1.1 and is

$$\vec{v}_E = \frac{\vec{E} \times \vec{B}}{B^2}. \quad (1.11)$$

₄₇₇ Lastly, for more detailed derivations of these motions, see the following texts:
₄₇₈ Baumjohann and Treumann (1997); Schulz and Lanzerotti (1974); Tsurutani and
₄₇₉ Lakhina (1997).

480 Particle Populations and Their Interractions in the Magnetosphere

₄₈₁ Now that we have looked at the dynamics of single-particle motion in electric
₄₈₂ and magnetic fields, we will briefly tour the various macroscopic populations in the
₄₈₃ magnetosphere that are illustrated in Fig. 1.4.

₄₈₄ The sun and its solar wind are ultimately the source of energy input into the
₄₈₅ magnetosphere. The solar wind at Earth's orbit is a plasma traveling at supersonic
₄₈₆ speeds with an embedded interplanetary magnetic field (IMF). When the solar wind
₄₈₇ encounters Earth's magnetic field, the plasma can not easily penetrate into the
₄₈₈ magnetosphere because the plasma is frozen-in on magnetic field lines. Thus the
₄₈₉ plasma and its magnetic field drapes around the magnetosphere forming a cavity in
₄₉₀ the solar wind that is roughly shaped as shown in Fig. 1.4. Because the solar wind
₄₉₁ is supersonic at 1 AU, a bow shock exists upstream of the magnetosphere. The solar

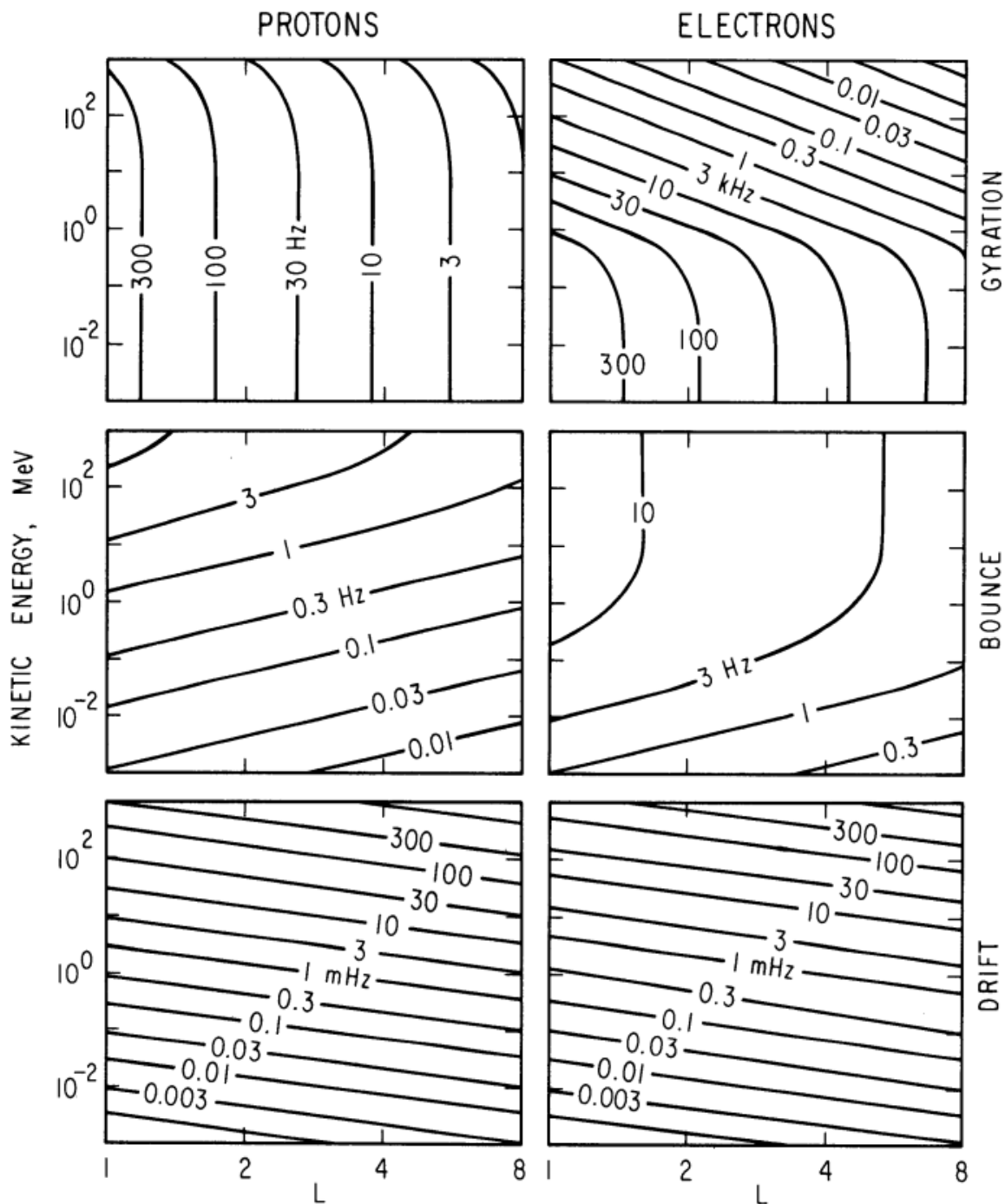


Figure 1.3: Contours of constant gyration, bounce, and drift frequencies for electrons and protons in a dipole field. Figure from Schulz and Lanzerotti (1974).

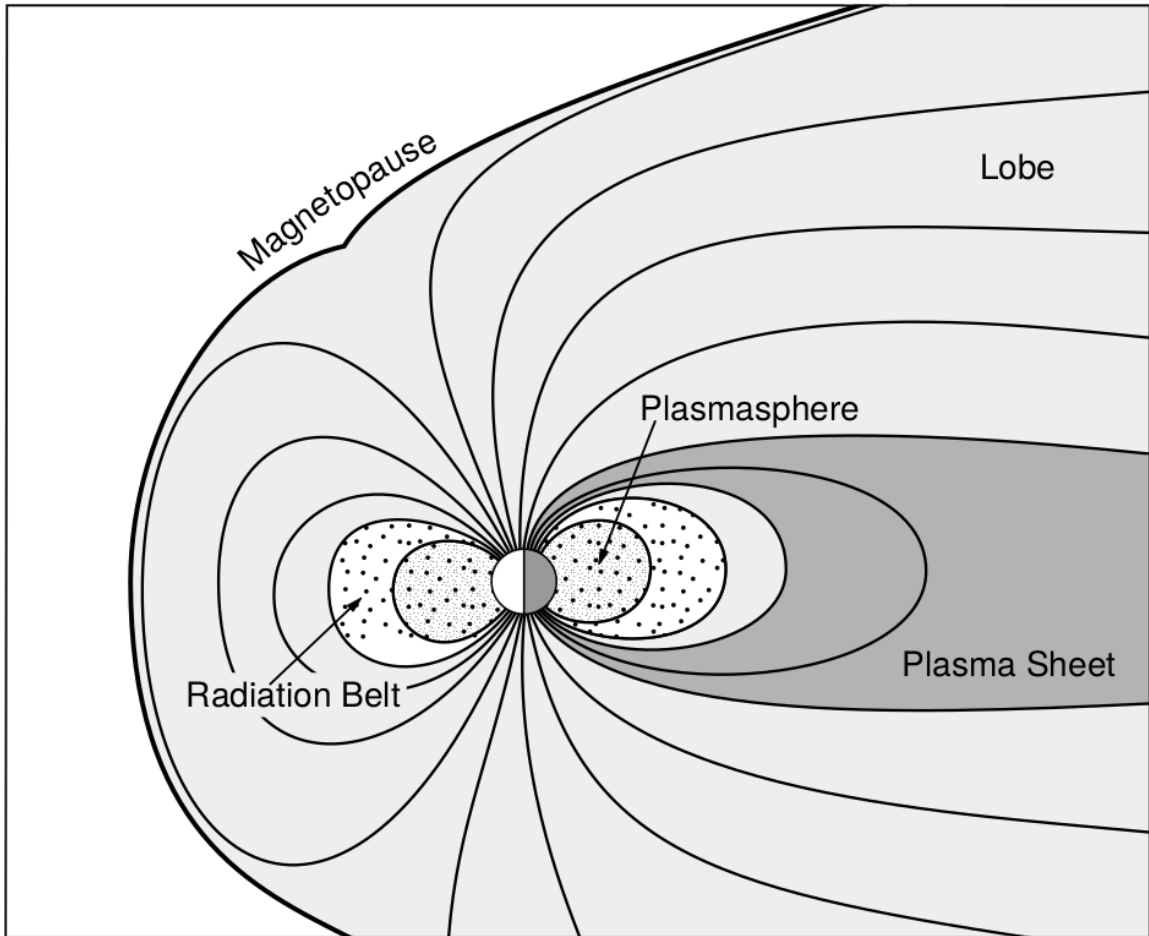


Figure 1.4: Macroscopic structures in the inner magnetosphere most relevant to this dissertation. The plasmasphere, and the radiation belts are shown and ring current is co-located there as well. Figure from Baumjohann and Treumann (1997).

492 wind plasma, after it is shocked by the bow shock, flows around the magnetosphere
 493 inside the magnetosheath. The surface where the solar wind ram pressure and Earth's
 494 magnetic pressure balance is termed the magnetopause, which can be thought of as
 495 a boundary between the solar wind's and Earth's plasma environments. This is
 496 a slightly naive description of the magnetopause, but is nonetheless an instructive
 497 conceptual picture. The shocked plasma then flows past the Earth where it shapes
 498 the magnetotail. In the magnetotail the solar wind magnetic pressure balances Earth's
 499 magnetic field pressure in the lobes. The magnetotail extends on the order of 100
 500 R_E downstream of Earth, and the tailward stretching of magnetic field lines creates
 501 the plasma sheet which exists in the region of low magnetic field strength near the
 502 magnetic equator (e.g. Eastwood et al., 2015).

503 Populations in the Inner Magnetosphere

504 Closer to Earth, where the magnetic field is largely dipolar, are three plasma
 505 populations that comprise the inner magnetosphere: the plasmasphere, the ring
 506 current, and the radiation belts. Before we describe these three particle populations
 507 in detail, we will first introduce the coordinate system that most naturally describes
 508 the inner magnetosphere environment, and the electric fields that affect mostly low
 509 energy particles.

510 In this coordinate system the “radial” coordinate was defined in section 1 and
 511 is the L shell. The azimuthal coordinate is the magnetic local time (MLT). For an
 512 observer above Earth's north pole looking down, MLT is defined to be 0 (midnight)
 513 in the anti-sunward direction, and increases in the counter-clockwise direction with 6
 514 at dawn, 12 at noon (sunward direction), and 18 in dusk. The final coordinate is the
 515 magnetic latitude, λ which is analogous to the latitude coordinate in the spherical
 516 coordinate system, and is defined to be 0 at the magnetic equator. This coordinate

517 system naturally describes the following inner magnetosphere populations.

518 The low energy particle dynamics in the inner magnetosphere are organized by
 519 two electric fields: the co-rotation and the dawn-dusk electric fields. The co-rotation
 520 electric field arises from the rotation of Earth's magnetic field. Since particles are
 521 frozen on magnetic field lines and the plasma conductivity is effectively infinite, to a
 522 non-rotating observer, Earth's rotation appears as a radial electric field that drops off
 523 as $\sim L^2$. This electric field makes particles orbit around the Earth due to the $\vec{E} \times \vec{B}$
 524 drift. The other electric field, pointing from dawn to dusk is called the convection
 525 electric field and is due to the Earthward transport of particles from the magnetotail
 526 that appears as an electric field to a stationary observer (with respect to Earth). The
 527 superposition of the co-rotation and convection electric fields results in a potential
 528 field shown in Fig. 1.5. The shaded area in Fig. 1.5 shows the orbits on which low
 529 energy electrons are trapped, and outside are the untrapped particles. The dynamic
 530 topology of the shaded region in Fig. 1.5 is controlled by only the convection electric
 531 field which is dependent on the solar wind speed and the IMF. The lowest energy
 532 particles, that are most effected by these electric fields, make up the plasmasphere.

533 Plasmasphere The plasmasphere is a dense ($n_e \sim 10^3/\text{cm}^3$), cool plasma
 534 ($\sim \text{eV}$) that extends to $L \sim 4$ (extent is highly dependent on the solar wind and
 535 magnetospheric conditions) and is sourced from the ionosphere. The two main
 536 mechanisms that source the cold plasma from the ionosphere are ultraviolet ionization
 537 by sunlight and particle precipitation. The ultraviolet ionization by sunlight is
 538 strongly dependent on the time of day (day vs night), latitude (more ionization near
 539 the equator). The ionization due to particle precipitation, on the other hand, is highly
 540 dependent on magnetospheric conditions, and mostly occurs at high latitudes.

541 The outer boundary of the plasmasphere is the plasmapause which is typically

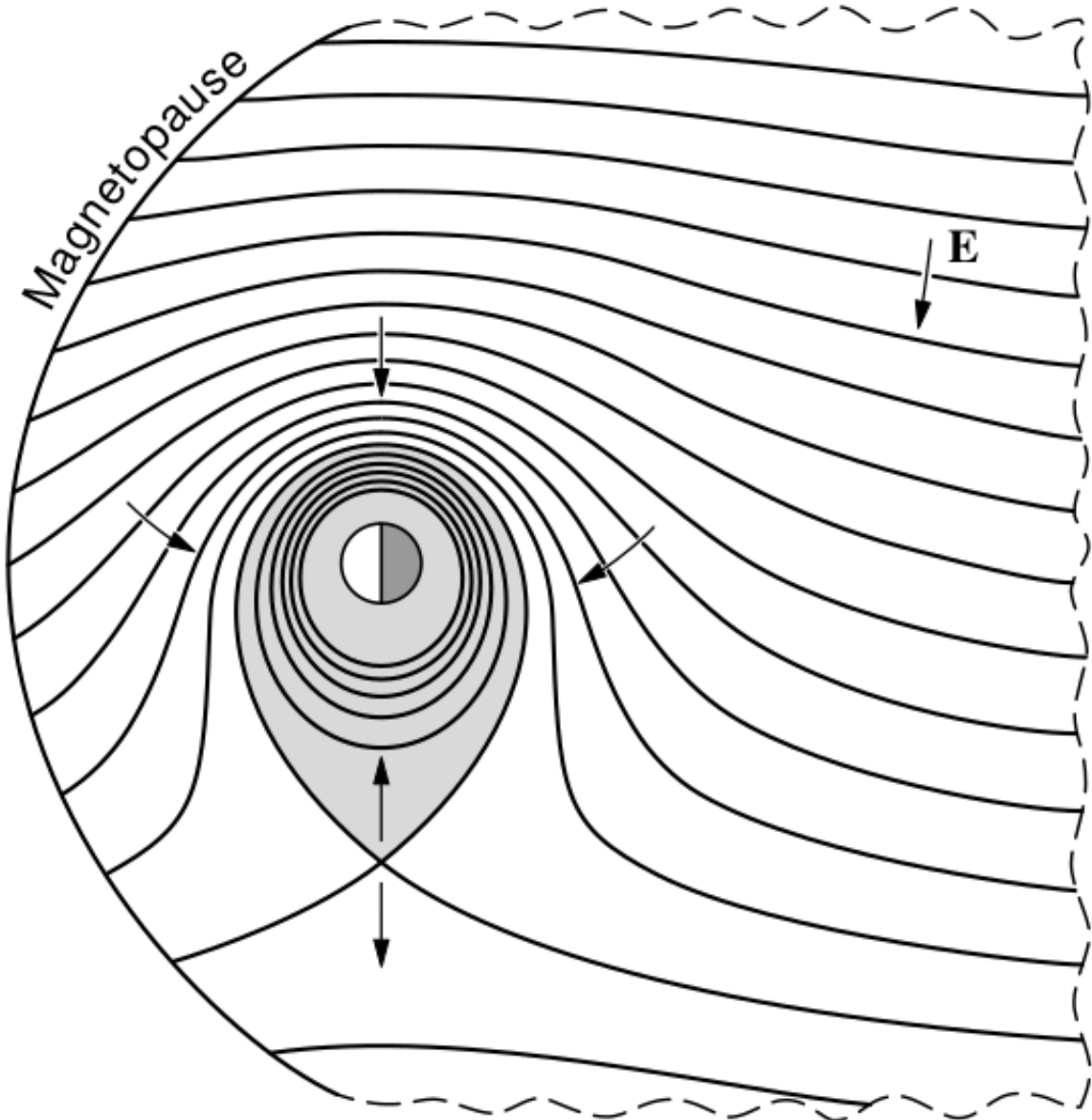


Figure 1.5: Equipotential lines and electric field arrows due to the superposition of the co-rotation and convection electric fields. Electrons in the shaded region execute closed orbits. Outside of the shaded regions the electrons are not trapped and will escape. The region separating the two regimes is called the Alfvén layer. Figure from Baumjohann and Treumann (1997).

542 identified as a steep radial gradient in plasma density from $\sim 10^3/\text{cm}^3$ to $\sim 1/\text{cm}^3$. As
 543 we will see throughout this dissertation, the location of the plasmapause is important
 544 to model (e.g. O'Brien and Moldwin, 2003) and understand since the plasma density
 545 strongly controls the efficiency of particle scattering (Horne et al., 2005).

546 Ring Current The next higher energy population is the ring current. This
 547 population consists of protons and electrons between tens and a few hundred keV
 548 that drift around the Earth. The orbits of higher energy particles are not as effected
 549 by the convection and co-rotation electric field, rather they drift around the Earth
 550 due to gradient and curvature drifts. Since the direction of the drift is dependent on
 551 charge, protons drift west around the Earth and electrons drift East. This has the
 552 effect of creating a current around the Earth.

553 The ring current generates a magnetic field which decreases the magnetic field
 554 strength on Earth's surface and increases it outside of the ring current. The decrease
 555 of Earth's magnetic field strength is readily observed by a system of ground-based
 556 magnetometers and is merged into a Disturbance Storm Time (DST) index. An
 557 example of a DST index time series from a coronal mass ejection (CME) driven 2015
 558 St. Patrick's Day storm is shown in Fig. 1.6. The ring current is sometimes first
 559 depleted and DST increases slightly (initial phase or sudden storm commencement).
 560 Then the ring current is rapidly built up during which DST rapidly decreases (main
 561 phase). Lastly the ring current gradually decays toward its equilibrium state over a
 562 period of a few days and DST increases towards 0 (recovery phase). The DST index
 563 along with other indicies are readily used by the space physics community to quantify
 564 the global state of the magnetosphere.

565 Radiation Belts The highest energy particle populations are in the Van Allen
 566 radiation belts. These belts were discovered by Van Allen (1959) and Vernov and

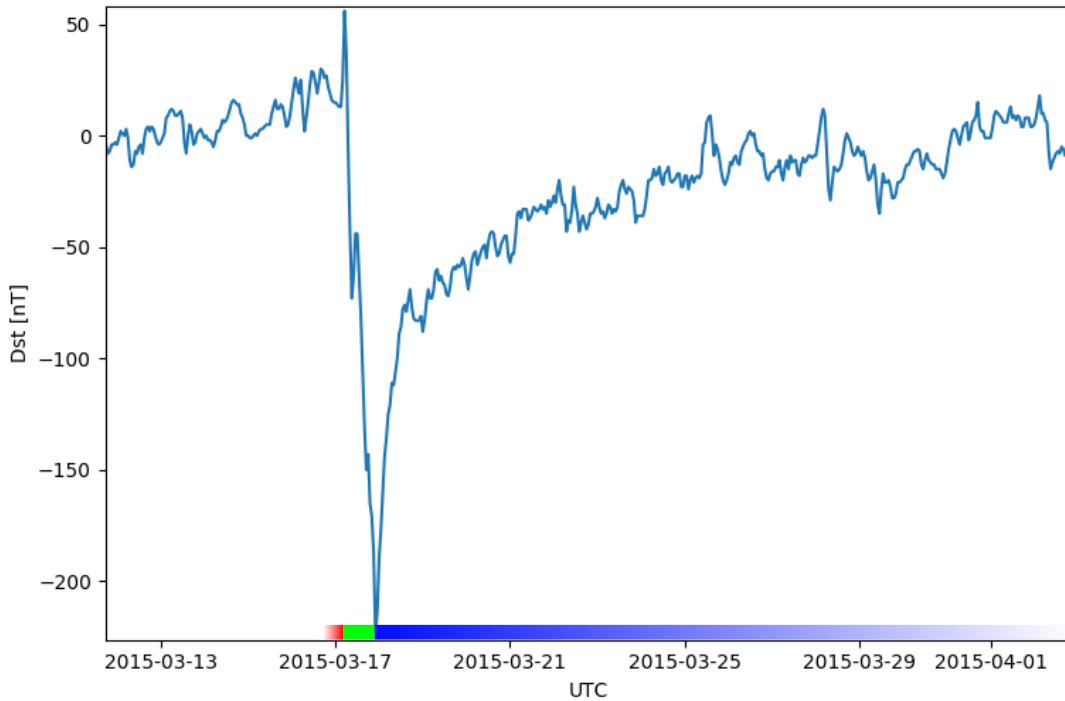


Figure 1.6: The DST index during the St. Patrick's Day 2015 storm. This storm was caused by a coronal mass ejection on March 15th, 2015. The storm phases are: initial phase, main phase, and recovery phase. The initial phase occurred when the Dst peaked at $+50$ nT on March 17th during which the ring current was eroded by the coronal mass ejection during the interval shown by the red bar. Then the rapid decrease to ≈ -200 nT was during the main phase where many injections from the magnetotail pumped up the ring current which reduced Earth's magnetic field strength at the ground and is shown with the green bar. Lastly, the recovery phase lasted from March 18th to approximately March 29th during which the ring current particles were lost and the ring current returned to its equilibrium state. The recovery phase is shown with the blue bar.

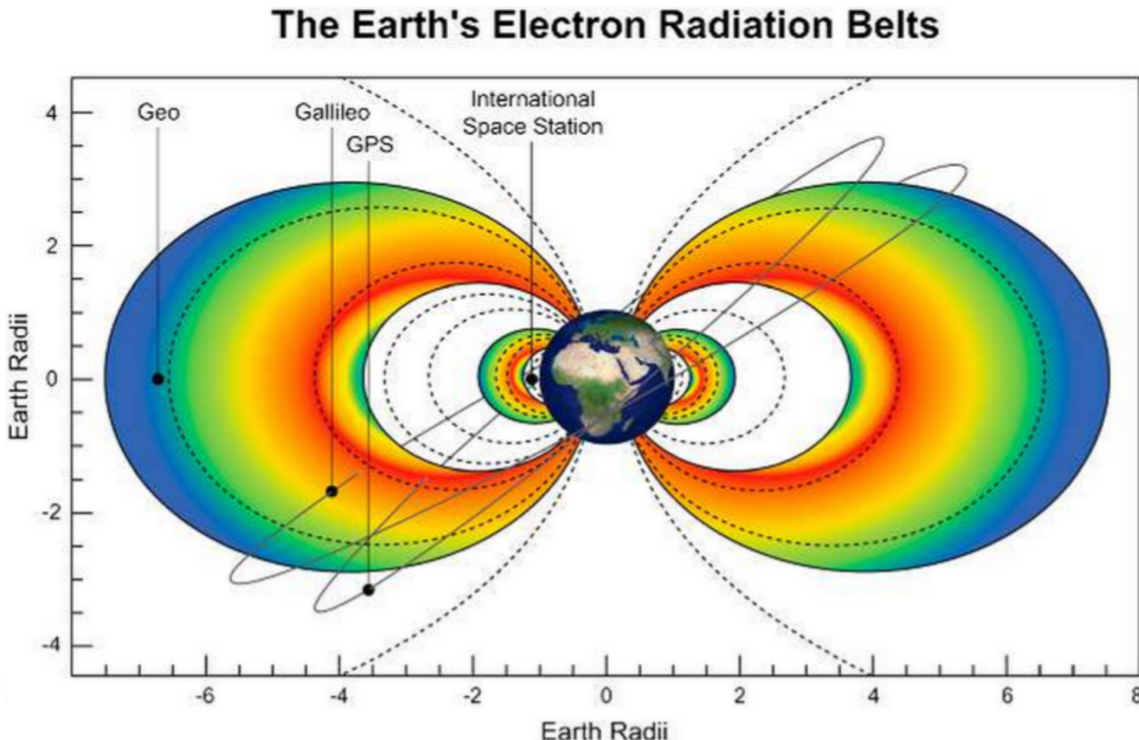


Figure 1.7: The two radiation belts with the locations of various satellites and orbits. Figure from (Horne et al., 2013).

567 Chudakov (1960) during the Cold War and are a pair of toroidally shaped populations
 568 of trapped electrons and protons usually within $L < 8$ and are shown in Fig. 1.7.
 569 Their quiescent toroidal shape is similar to the shape of the plasmasphere and ring
 570 current and is a result of Earth's dipole magnetic field and the conservation of the
 571 three adiabatic invariants discussed in section 1.

572 The inner radiation belt is extremely stable on time periods of years, extends
 573 to $L \approx 2$, and mainly consists of protons with energies between MeV and GeV and
 574 electrons with energies up to ≈ 1 MeV (Claudepierre et al., 2019). The source of inner
 575 radiation belt protons is believed to be due to cosmic-ray albedo neutron decay (e.g.
 576 Li et al., 2017) and inward radial diffusion for electrons (e.g. O'Brien et al., 2016a).
 577 The gap between the inner and outer radiation belt is called the slot, which is believed

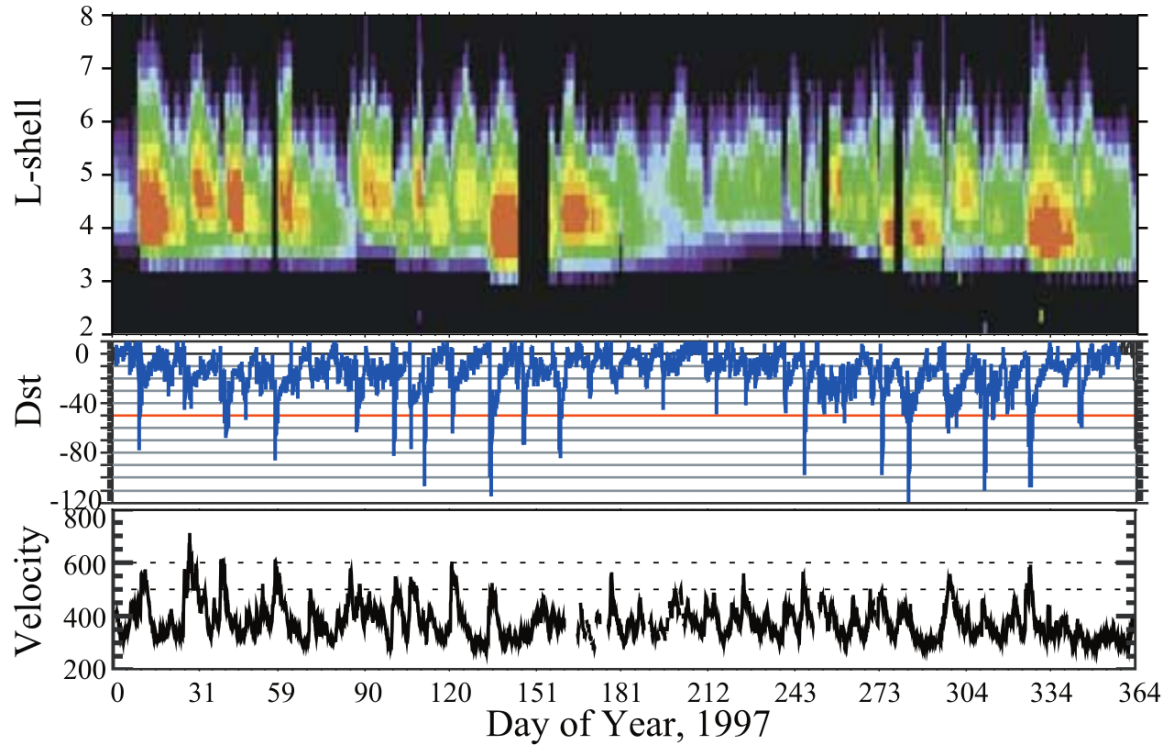


Figure 1.8: The dynamics of the outer radiation belt in 1997 from the POLAR satellite. Top panel shows the 1.2-2.4 MeV electron flux as a function of L and 1997 day of year. The middle panel shows the DST index, and bottom panel shows the solar wind velocity. Figure from (Reeves et al., 2003).

578 to be due to hiss waves inside the plasmasphere (described below) scattering particles
 579 into the atmosphere (e.g. Breneman et al., 2015; Lyons and Thorne, 1973).

580 The outer radiation belt, on the other hand is much more dynamic and consists
 581 of mainly electrons of energies up to a few MeV. The outer belt's spatial extent is
 582 highly variable e.g. see Fig. 1.8, and is typically observed at $4 < L < 8$. Since
 583 the outer radiation belt contains a dynamic population of energetic particles that
 584 pose a threat to human and technological presence in Earth's atmosphere and space,
 585 decades of research has been undertaken to understand and predict the outer radiation
 586 belt particles, waves, and wave-particle interactions. The dynamics of the outer
 587 radiation belt can be understood by considering various competing acceleration and
 588 loss mechanisms which will be described in the following sections.

589 Radiation Belt Particle Sources and Sinks

590 Adiabatic Heating

591 One of the particle heating and transport mechanisms arises from the Earthward
 592 convection of particles. The conservation of J_1 implies that the initial and final v_\perp
 593 depends on the change in the magnetic field amplitude

$$\frac{v_{\perp i}^2}{B_i} = \frac{v_{\perp f}^2}{B_f}. \quad (1.12)$$

594 As a particle convets Earthward, $B_f > B_i$ thus v_\perp must increase. The dipole
 595 magnetic field amplitude can be written as

$$B(L, \theta) = \frac{31.2 \mu\text{T}}{L^3} \sqrt{1 + 3 \cos^2 \theta} \quad (1.13)$$

596 which implies that

$$\frac{v_{\perp f}^2}{v_{\perp i}^2} = \left(\frac{L_i}{L_f}\right)^3. \quad (1.14)$$

597 .

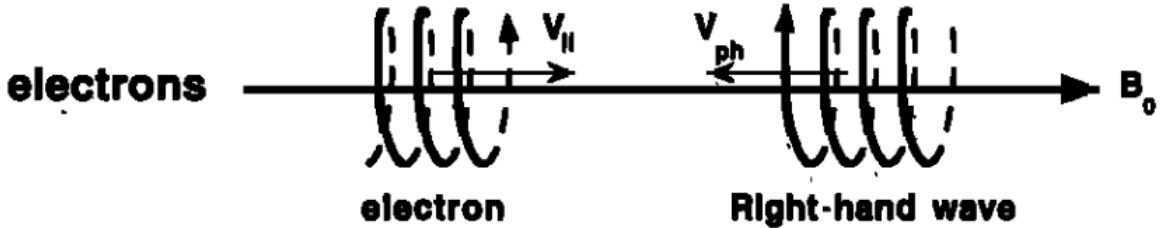
598 In addition, as the particle convects Earthward the distance between the
599 particle's mirror points decrease. If J_2 is conserved, the shrinking bounce path implies
600 that $v_{||}$ must increase by

$$\frac{v_{|| f}^2}{v_{|| i}^2} = \left(\frac{L_i}{L_f}\right)^k \quad (1.15)$$

601 where k ranges from 2 for equatorial pitch angles, $\alpha_{eq} = 0^\circ$, to 2.5 for $\alpha_{eq} = 90^\circ$
602 (Baumjohann and Treumann, 1997). Since the rate of adiabatic heating is greater in
603 the perpendicular direction than heating in the parallel direction, an initially isotropic
604 particle distribution will become anisotropic during its convection. These isotropic
605 particles can then become unstable to wave growth and generate waves in order to
606 reach equilibrium.

607 Wave Resonance Heating

608 Another mechanism that heats particles is due to particles resonating with
609 plasma waves. A few of the electromagnetic wave modes responsible for particle
610 acceleration (and deceleration) relevant to radiation belt dynamics are hiss, whistler
611 mode chorus (chorus), and electromagnetic ion cyclotron (EMIC) waves. These waves
612 are created by the loss cone instability that driven by an anisotropy of electrons
613 for chorus waves, and protons for EMIC waves. The level of anisotropy can be
614 quantified by the ratio of the perpendicular to parallel particle temperatures ($T_{\perp}/T_{||}$).
615 A particle distribution is unstable when $T_{\perp}/T_{||} > 1$ which facilitates wave growth.



$$\omega + k_{\parallel} v_{\parallel} = \Omega^-$$

Figure 1.9: The trajectories of an electron and a right-hand circularly polarized wave during a cyclotron resonance. The electron's v_{\parallel} and the wave's k_{\parallel} are in opposite directions such that the wave's frequency is Doppler shifted to an integer multiple of the electron cyclotron frequency. Figure from (Tsurutani and Lakhina, 1997).

616 Since electrons gyrate in a right-handed sense, the chorus waves also tend to be right
 617 hand circularly polarized (Tsurutani and Lakhina, 1997). The same argument applies
 618 to protons and left hand circularly polarized EMIC waves as well.

619 These circularly polarized waves can resonate with electrons and/or protons
 620 when their combined motion results in a static \vec{E} . One example of a resonance
 621 between a right hand circularly polarized wave and an electron is shown in Fig. 1.21
 622 and is termed the cyclotron resonance. An electron's v_{\parallel} and the wave's parallel wave
 623 vector, k_{\parallel} are in opposite directions such that the wave frequency ω is Doppler shifted
 624 to an integer multiple of the Ω_e at which point the electron feels a static electric
 625 field and is accelerated or decelerated. This acceleration happens when a resonance
 626 condition is satisfied between a wave and a particle for which we will now derive an
 627 illustrative toy model.

628 Assume a uniform magnetic field $\vec{B} = B_0 \hat{z}$ with a parallel propagating ($k = k \hat{z}$),
 629 right-hand circularly polarized wave. The wave's electric field as a function of position
 630 and time can be written as

$$\vec{E} = E_0 (\cos(\omega t - kz) \hat{x} + \sin(\omega t - kz) \hat{y}) \quad (1.16)$$

which is more clearly expressed by taking the dot product to find \vec{E} in the $\hat{\theta}$ direction

$$E_\theta = \vec{E} \times \hat{\theta} = E_0 \cos(\omega t - kz + \theta). \quad (1.17)$$

631 Now assume that the electron is traveling in the $-\hat{z}$ direction with a velocity $\vec{v} = -v_0 \hat{z}$
632 so its time dependent position along \hat{z} is

$$z(t) = -v_0 t \quad (1.18)$$

633 and gyrophase is

$$\theta(t) = -\Omega t + \theta(0) \quad (1.19)$$

634 where the first negative sign comes from the electron's negative charge. Now we put
635 this all together and express the electric field and the force that the electron will
636 experience

$$m \frac{dv_\theta}{dt} = qE_\theta = qE_0 \sin((\omega + kv_0 - \Omega)t + \theta(0)). \quad (1.20)$$

637 This is a relatively complex expression, but when the time dependent component,

$$\omega + kv_0 - \Omega = 0, \quad (1.21)$$

638 the electron will be in a static electric field which will accelerate or decelerate the
639 electron depending on θ_0 , the phase between the wave and the electron. **Show Bortnik
640 2008 plot?** The expression in Eq. 1.21 is commonly referred to as the resonance

641 condition and is more generally written as

$$\omega - k_{||}v_{||} = \frac{n\Omega_e}{\gamma} \quad (1.22)$$

642 where n is the resonance order, and γ is the relativistic correction (e.g. Millan and
 643 Thorne, 2007). In the case of the cyclotron resonance, $\omega \approx \Omega_e$ thus J_1 is violated.
 644 Since J_1 is violated, J_2 and J_3 are also violated since the conditions required to
 645 violate J_2 and J_3 are less stringent than J_1 . It is important to remember that along
 646 the particle's orbit it will encounter and experience the effects of many waves along
 647 its orbit. The typical MLT extent of a handful of waves that are capable of resonating
 648 with radiation belt electrons are shown in Fig. 1.10.

649 Particle Losses

650 Now that we have seen two general mechanisms with which particles are
 651 accelerated and transported in the magnetosphere, we will now consider a few
 652 specific mechanisms with which particles are lost to the atmosphere or the solar
 653 wind. One particle loss mechanism into the solar wind is magnetopause shadowing
 654 (e.g. Ukhorskiy et al., 2006). Particles are sometimes lost when the ring current is
 655 strengthened and Earth's magnetic field strength is increased outside of the ring
 656 current (and reduced on Earth's surface). If the time scale of the ring current
 657 strengthening is slower than a particle drift, J_3 is conserved. Then in order to
 658 conserve J_3 while the magnetic field strength is increased, the particle's drift shell
 659 must move outward to conserve the magnetic flux contained by the drift shell. Then
 660 if the particle's drift shell expands to the point that it crosses the magnetopause, the
 661 particle will be lost to the solar wind.

662 **Move to acceleration?** Another particle loss and acceleration mechanism is driven
 663 by ultra low frequency (ULF) waves and is called radial diffusion. Radial diffusion is

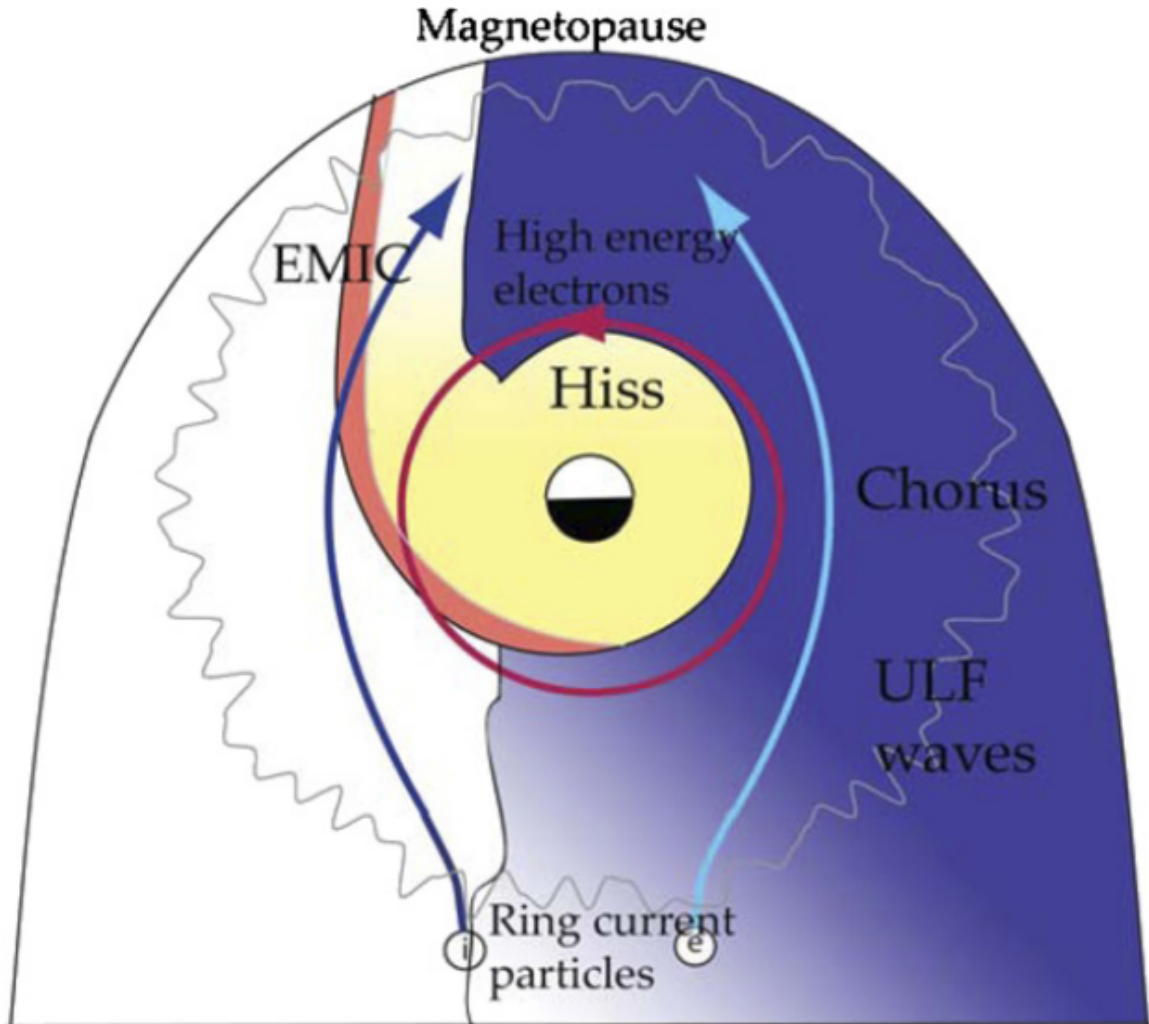


Figure 1.10: Various wave modes in the magnetosphere. Ultra low frequency waves occur through the magnetosphere. Chorus waves are typically observed in the 0-12 midnight-dawn region. EMIC waves are typically observed in the dusk MLT sector. Hiss waves are observed inside the plasmasphere. Figure from Millan and Thorne (2007).

the transport of particles from high to low phase space density, f . If the transport is radially inward, particles will appear to be accelerated. On the other hand, radially outward radial diffusion can transport particles through the magnetopause where they will be lost to the solar wind. Reeves et al. (2013) investigated the driver of particle acceleration during the October 2012 storm and observationally found that inward radial diffusion was not dominant, rather local acceleration via wave-resonance heating (i.e. particle diffusion in pitch angle and energy which will be described below) appeared to be the dominant acceleration mechanism.

The loss mechanism central to this dissertation is pitch angle and energy scattering of electrons by waves. Some of the waves that scatter electrons in energy and pitch angle in the inner magnetosphere are: plasmaspheric hiss (e.g. Breneman et al., 2015; O'Brien et al., 2014), EMIC waves (e.g. Capannolo et al., 2019; Hendry et al., 2017), and chorus waves (e.g. Breneman et al., 2017; Kasahara et al., 2018; Ozaki et al., 2019). These wave-particle interactions occur when the resonance condition in Eq. 1.22 is satisfied at which point the particle's energy and α is modified by the wave. More details regarding the theory of pitch angle and energy diffusion is given in Chapter X. If the wave changes α towards 0 such that $\alpha < \alpha_{LC}$, the particle's mirror point lowers to less than 100 km altitude where the particle can be lost due collisions with air. One manifestation of pitch angle scattering of particles into the loss cone are microbursts: a sub-second durtation impulse of electrons.

Microbursts

Microbursts were first found in high altitude balloon measurements of bremsstrahlung X-rays emitted by microburst electrons impacting the atmosphere by Anderson and Milton (1964). In the following years, numerous balloon flights expanded our knowledge of non-relativistic microbursts (relativistic microbursts have not yet been

689 observed by high altitude balloons) by quantifying the microburst spatial extent,
 690 temporal width, occurrence frequency, extent in L and MLT, and their source (a
 691 local plasma instability vs. a propagating disturbance in the magnetosphere) (e.g.
 692 Barcus et al., 1966; Brown et al., 1965; Parks, 1967; Trefall et al., 1966). Since then,
 693 non-relativistic and relativistic (> 500 keV) microbursts electrons have been directly
 694 observed in LEO with spacecraft including the Solar Anomalous and Magnetospheric
 695 Particle Explorer (SAMPEX) (e.g. Blake et al., 1996; Blum et al., 2015; Douma et al.,
 696 2019, 2017; Greeley et al., 2019; Lorentzen et al., 2001a,b; Nakamura et al., 1995, 2000;
 697 O'Brien et al., 2004, 2003), Montana State University's (MSU) Focused Investigation
 698 of Relativistic Electron Bursts: Intensity, Range, and Dynamics II (FIREBIRD-II)
 699 (Anderson et al., 2017; Breneman et al., 2017; Crew et al., 2016; Klumpar et al.,
 700 2015; Spence et al., 2012), and Science Technologies Satellite (STSAT-I) (e.g. Lee
 701 et al., 2012, 2005). An example microburst time series is shown in Fig. 1.11 and was
 702 observed by the FIREBIRD-II CubeSats. The prominent features of the example
 703 microbursts in Fig. 1.11 are their < 1 second duration, half order of magnitude
 704 increase in count rate above the falling background, and their approximately 200-800
 705 keV energy extent.

706 Microbursts are observed on magnetic field footprints that are connected to the
 707 outer radiation belt (approximately $4 < L < 8$), and are predominately observed in
 708 the 0-12 MLT sector with an elevated occurrence frequency during magnetospherically
 709 disturbed times as shown in Fig. 1.12 (e.g. Douma et al., 2017). O'Brien et al. (2003)
 710 used SAMPEX relativistic electron data and found that microbursts predominately
 711 occur during the main phase of storms, with a heightened occurrence rate during the
 712 recovery phase. Microburst occurrence rates also appear to be higher during high
 713 solar wind velocity events e.g. from co-rotating interaction regions (Greeley et al.,
 714 2019; O'Brien et al., 2003).

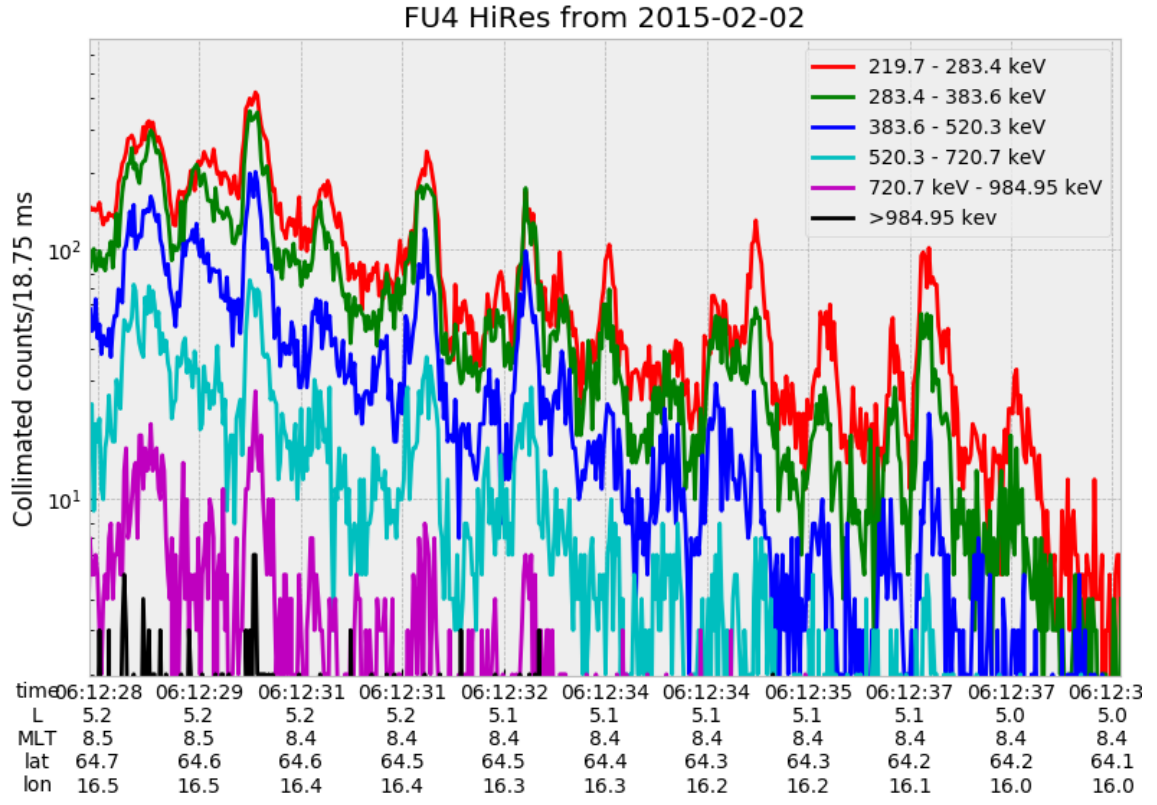


Figure 1.11: An example train of microbursts observed by FIREBIRD-II unit 4 on February 2nd, 2015. The colored curves show the differential energy channel count rates in six channels from ≈ 200 keV to greater than 1 MeV. The x-axis labels show auxiliary information such as time of observation and the spacecraft position in L, MLT, latitude and longitude coordinates.

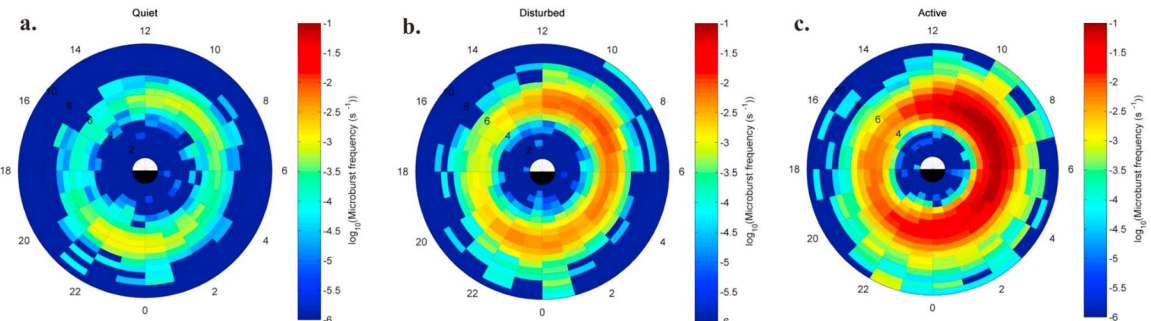


Figure 1.12: Relativistic ($> 1\text{MeV}$) distribution of microburst occurrence rates as a function of L and MLT. The three panels show the microburst occurrence rate dependence on geomagnetic activity, parameterized by the auroral electrojet (AE) index for (a) $\text{AE} < 100 \text{nT}$, (b) $100 < \text{AE} < 300 \text{nT}$ and (c) $\text{AE} > 300 \text{nT}$. Figure from Douma et al. (2017).

The impact of microbursts on atmospheric chemistry has been estimated to be significant. Relativistic microburst electrons impacting the atmosphere are ionized at $< 100 \text{ km}$ altitudes, with higher energy electrons penetrating closer to the surface. The resulting chemical reaction of microburst electrons impacting the atmosphere produces odd hydrogen HO_x and odd nitrogen NO_x molecules. These molecules are partially responsible for destroying ozone (O_3). Seppälä et al. (2018) modeled a six hour relativistic microburst storm and found that the mesospheric ozone was reduced by 7 – 12% in the summer months and 12 – 20% in the winter months.

Furthermore, microbursts have also been estimated to have a significant impact on the outer radiation belt electrons. Radiation belt electron loss due to microbursts has been estimated to be on the order of a day (Breneman et al., 2017; Douma et al., 2019; Lorentzen et al., 2001b; O'Brien et al., 2004; Thorne et al., 2005).

The wave-particle interactions responsible for generating microbursts are also believed to accelerate electrons in the radiation belts. **Mention Thorne's and Paul's work on microburst acceleration and losses. Talk about the balance.**

The range of observed microburst energies range from a few tens of keV (e.g.

731 Datta et al., 1997; Parks, 1967) to greater than 1 MeV (e.g. Blake et al., 1996; Greeley
 732 et al., 2019). The microburst electron flux (J) falls off in energy, and the microburst
 733 energy spectra is typically well fit to a decaying exponential

$$J(E) = J_0 e^{-E/E_0} \quad (1.23)$$

734 where J_0 is the flux at 0 keV (unphysical free parameter) and E_0 quantifies the
 735 efficiency of the scattering mechanism in energy (.e.g Datta et al., 1997; Lee et al.,
 736 2005; Parks, 1967). A small E_0 suggests that mostly low energy particles are scattered
 737 and a high E_0 suggests that the scattering mechanism scatters low and high energy
 738 electrons. Reality is a bit more messy and a high E_0 may be a signature of a scattering
 739 mechanism preferential to high energy electrons, but is hidden by the convolution of
 740 the source particles available to be scattered (typically with a falling energy spectrum)
 741 and the energy-dependent scattering efficiency.

742 The short duration of microbursts observed by a single LEO satellite has an
 743 ambiguity when interpreting what is exactly a microburst. The two possible realities
 744 are: a microburst is very small and spatially stationary so that the LEO spacecraft
 745 passes through it in less than a second. Alternatively, microbursts are spatially large
 746 with a short duration such that the microburst passes by the spacecraft in a fraction
 747 of a second. There are a few ways to distinguish between the two possible realities,
 748 and each one has a unique set of advantages.

749 A high altitude balloon provides essentially a stationary view of the precipitating
 750 particles under the radiation belt footprints so a short-lived, temporal microburst can
 751 be unambiguously identified. Spatial structures, on the other hand, are difficult to
 752 identify because a balloon is essentially still on drift timescales.

753 Multi-spacecraft missions are an alternate solution which can determine if a

754 microburst-like feature is spatial or temporal. As will be shown in this dissertation,
755 if a microburst is observed simultaneously by two spacecraft then it is temporal and
756 has a size greater than the spacecraft separation. On the contrary, if two spacecraft
757 observe a microburst-like feature at different times, but at the same location, then
758 the feature is spatial and may be a curtain (Blake and O'Brien, 2016). Both balloon
759 and multi-spacecraft observational methods have a unique set of strengths, and this
760 dissertation takes the multi-spacecraft approach to identify and study microbursts.

761

Scope of Reserach

762 This dissertation furthers our understanding of the microburst scattering
763 mechanism by observing the scattering directly, and measuring the microburst sizes
764 and comparing them to the size of waves near the magnetic equator where those
765 electrons could have been scattered. Chapter 2 describes a microburst scattering event
766 observed by NASA's Van Allen Probes which was studied in the theoretic framework
767 of pitch angle and energy diffusion. The following two chapters will then study the size
768 of microbursts. Chapter 3 describes a bouncing packet microburst observation made
769 by MSU's FIREBIRD-II mission where the microburst's lower bound longitudinal and
770 latitudinal sizes were estimated. Then Chapter 4 expands the case study from Ch. 3 to
771 a statistical study of microburst sizes using The Aerospace Corporation's AeroCube-6
772 (AC6) CubeSats. In this study, a Monte Carlo and analytic microburst size models
773 were developed to account for the compounding effects of random microburst sizes and
774 locations. Lastly, Ch. 5 will summarize the dissertation work and make concluding
775 remarks regarding outstanding questions in microburst physics.

776

CHAPTER TWO

777

EVIDENCE OF MICROBURSTS OBSERVED NEAR THE EQUATORIAL

778

PLANE IN THE OUTER VAN ALLEN RADIATION BELT

779

Contribution of Authors and Co-Authors

780 Manuscript(s) in Chapter(s) 1

781

782 Author: [type author name here]

783 Contributions: [list contributions here, single-spaced]

784 Co-Author: [type co-author name here]

785 Contributions: [list contributions here, single-spaced]

786 Co-Author: [type co-author name here]

787 Contributions: [list contributions here, single-spaced]

788

789

Manuscript Information

790 [Type Author and Co-author(s) Names Here]

791 Geophysical Research Letters

792 Status of Manuscript: Published in a peer-reviewed journal

793 Wiley

794 Volume 45, Issue 16

795

Key Points

- 796 • First report of direct observation of microbursts at high altitude, near the
 797 equatorial plane.
- 798 • Microbursts' duration, flux enhancement, and energy spectra are similar to prior
 799 observations in LEO.
- 800 • Microburst generation is not consistent with a single quasi-linear gyroresonant
 801 interaction with chorus waves.

802

Abstract

803 We present the first evidence of electron microbursts observed near the equatorial
 804 plane in Earth's outer radiation belt. We observed the microbursts on March 31st,
 805 2017 with the Magnetic Electron Ion Spectrometer and RBSP Ion Composition
 806 Experiment on the Van Allen Probes. Microburst electrons with kinetic energies
 807 of 29-92 keV were scattered over a substantial range of pitch angles, and over time
 808 intervals of 150-500 ms. Furthermore, the microbursts arrived without dispersion in
 809 energy, indicating that they were recently scattered near the spacecraft. We have
 810 applied the relativistic theory of wave-particle resonant diffusion to the calculated
 811 phase space density, revealing that the observed transport of microburst electrons is
 812 not consistent with the hypothesized quasi-linear approximation.

813

Introduction

814 Since the Van Allen radiation belts were discovered by Van Allen (1959) and
 815 Vernov and Chudakov (1960), decades of work has focused on understanding their
 816 origins and effects on the near-Earth space environment and ionosphere-thermosphere

system. The energy content of the outer belt is dominated by energetic electrons, with dynamics controlled by a complex interplay between various source and loss mechanisms. One important loss and acceleration mechanism is gyroresonant diffusion in energy and pitch angle (PA) due to scattering of electrons by plasma waves (e.g. Bortnik et al., 2008; Horne and Thorne, 2003; Meredith et al., 2002; Millan and Thorne, 2007; Summers et al., 1998; Thorne and Andreoli, 1981; Thorne et al., 2005; Walker, 1993).

Chorus waves are commonly associated with PA and energy diffusion. These waves are typically generated by substorm injections into the inner magnetosphere, which lead to a temperature anisotropy of the source electrons with energies up to tens of keV (e.g. Horne et al., 2003; Li et al., 2009a). Since these source electrons drift eastward, chorus is most frequently observed in the dawn sector, but it has been observed at all magnetic local times (MLT) (Li et al., 2009b). Chorus waves are believed to generate electron microburst precipitation through wave-particle interactions.

Microbursts are typically defined as an increase of electron flux in or near the atmospheric loss cone that last < 1 s (e.g. Anderson and Milton, 1964; Blake et al., 1996; Lorentzen et al., 2001a). Empirical and theoretical analyses indicate that microbursts are an important loss process since they can substantially deplete the radiation belt electrons on the order of one day (e.g. Breneman et al., 2017; Lorentzen et al., 2001b; O'Brien et al., 2004; Thorne et al., 2005). Previously, microbursts have been observed in the upper atmosphere in the form of bremsstrahlung X-rays (e.g. Anderson et al., 2017; Parks, 1967; Woodger et al., 2015) and directly in low Earth orbit (LEO) (e.g. Blake et al., 1996; Blum et al., 2015; Breneman et al., 2017; Crew et al., 2016; Lee et al., 2012, 2005; Lorentzen et al., 2001a,b; Mozer et al., 2018; Nakamura et al., 1995, 2000; O'Brien et al., 2004, 2003).

We observed for the first time, microburst-like signatures near their hypothesized origin within the heart of the outer radiation belt. The unique microburst observations we report here were possible with the Van Allen Probe-A's (RBSP-A) Magnetic Electron Ion Spectrometer's (MagEIS) fast sampling rate (~ 11 ms), and RBSP Ion Composition Experiment's (RBSPICE) PA coverage. The observed microbursts' duration, energy spectra, and energy dispersion signature were similar to microbursts previously reported from LEO. Furthermore, we simultaneously observed structureless "hiss-like" whistler mode wave power in the lower band chorus frequency range (Li et al., 2012). From previous observations in LEO (e.g. Blake et al., 1996), it is believed that microbursts result from the impulsive scattering of electrons into or near the loss cone, which is on the order of a few tens of degrees in LEO. With this assumption, high altitude microburst observations near the magnetic equator should be very difficult to make since the atmospheric loss cone there is only a few degrees wide. Thus, the loss cone is smaller than the angular resolution of most particle detectors. Even when an instrument is observing the loss cone, the instrument's field of view will include some portion of the trapped population. The trapped electron flux is typically orders of magnitude higher than that in the loss cone, so that microbursts scattered into the loss cone will be obscured. We present observational evidence that suggests that the sudden impulse of electrons studied here is consistent with the creation of microbursts. Furthermore, these microbursts were scattered over a broad PA range outside of the loss cone, though the loss cone was not directly observed by MagEIS and RBSICE.

This paper explores the properties of the observed microbursts by utilizing in-situ RBSP measurements of waves and particles. This unique high altitude point of view enables us to test whether the observed microburst scattering is consistent with a quasi-linear diffusion process. We have tested this hypothesis with in-situ electron

869 phase space density (PSD) measurements and the relativistic theory of wave-particle
 870 resonant diffusion (Summers et al., 1998; Walker, 1993) to determine if the microburst
 871 electrons diffused in PA and energy.

872 Spacecraft Instrumentation

873 NASA's RBSP mission (Mauk et al., 2013), launched on August 30th, 2012,
 874 consists of a pair of identically instrumented spacecraft. Their orbit and instru-
 875 mentation are uniquely configured to enrich our understanding of the particles and
 876 waves in the inner magnetosphere. The RBSP spacecraft are in highly elliptical, low-
 877 inclination orbit, with perigee of \sim 600 km and apogee of \sim 30,000 km altitude. Their
 878 attitude is maintained by spin-stabilization with a period of \sim 11 s and the spin axis is
 879 roughly sun-pointing. In this analysis, energetic electron measurements from MagEIS
 880 (Blake et al., 2013) and RBSPICE (Mitchell et al., 2013) were used, complemented by
 881 magnetic field and wave measurements from Electric and Magnetic Field Instrument
 882 and Integrated Science (EMFISIS) (Kletzing et al., 2013).

883 We observed these microbursts with RBSP-A's MagEIS low energy instrument
 884 (MagEIS-A) which measures 20-240 keV electrons. It has an angular acceptance
 885 of $3^\circ - 10^\circ$ in the spacecraft spin plane, and 20° perpendicular to the spin plane.
 886 MagEIS-A has a high rate data mode which samples at 1000 angular sectors per
 887 spacecraft spin (11 ms cadence). MagEIS low on RBSP-B on the other hand samples
 888 at 64 angular sectors per spacecraft spin (172 ms cadence), so it was only used for
 889 context.

890 To expand the PA coverage of MagEIS-A, we used the RBSPICE-A time-of-
 891 flight instrument. RBSPICE-A measures electron energies in the range of 19 keV -
 892 1 MeV with a fan of six telescopes (the sixth telescope is used only for calibration
 893 and was excluded from this analysis). These telescopes have an overall acceptance

894 angle of 160° by 12° which allows them to simultaneously sample a substantial part
 895 of the Pitch Angle Distribution (PAD). RBSPICE-A gathers data over 32 sectors
 896 per spacecraft spin (≈ 310 ms cadence) and each sector is divided into three sub-
 897 sectors corresponding to three measurement modes (Manweiler and Zwiener, 2018).
 898 At the time of the observation, the sub-sector used for electron measurements had
 899 an accumulation time of 77 ms. We used RBSPICE-A's Electron Basic Rate (EBR)
 900 telemetry data in this analysis which is not averaged, though it is an integral energy
 901 channel.

902 To understand the dynamics of the local magnetic field, we used the EMFISIS
 903 instrument. EMFISIS provides measurements of the DC magnetic field with flux gate
 904 magnetometers. In addition, it measures electromagnetic waves from 10 Hz to 500
 905 kHz with search coil magnetometers. The spectral matrix and burst data products
 906 used in this analysis were from the EMFISIS waveform receiver (WFR) (10 Hz - 12
 907 kHz) and the high frequency receiver (10 kHz - 500 kHz). Burst data were selectively
 908 captured at a 35 kHz sample rate, and the survey mode spectral matrix data was
 909 captured every 6s.

910

Observations

911 MagEIS-A and RBSPICE-A observed the microburst-like signatures on March
 912 31st, 2017 at $L^* \approx 6$ and $MLT \approx 19$, calculated with the Tsyganenko 2004 magnetic
 913 field model (Tsyganenko and Sitnov, 2005). The magnetosphere was in the recovery
 914 phase of a storm, with minimum Dst of -75 nT observed on March 27th. The local
 915 electron number density was on the order of 1 cm^{-3} at this time, so both RBSP
 916 spacecraft were located outside the plasmasphere. The two spacecraft were separated
 917 by 1700 km, at magnetic latitudes $\lambda \approx -19^\circ$ and $\lambda \approx -18^\circ$ for RBSP-A and RBSP-B,
 918 respectively.

919 MagEIS-A observed microburst electron flux (J) at energies ≥ 92 keV around
 920 11:17 UT as shown in panel (a) in Fig. 4.1. For directional information, panel (b)
 921 in Fig. 4.1 shows flux as a function of local pitch angle (α_L) and time for 46-66 keV
 922 electrons. Electrons that traveled towards the northern hemisphere had $\alpha_L < 90^\circ$ and
 923 southern hemisphere had $\alpha_L > 90^\circ$. The interval between the two vertical dashed
 924 black lines contain the four microbursts examined in this study. We observed these
 925 microbursts at $\alpha_L < 50^\circ$, but MagEIS-A did not sample into the 0° loss cone.

926 Figure 4.1 panel (c) shows the EMFISIS WFR data from RBSP-A. Between
 927 11:17:05 and 11:17:10 UT, we observed an isolated burst of whistler mode wave power
 928 in the frequency range $0.1 < \omega < 0.3 \Omega_{ce0}$, where Ω_{ce0} is the equatorial electron
 929 gyrofrequency. No individual rising or falling tone elements were observed during
 930 this period, and the waves appeared more “hiss-like” (e.g. Li et al., 2012). This wave
 931 was near-parallel propagating (evidence shown in Appendix A) and about 10 minutes
 932 later, weak chorus rising tone elements were observed (not shown).

933 Panels (d)-(f) in Fig. 4.1 are in the same format as panels (a)-(c), but for RBSP-
 934 B. An injection or boundary was observed with RBSP-B at 11:16:50 UT and RBSP-A
 935 observed a similar feature soon after 11:18 UT (not shown).

936 A zoomed-in version of Fig. 4.1 panels (a) and (b) is shown in Fig. 4.2. Panel
 937 (a) shows the four microburst-like signatures observed between 11:17:10 and 11:17:12
 938 UT, at energies up to 92 keV. The observed duration of the microbursts was 150
 939 - 500 ms, and they did not arrive dispersed in energy, which indicates that they
 940 were recently scattered near the spacecraft location. We use IRBEM-Lib, a library
 941 dedicated to radiation belt modeling (Boscher et al., 2012), to calculate the mirror
 942 point altitudes, which were found to be above LEO. Panel (b) shows the RBSPICE-
 943 A EBR time series with the group of microbursts observed at the same time as
 944 in panel (a). To understand the timing relationship between the MagEIS-A and

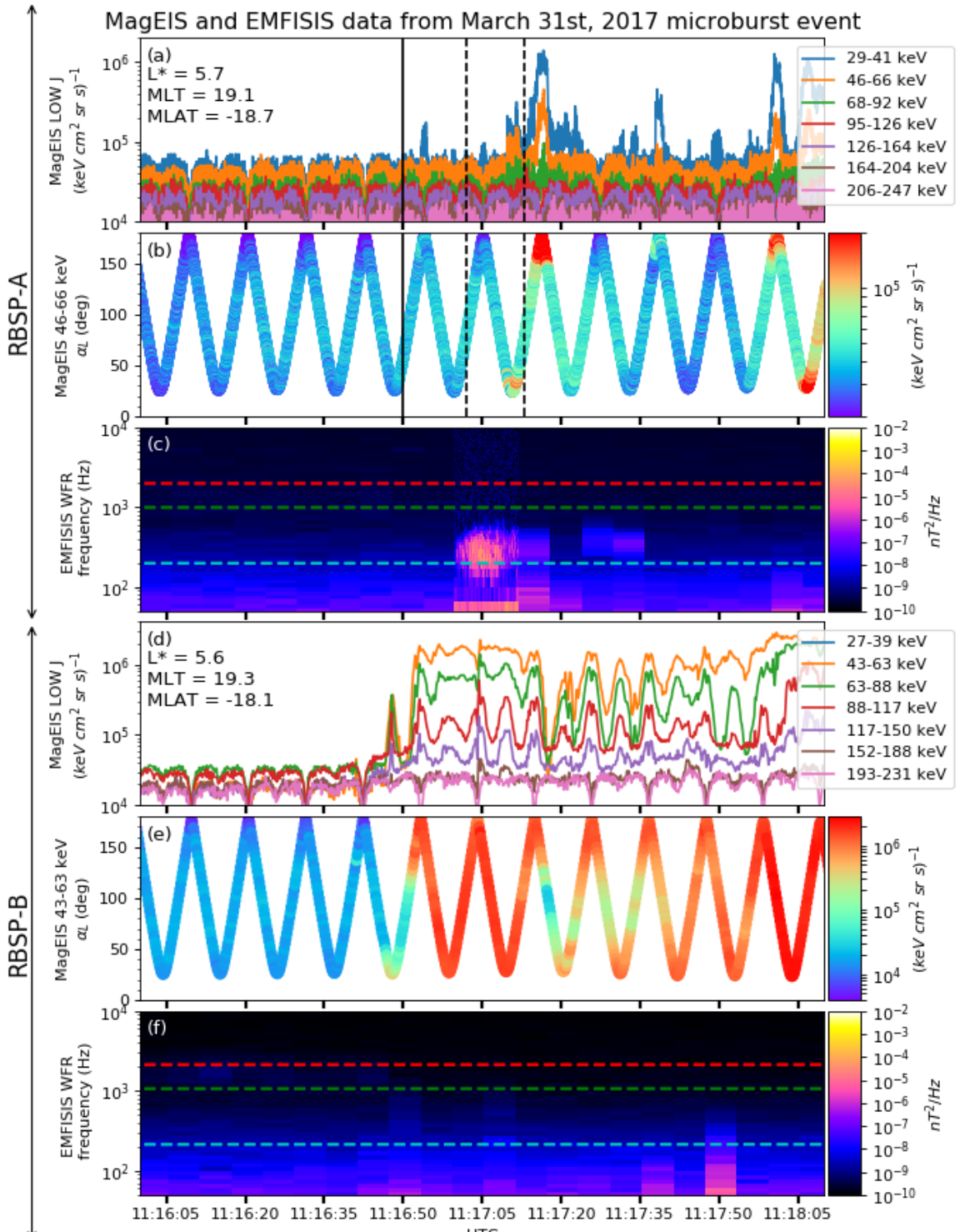


Figure 2.1: Electron and wave conditions from the MagEIS-A and EMFISIS WFR sensors for the microburst time interval. Panels (a), (b), and (c) are from RBSP-A with its position information annotated in panel (a). Panels (d), (e), and (f) are from RBSP-B with its position information annotated in panel (d). Panel (a) is the MagEIS-A high rate timeseries. Panels (b) and (e) show the evolution of the MagEIS-A J as a function of α_L from the ~ 40 to ~ 60 keV channel. Every 10th point is shown in panel (b). The solid black line in panels (a) and (b) mark the end of the time period used for the PSD fit extrapolation analysis explained in section

945 RBSPICE-A observations, we marked the times when MagEIS-A observed the four
 946 microbursts by vertical black arrows in panels (a) and (b). MagEIS-A observed the
 947 first microburst ~ 0.5 s before RBSPICE-A. The bounce period of locally mirroring,
 948 100 keV electrons was ~ 0.8 s, so this was unlikely to have been a returning bounce.
 949 This evidence confirms that these microburst signatures are packets of electrons and
 950 not a boundary moving back and forth at RBSPICE-A's location. To understand the
 951 PA extent of these microbursts, panel (c) shows the 29-41 keV MagEIS-A J and
 952 RBSPICE-A EBR as a function of α_L and time. The microburst J was observed
 953 by MagEIS-A between $25^\circ < \alpha_L < 50^\circ$ and RBSPICE-A between $100^\circ < \alpha_L < 160^\circ$,
 954 with the highest intensities close to $\alpha_L = 90^\circ$. RBSPICE-A observed a 10-80%
 955 enhancement in count rate over those PAs with the evidence presented in Appendix
 956 A.

957 Analysis

958 First, we estimated the microburst energy spectra. For each microburst shown in
 959 Fig. 4.2, its flux was averaged and baseline subtracted using the method from O'Brien
 960 et al. (2004) and then fit with an exponential function. The calculated exponential
 961 E-folding energy was found to vary between 25 and 35 keV, which is consistent with
 962 spectra derived from prior measurements (Datta et al., 1997; Lee et al., 2012, 2005).

963 We then tested the hypothesis that the microburst electrons were transported
 964 in energy and PA by a single chorus wave. We used a procedure similar to sections
 965 3.1 and 4.5 in Meredith et al. (2002) which we describe below.

966 Microburst and Source PSD

967 We estimated the electron PSD, $f(p_\perp, p_\parallel)$ where p_\perp and p_\parallel are the perpendicular
 968 and parallel components of the electron momentum relative to the local magnetic field,

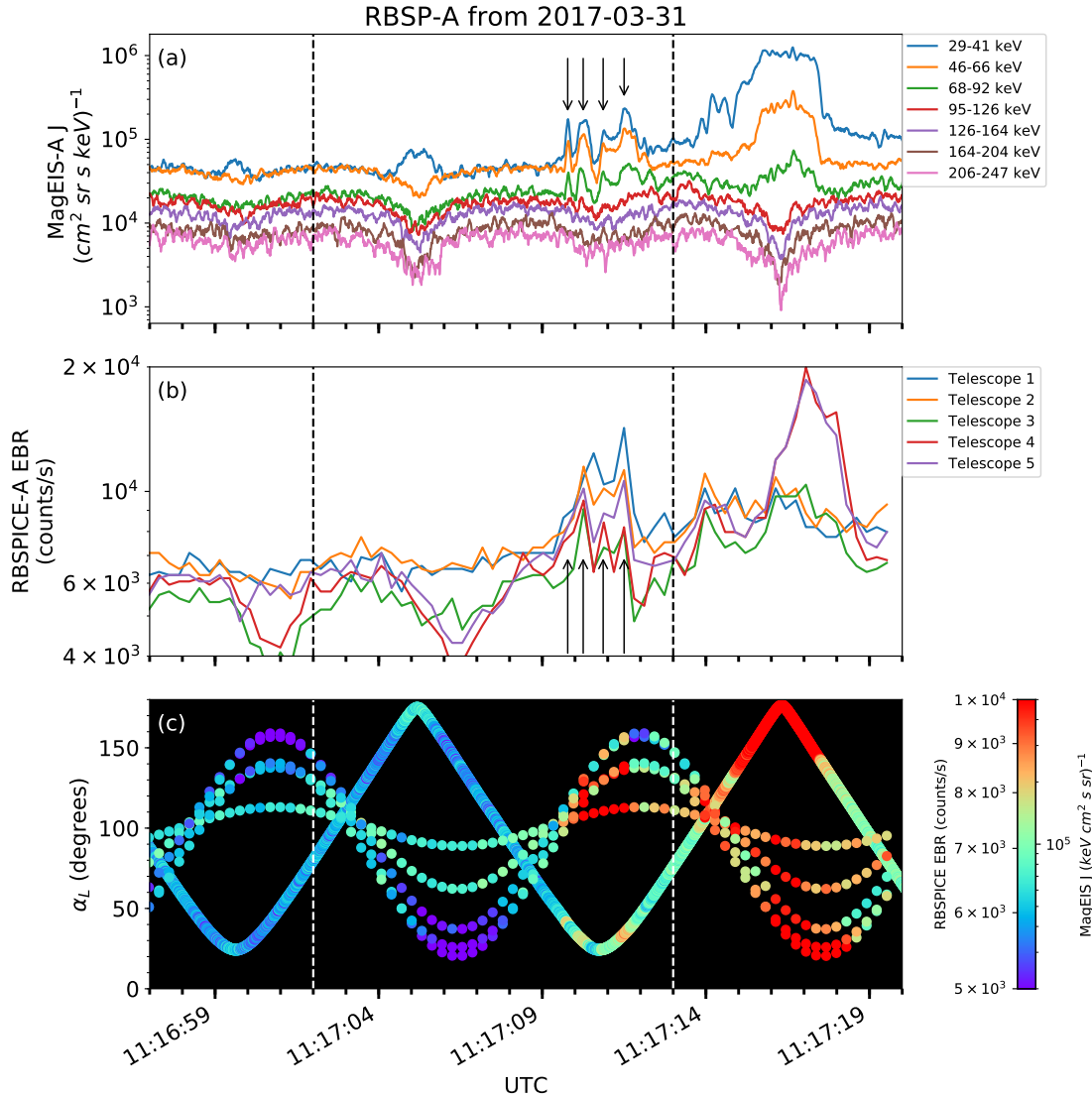


Figure 2.2: Panel (a) shows the MagEIS-A high rate timeseries. Panel (b) shows the RBSPICE EBR count rate timeseries for $\zeta = 19$ keV electrons. The microbursts were observed between 11:17:10 - 11:17:12 UT and are indicated with the vertical black arrows in panels (a) and (b) for MagEIS-A times. Panel (c) shows the RBSPICE EBR (family of relatively sparse sampled curves) and MagEIS-A J from the 29-41 keV energy channel (single curve) as a function of α_L . The vertical dashed lines show the time interval for the PSD analysis.

for the microburst time period. MagEIS-A $J(E, \alpha_L)$ was averaged between 11:17:02 and 11:17:13 UT and binned by α_L into 5° bins. Then, we assumed the conservation of the first adiabatic invariant and mapped α_L to equatorial PA, α_{eq} . The binned $J(E, \alpha_{eq})$ was then converted to $f(p_\perp, p_\parallel)$ via

$$f(p_\perp, p_\parallel) = \frac{J(E, \alpha_{eq})}{p^2}, \quad (2.1)$$

where $p = \sqrt{p_\perp^2 + p_\parallel^2}$. Lastly, α_{eq} was used to separate p into p_\perp and p_\parallel via

$$\frac{p_\parallel}{m_e c} = \frac{\sqrt{E(E + 2E_0)} \cos(\alpha_{eq})}{E_0} \quad (2.2)$$

$$\frac{p_\perp}{m_e c} = \frac{\sqrt{E(E + 2E_0)} \sin(\alpha_{eq})}{E_0} \quad (2.3)$$

where c is the speed of light, E is the kinetic energy, m_e is the electron mass, and E_0 is the electron rest energy. The observed $f(p_\perp, p_\parallel)$ in dimensionless momentum space is shown in Fig. 4.3 in all panels between the p_\parallel axis and the white dotted lines. The bright spot in $f(p_\perp, p_\parallel)$ in the upper p_\parallel plane represents the four microbursts. Along with the observed PSD, we use Fig. 4.3 to explore the various PSD extrapolation and diffusion model assumptions which are described below.

We proceed under the assumption that the source of the microburst electrons is not likely to be at the latitude of the observation, and is closer to the magnetic equator. To look for a source of microburst electrons, we extrapolate the unobserved $f(p_\perp, p_\parallel)$ of electrons with $|\lambda_m| < 19^\circ$ using two cases with a 90° -peaked PAD of the form

$$f(E, \alpha_{eq}) = f_0(E) \sin^n(\alpha_{eq}) \quad (2.4)$$

where $f_0(E)$ is a scaling parameter and n is a power parameter. Similarly to the

981 in-situ $f(p_{\perp}, p_{||})$, the $f(E, \alpha_{eq}) \mapsto f(p_{\perp}, p_{||})$ conversion was applied.

982 In the first case, we fitted Eq. 2.4 to the quiet time $J(E, \alpha_{eq})$ from 11:15:00 to
 983 11:16:50 UT (end time shown as the black vertical line in Fig. 4.1). The fitted
 984 PAD was relatively flat with $0.4 < n < 0.5$ and highest magnitude of f_0 was
 985 $0.05 \text{ cm}^3/(\text{cm MeV})^3$. This extrapolated $f(p_{\perp}, p_{||})$ is shown in Fig. 4.3 panels (A) and
 986 (E), between the dotted white lines for scattering at $\lambda = 0^\circ$ and 20° , respectively.
 987 To confirm the relatively low n parameter, we found times where RBSP-A was in
 988 a similar L-MLT location, but closer to the magnetic equator. At 2 and 19 UT on
 989 the same day, we fit the $J(E, \alpha_{eq})$, and the fit parameters were very similar to the
 990 pre-microburst $f(p_{\perp}, p_{||})$ at 11 UT. Thus it is a reasonable assumption that $f(p_{\perp}, p_{||})$
 991 was relatively flat near the equator.

992 In the other case, we estimate how large n would have to be in order to find
 993 sufficient PSD in MagEIS-A's energy range to be a source of the microburst electrons.
 994 We used $n \in \{1, 2, 4\}$ and we forced the $f_0(E)$ parameter to match the observed
 995 $f(p_{\perp}, p_{||})$ at the most equatorial PAs observed by MagEIS-A. These extrapolations
 996 are shown in columns 2-4 in Fig. 4.3. There was enough source PSD anywhere in
 997 MagEIS-A's energy range only if $n \geq 2$.

998 Motion of resonant electrons in phase space

To calculate the motion of resonant electrons in momentum space, we used the relativistic theory of wave-particle resonant diffusion developed by Walker (1993) and Summers et al. (1998) and applied in Meredith et al. (2002). The chorus wave can modify $f(p_{\perp}, p_{||})$ when a resonance condition is satisfied. The cyclotron resonance condition between an electron with velocity $v = \sqrt{v_{||}^2 + v_{\perp}^2}$ and a parallel propagating

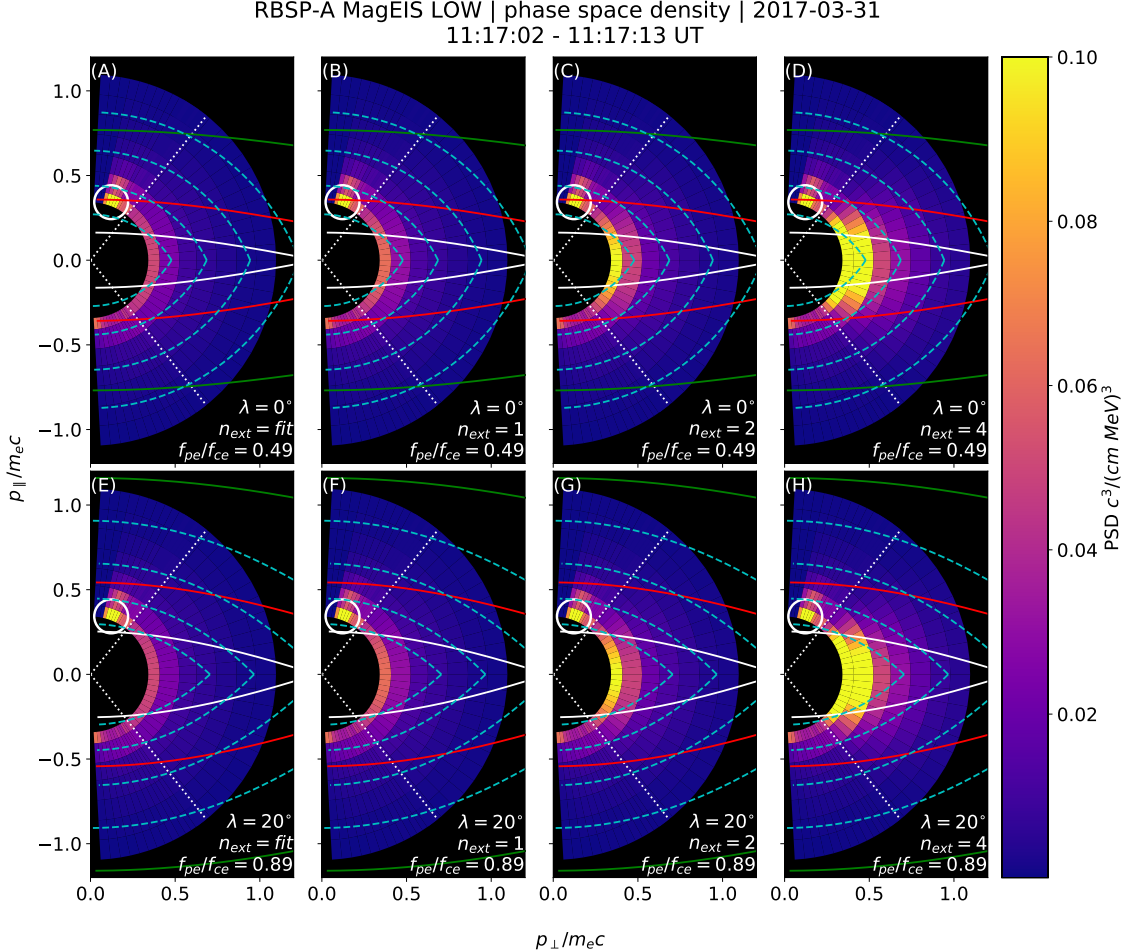


Figure 2.3: The colored annulus represents $f(p_{\perp}, p_{\parallel})$ in normalized momentum space, parallel and perpendicular to the background magnetic field. The microburst $f(p_{\perp}, p_{\parallel})$ is highlighted with the white circle. The columns show different powers of the sine extrapolation, and rows show the different magnetic latitudes of the scattering. The white dotted traces represent the boundary between the data and extrapolation. The green, red, and white solid traces are the resonance curves for $\omega = 0.2\Omega_{ce}$, $0.4\Omega_{ce}$, $0.6\Omega_{ce}$, respectively. The cyan dashed traces are the diffusion curves for a $\omega = 0.4\Omega_{ce}$ wave (waves of other frequency have similar diffusion curves). The magnetic latitude of the scattering, the ratio of the plasma to the cyclotron frequency, and the power of the sine extrapolation is annotated in each panel. For the resonance and diffusion curves, the density model assumed a $n_L = 1 e^-/cm^3$ and $\psi = -1$.

wave of frequency ω and wave number k_{\parallel} is given by

$$\omega - v_{\parallel} k_{\parallel} = \frac{\Omega_{ce}}{\gamma}, \quad (2.5)$$

where Ω_{ce} is the electron gyrofrequency at the scattering location, and γ is the relativistic correction. Assuming the cold plasma approximation,

$$k_{\parallel} = \frac{\omega}{c} \sqrt{1 - \frac{\omega_{pe}^2}{\omega(\omega - |\Omega_{ce}|)}}, \quad (2.6)$$

where ω_{pe} is the plasma frequency. For a particular set of parameters, Eq. 2.5 defines a curve in momentum space that describes which electrons will resonate with a monochromatic wave.

To calculate k_{\parallel} , we approximated the electron number density, $n_e(\lambda)$ locally and at the magnetic equator. Locally, the plasma density was approximately $n_e(\lambda = -20^\circ) = n_L \approx 1 \text{ cm}^{-3}$. We used magnetospheric seismology techniques (e.g. Takahashi and Denton, 2007) to parameterize $n_e(\lambda)$ elsewhere along the field line with

$$n_e(\lambda) = n_e(0) \left(\frac{LR_e}{R(\lambda)} \right)^{\psi} \quad (2.7)$$

where R_e is the Earth's radius, $R(\lambda)$ is the radial distance from the Earth to the spacecraft, and ψ is the exponent parameter. Assuming a dipole magnetic field for which $R(\lambda) = LR_e \cos^2 \lambda$ (e.g. Schulz and Lanzerotti, 1974), we can express Eq. 2.7 in terms of n_L via

$$n_e(\lambda) = n_L \left(\frac{\cos \lambda_L}{\cos \lambda} \right)^{2\psi} \quad (2.8)$$

where we used $\psi = -1$ (higher density at the magnetic equator) in this analysis. We chose this exponent parameter because it is a realistic best case scenario for the

1009 electrons to be transported along the diffusion curves (described below).

Walker (1993) and Summers et al. (1998) argued that a resonant electron will move along diffusion curves in momentum space. A diffusion curve is derived as follows. In the reference frame moving with a monochromatic chorus wave's phase velocity (wave frame), the chorus wave is stationary and there is no electric field. Thus in the wave frame, the electron's kinetic energy is conserved, and the electron's velocity in the wave frame can be expressed in differential form as

$$v_{\parallel} dv_{\parallel} + v_{\perp} dv_{\perp} = 0. \quad (2.9)$$

After a Lorentz transformation of Eq. 2.9 into the magnetospheric frame, kinetic energy will no longer be conserved. After integration and manipulation of Eq. 2.9, we obtain:

$$\left(1 - \frac{u_0^2 v_0^2}{c^4}\right) v_{\parallel}^2 - 2u_0 \left(1 - \frac{v_0^2}{c^2}\right) v_{\parallel} + \left(1 - \frac{u_0^2}{c^2}\right) v_{\perp}^2 = v_0^2 - u_0^2 \quad (2.10)$$

1010 where $u_0 = \omega/k_{\parallel}$ is the phase velocity, and v_0 is a constant of integration (Summers
1011 et al., 1998; Walker, 1993). Equation 2.10 defines a family of diffusion curves in
1012 momentum space on which resonant electrons will move. The distance that an
1013 electron moves along a diffusion curve is a function of wave and plasma parameters,
1014 and is estimated from the magnitude of the diffusion coefficients and the resonance
1015 time.

1016 Comparing the microburst PSD to diffusion theory

1017 Superposed on the PSD plots in Fig. 4.3 are resonance curves for chorus waves
1018 of $\omega = 0.2\Omega_{ce}$, $0.4\Omega_{ce}$, $0.6\Omega_{ce}$ and a few diffusion curves for a $\omega = 0.4\Omega_{ce}$ wave.
1019 These curves were parameterized by λ using a dipole magnetic field for $\lambda = 0^\circ$

(Fig. 4.3, panels A-D) and $\lambda = 20^\circ$ (Fig. 4.3, panels E-H). If the transport of microburst electrons is consistent with gyro-resonant diffusion, a diffusion curve that passes through the microburst $f(p_\perp, p_\parallel)$ must also pass through another region with at least the same magnitude PSD ($f(p_\perp, p_\parallel) \geq 0.1 \text{ c}^3/(\text{cm MeV})^3$) e.g. Fig. 4.3, panel (D). With this constraint, an artificially high extrapolated $f(p_\perp, p_\parallel)$ with $n > 2$ (5 times larger than calculated from the fits) must be assumed for there to have been a sufficient source of PSD anywhere in MagEIS-A's energy range.

We now show that by comparing MagEIS observations with theory, that the minimum wave amplitude necessary to scatter these electrons is much higher than was observed by EMFISIS-A. If we assume a unrealistic PAD with enough PSD just equatorward of RBSP-A, we can use MagEIS-A observations to calculate the minimum $\Delta\alpha_{eq}$ that the electrons were transported. We then used diffusion theory to calculate the necessary wave amplitude. For microbursts with larger PAs, MagEIS-A observed a transport of $\Delta\alpha_{eq} = 9^\circ$ and for microbursts with smaller PAs, the observed transport was $\Delta\alpha_{eq} = 24^\circ$. The required wave amplitude was calculated with Eq. 3 from Thorne and Andreoli (1981) assuming a maximum resonance period of a quarter bounce. The observed change in PA requires a wave amplitude $0.2 < |B_w| < 0.5 \text{ nT}$. For a few brief moments, the EMFISIS-A WFR waveform data showed $0.1 < |B_w| < 0.15 \text{ nT}$, so a transport of 9° is plausible, but not likely for 24° .

Another source of microburst electrons may be from energies below MagEIS-A's range. The Helium, Oxygen, Proton, and Electron mass spectrometer (Funsten et al., 2013) on RBSP-A observed $f(p_\perp, p_\parallel) \geq 0.1 \text{ c}^3/(\text{cm MeV})^3$ for $\pm 23 \text{ keV}$ electrons at this time. We then assumed the wave amplitude derived above to predict the transport in energy. We used the fact that the momentum and pitch angle diffusion coefficients, D_{pp} and $D_{\alpha\alpha}$ are related via $D_{pp}/p^2 \sim D_{\alpha\alpha}$ or equivalently, $\Delta p/p \sim \Delta\alpha$. The observed PA transport corresponds to an energy transport of $6 < \Delta E < 16$

1046 keV. Therefore, this wave can transport 23 keV electrons from smaller pitch angles
 1047 to larger pitch angles and would be observed in the 29 – 41 keV MagEIS-A channel.
 1048 However, this wave is insufficient to transport electrons to the 68 – 92 keV channel
 1049 in one interaction. Therefore we conclude that quasi-linear diffusion cannot explain
 1050 the observed microbursts.

1051

Discussion and Conclusions

1052 These novel observations of impulsive electron signatures reported here fall
 1053 well within the broad definition of a microburst as described in section 3. Their
 1054 properties were similar to microbursts observed in LEO, with an E-folding energy of
 1055 $25 < E_0 < 35$ keV (Datta et al., 1997; Lee et al., 2012, 2005), duration of 150-500
 1056 ms (Lorentzen et al., 2001a), observed upper energy limit of 92 keV, and a lack of
 1057 clear energy dispersion (Breneman et al., 2017). With MagEIS-A’s high time and
 1058 energy resolution, we conclude that these dispersionless microbursts were recently
 1059 scattered near the spacecraft. Furthermore, RBSPICE-A’s PA coverage suggests
 1060 that these electrons were scattered over a substantial range of PAs, with the highest
 1061 intensities near $\alpha_L = 90^\circ$. Overall, our observational evidence suggests that on time
 1062 scales shorter than one bounce period, the chorus wave effectively accelerated trapped
 1063 electrons over a broad PA range.

1064 In the theoretical framework of wave-particle resonant diffusion applied to the
 1065 observed PSD in section 3, we determine that the observed scattering is not consistent
 1066 with the quasi-linear approximation. The nearest source of sufficient PSD is too
 1067 far away in phase space to have been transported by the hypothesized quasi-linear
 1068 process over a timescale shorter than one bounce period (one interaction). A similar
 1069 conclusion was made by Mozer et al. (2018) who used quasi-linear theory constrained
 1070 by RBSP wave measurements. They successfully modeled the one second average

1071 precipitating flux observed with AeroCube-6 (AC-6) CubeSats during a conjunction,
 1072 but they were unable to model the AC-6 fluxes on smaller time scales.

1073 To put these microburst observations into a wider magnetospheric perspective,
 1074 we observed them during the recovery phase of a minimum Dst of -75 nT storm, a
 1075 statistically favorable time period for microbursts (O'Brien et al., 2003). Furthermore,
 1076 during the same storm on March 27th, the Arase spacecraft observed highly correlated
 1077 lower band chorus with 10-50 keV electron precipitation inside the loss cone. At
 1078 that time, Arase's magnetic field footprint was near The Pas All-Sky Imager (part
 1079 of the THEMIS mission) which simultaneously observed pulsating auroral patches
 1080 (Kasahara et al., 2018). While microbursts and pulsating auroral patches have not
 1081 been clearly connected, they are both believed to be a product of electron scattering
 1082 by whistler mode waves (e.g. Lorentzen et al., 2001a; Nishimura et al., 2011; O'Brien
 1083 et al., 2003; Ozaki et al., 2012).

1084 The combined capabilities of the various RBSP wave and particle instruments
 1085 enable comprehensive studies of wave-particle scattering and the resulting microburst
 1086 precipitation. From a preliminary search by the authors, other microburst-like
 1087 signatures have been found with RBSP. Similar to previous studies (e.g. Blum et al.,
 1088 2015; O'Brien et al., 2003), a statistical study of high-altitude microbursts in L-MLT
 1089 space needs to be conducted before we can verify that these microbursts are the
 1090 counterpart of the microbursts observed in LEO and the upper atmosphere.

1091

Acknowledgments

1092 The authors acknowledge the technicians, engineers, and scientists who made the
 1093 RBSP and AC-6 missions possible. One author (Shumko) would like to acknowledge
 1094 Dana Longcope for his help in understanding the quasi-linear diffusion theory. Dr.
 1095 Gkioulidou was supported by JHU/APL subcontract 131803 to the NJIT under NASA

1096 Prime contract NNN06AA01C. EMFISIS work was supported by JHU/APL contract
1097 no. 921647 under NASA Prime contract No. NAS5-01072. The MagEIS instrument
1098 was funded by NASA's Prime contract no. NAS5-01072. The level 3 MagEIS-A
1099 "high rate" data is available in the Supporting Information, level 1 RBSPICE EBR
1100 data is archived at <http://rbspicea.ftecs.com/>, and the EMFISIS level 2 spectral
1101 matrix and burst data as well as the level 3 magnetometer data is archived at
1102 <http://emfisis.physics.uiowa.edu/data/index>. The IRBEM Library can be obtained
1103 at irbem.sf.net.

1104 CHAPTER THREE

1105 MICROBURST SCALE SIZE DERIVED FROM MULTIPLE BOUNCES OF A

1106 MICROBURST SIMULTANEOUSLY OBSERVED WITH THE FIREBIRD-II

1107 CUBESATS

1108 Contribution of Authors and Co-Authors

1109 Manuscript(s) in Chapter(s) 1

1110

1111 Author: [type author name here]

1112 Contributions: [list contributions here, single-spaced]

1113 Co-Author: [type co-author name here]

1114 Contributions: [list contributions here, single-spaced]

1115 Co-Author: [type co-author name here]

1116 Contributions: [list contributions here, single-spaced]

1117

1118

Manuscript Information

1119 [Type Author and Co-author(s) Names Here]

1120 Geophysical Research Letters

1121 Status of Manuscript: Published in a peer-reviewed journal

1122 Wiley

1123 Volume 45, Issue 17

1124

1125 This article is available under the terms of the Creative Commons Attribution

1126 Non-Commercial No Derivatives License CC BY-NC-ND (which may be updated

1127 from time to time) and permits non-commercial use, distribution, and reproduction

1128 in any medium, without alteration, provided the original work is properly cited and

1129 it is reproduced verbatim.

1130

Key Points

1131

- Multiple bounces from a microburst were observed by the two FIREBIRD-II CubeSats at LEO.
- The lower bounds on the microburst scale size at LEO were 29 ± 1 km (latitudinal) and 51 ± 11 km (longitudinal).
- Deduced lower bound equatorial scale size was similar to the whistler-mode chorus source scale.

1137

Abstract

1138

We present the observation of a spatially large microburst with multiple bounces made simultaneously by the FIREBIRD-II CubeSats on February 2nd, 2015. This is the first observation of a microburst with a subsequent decay made by two co-orbiting but spatially separated spacecraft. From these unique measurements, we place estimates on the lower bounds of the spatial scales as well as quantify the electron bounce periods. The microburst's lower bound latitudinal scale size was 29 ± 1 km and the longitudinal scale size was 51 ± 1 km in low earth orbit. We mapped these scale sizes to the magnetic equator and found that the radial and azimuthal scale sizes were at least 500 ± 10 km and 530 ± 10 km, respectively. These lower bound equatorial scale sizes are similar to whistler-mode chorus wave source scale sizes, which supports the hypothesis that microbursts are a product of electron scattering by chorus waves. Lastly, we estimated the bounce periods for 200-800 keV electrons and found good agreement with four common magnetic field models.

1151

Introduction

1152 The dynamics of radiation belt electrons are complex, and are driven by
 1153 competition between source and loss processes. A few possible loss processes are
 1154 radial diffusion (Shprits and Thorne, 2004), magnetopause shadowing (Ukhorskiy
 1155 et al., 2006), and pitch angle and energy diffusion due to scattering of electrons by
 1156 plasma waves (e.g. Abel and Thorne, 1998; Horne and Thorne, 2003; Meredith et al.,
 1157 2002; Mozer et al., 2018; Selesnick et al., 2003; Summers et al., 1998; Thorne et al.,
 1158 2005). There are a variety of waves that cause pitch angle scattering, including
 1159 electromagnetic ion cyclotron waves, plasmaspheric hiss, and chorus (Millan and
 1160 Thorne, 2007; Thorne, 2010). Chorus predominantly occurs in the dawn sector (6-12
 1161 magnetic local times (MLT)) (Li et al., 2009b) where it accelerates electrons with
 1162 large equatorial pitch angles and scatters electrons with small equatorial pitch angles
 1163 (Horne and Thorne, 2003). Some of these electrons may be impulsively scattered
 1164 into the loss cone, where they result in short-duration (~ 100 ms) enhancements in
 1165 precipitating flux called microbursts.

1166 Anderson and Milton (1964) coined the term microburst to describe high altitude
 1167 balloon observations of ~ 100 ms duration enhancements of bremsstrahlung X-
 1168 rays emitted from scattered microburst electrons impacting the atmosphere. Since
 1169 then, non-relativistic (less than a few hundred keV) microbursts have been routinely
 1170 observed with other balloon missions (e.g. Anderson et al., 2017; Parks, 1967; Woodger
 1171 et al., 2015). A review of the literature shows no reports of microbursts above a few
 1172 hundred keV observed by balloons (Millan et al., 2002; Woodger et al., 2015). This
 1173 lack of observation may be explained by relatively weaker pitch angle scattering of
 1174 relativistic electrons by chorus (Lee et al., 2012).

1175 In addition to the X-ray signature for bursts of electron precipitation, the

1176 precipitating relativistic and non-relativistic electrons have been measured in situ by
 1177 spacecraft orbiting in low earth orbit (LEO). Hereinafter, we refer to these electron
 1178 signatures observed by LEO spacecraft also as microbursts. Microbursts have been
 1179 observed with, e.g. the Solar Anomalous and Magnetospheric Particle Explorer's
 1180 (SAMPEX) \gtrsim 150 keV and \gtrsim 1 MeV channels (Blake et al., 1996; Blum et al., 2015;
 1181 Lorentzen et al., 2001a,b; Nakamura et al., 1995, 2000; O'Brien et al., 2004, 2003) and
 1182 Focused Investigation of Relativistic Electron Bursts: Intensity, Range, and Dynamics
 1183 (FIREBIRD-II) with its \gtrsim 200 keV energy channels (Anderson et al., 2017; Breneman
 1184 et al., 2017; Crew et al., 2016).

1185 Understanding microburst precipitation and its scattering mechanism is impor-
 1186 tant to radiation belt dynamics. The scattering mechanism has been observationally
 1187 studied by e.g. Lorentzen et al. (2001b) who found that microbursts and chorus
 1188 waves predominantly occur in the dawn sector and Breneman et al. (2017) made
 1189 a direct observational link between individual microbursts and chorus elements.
 1190 Microbursts have been modeled and empirically estimated to be capable of depleting
 1191 the relativistic electron population in the outer radiation belt on the order of a day
 1192 (Breneman et al., 2017; O'Brien et al., 2004; Shprits et al., 2007; Thorne et al., 2005).
 1193 An important parameter in this estimation of instantaneous radiation belt electron
 1194 losses due to microbursts is their scale size. Parks (1967) used balloon measurements
 1195 of bremsstrahlung X-rays to estimate the high altitude scale size of predominantly low
 1196 energy microbursts to be 40 ± 14 km. In Blake et al. (1996) a microburst with multiple
 1197 bounces was observed by SAMPEX, and the microburst's latitudinal scale size in LEO
 1198 was estimated to have been "at least a few tens of kilometers". Blake et al. (1996)
 1199 concluded that typically microbursts are less than a few tens of electron gyroradii in
 1200 size (at $L = 5$ at LEO, the gyroradii of 1 MeV electrons is on the order of 100 m).
 1201 Dietrich et al. (2010) used SAMPEX along with ground-based very low frequency

1202 stations to conclude that during one SAMPEX pass, the observed microbursts had
 1203 scale sizes less than 4 km.

1204 Since February 1st, 2015, microbursts have been observed by FIREBIRD-II, a
 1205 pair of CubeSats in LEO. Soon after launch, when the two FIREBIRD-II spacecraft
 1206 were at close range, a microburst with a scale size greater than 11 km was observed
 1207 (Crew et al., 2016). On the same day, FIREBIRD-II simultaneously observed a
 1208 microburst with multiple bounces. The microburst decay was observed over a period
 1209 of a few seconds, while the spacecraft were traveling predominantly in latitude. Here
 1210 we present the analysis and results of the latitude and longitude scale sizes and
 1211 bounce periods of the first microburst with multiple bounces observed with the two
 1212 FIREBIRD-II spacecraft.

1213

Spacecraft and Observation

1214 The FIREBIRD missions are comprised of a pair of identically-instrumented
 1215 1.5U CubeSats (15 x 10 x 10 cm) that are designed to measure electron precipitation
 1216 in LEO (Klumpar et al., 2015; Spence et al., 2012). The second mission, termed
 1217 FIREBIRD-II, was launched on January 31st 2015. The two FIREBIRD-II CubeSats,
 1218 identified as Flight Unit 3 (FU3) and Flight Unit 4 (FU4), were placed in a 632 km
 1219 apogee, 433 km perigee, and 99° inclination orbit (Crew et al., 2016). FU3 and FU4
 1220 are orbiting in a string of pearls configuration with FU4 ahead, to resolve the space-
 1221 time ambiguity of microbursts. Each FIREBIRD-II unit has two solid state detectors:
 1222 one is mounted essentially at the spacecraft surface, covered only by a thin foil acting
 1223 as a sun shade, with a field of view of 90° (surface detector), and the other is beneath
 1224 a collimator which restricts the field of view to 54° (collimated detector). Only FU3
 1225 has a functioning surface detector, so this analysis utilizes the collimated detectors.
 1226 FU3's surface and collimated detectors, as well as FU4's collimated detector observe

1227 electron fluxes in six energy channels from ~ 230 keV to > 1 MeV. FIREBIRD-II's
 1228 High Resolution (HiRes) electron flux data is gathered with an adjustable sampling
 1229 period of 18.75 ms by default and can be as fast as 12.5 ms.

1230 On February 2nd, 2015 at 06:12 UT, both FIREBIRD-II spacecraft simulta-
 1231 neously observed an initial microburst, followed by subsequent periodic electron
 1232 enhancements of diminishing amplitude shown in Fig. 3.1. This is thought to be
 1233 the signature of a single burst of electrons, some of which precipitate, but the rest
 1234 mirror near the spacecraft then bounce to the conjugate hemisphere where they mirror
 1235 again and the subsequent bounces produce a train of decaying peaks (Blake et al.,
 1236 1996; Thorne et al., 2005). This bounce signature occurred during the transition
 1237 between the main and recovery phases of a storm with a minimum Dst of -44 nT
 1238 ($K_p = 4$, and $AE \approx 400$ nT). At this time, the HiRes data was sampled at 18.75 ms.
 1239 Five peaks were observed by both spacecraft. The fifth peak observed by FU4 was
 1240 comparable to the Poisson noise and was not used in this analysis. This microburst
 1241 was observed from the first energy channel ($\approx 200 - 300$ keV), to the fourth energy
 1242 channel ($\approx 500 - 700$ keV), and FU3's surface detector observed the microburst up
 1243 to the fifth energy channel (683 - 950 keV).

1244 The HiRes data in Fig. 3.1 shows signs of energy dispersion, characterized by
 1245 higher energy electrons arriving earlier than the lower energies. This time of flight
 1246 energy dispersion tends to smear out the initial sharp burst upon each subsequent
 1247 bounce. The first peak does not appear to be dispersed, and subsequent peaks show
 1248 a dispersion trend consistent across energy channels. The black vertical bars have
 1249 been added to Fig. 3.1 to highlight this energy dispersion. This dispersion signature
 1250 and amplitude decay implies that the first peak was observed soon after the electrons
 1251 were scattered, followed by decaying bounces.

1252 At this time, in magnetic coordinates, FIREBIRD-II was at McIlwain $L = 4.7$

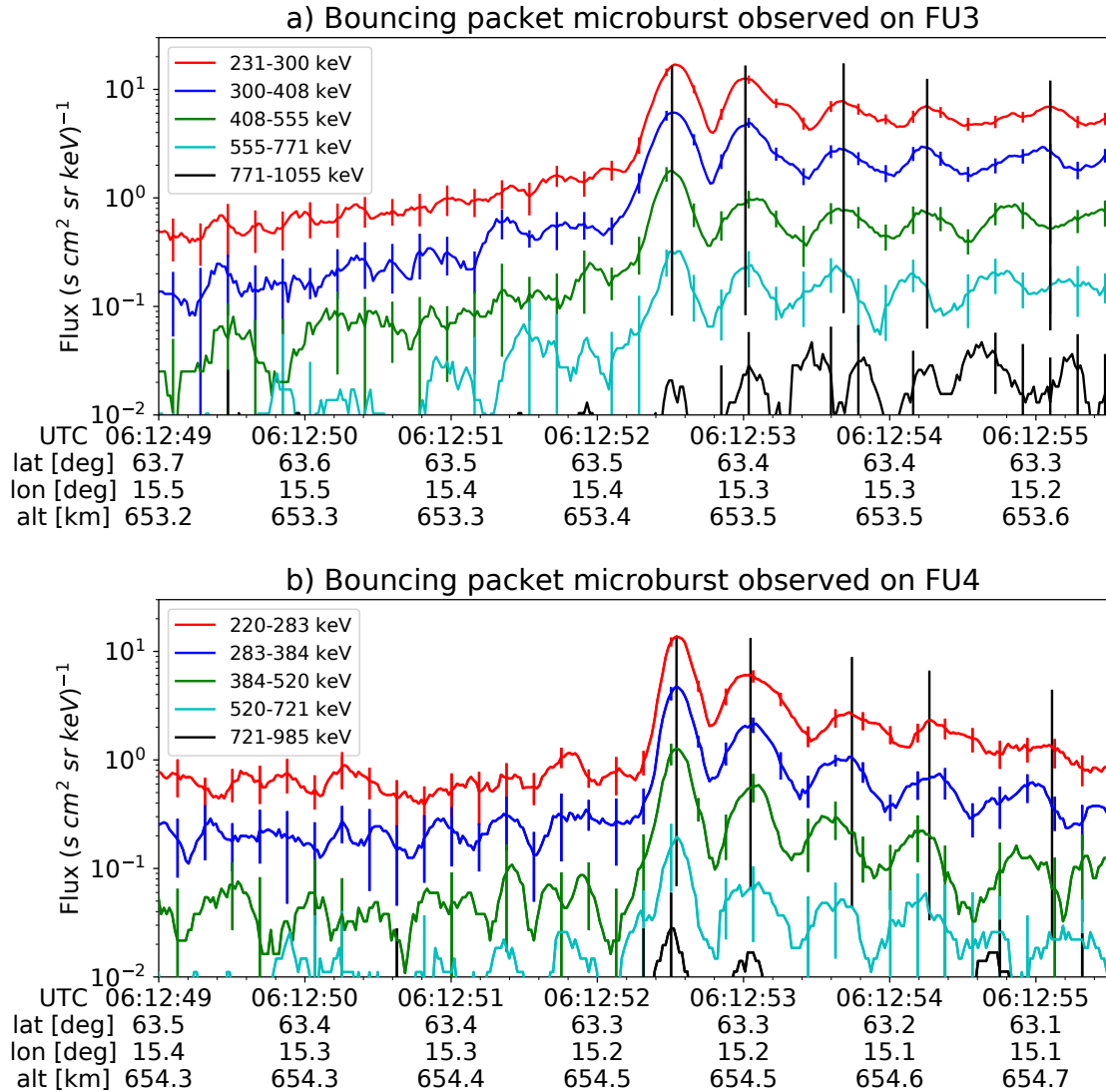


Figure 3.1: HiRes data of the microburst observed at February 2nd, 2015 at 06:12:53 UT, smoothed with a 150 ms rolling average. The subsequent bounces showed some energy dispersion. As discussed in Appendix B, a time correction of -2.28 s was applied to FU3. While the flux from five energy channels is shown, only channels with reasonable counting statistics were used for the spatial scale analysis. Vertical colored bars show the \sqrt{N} error every 10th data point and vertical black bars are lined up with the peaks in the 220-283 keV energy channel to help identify dispersion.

1253 and MLT = 8.3, calculated with the Tsyganenko 1989 (T89) magnetic field model
 1254 (Tsyganenko, 1989) using IRBEM-Lib (Boscher et al., 2012). Geographically, they
 1255 were above Sweden, latitude = 63°N, longitude = 15°E, altitude = 650 km. This
 1256 geographic location is magnetically conjugate to the east of the so-called South
 1257 Atlantic Anomaly (SAA). The SAA is the location where the mirror points of electrons
 1258 tend to occur at locations deeper in the atmosphere owing to the offset of the
 1259 dipole magnetic field from the Earth's center. Electrons with pitch angles within the
 1260 drift loss cone (DLC) will encounter the SAA and be removed from their eastward
 1261 longitudinal drift paths (Comess et al., 2013; Dietrich et al., 2010). FU3 and FU4 are
 1262 therefore both in regions where the particles in the DLC have recently precipitated,
 1263 leaving only particles that were recently scattered. At the spacecraft location, locally
 1264 mirroring electrons would have mirrored at 95 km in the opposite hemisphere, with
 1265 more field aligned electrons mirroring at even lower altitudes. From the analysis done
 1266 by Fang et al. (2010), the peak in the total ionization rate in the atmosphere for 100
 1267 keV electrons is around 80 km altitude, while the total ionization rate from 1 MeV
 1268 electrons peaks around 60 km altitude. It is, therefore, expected that a fraction of the
 1269 microburst electrons will survive each encounter with the atmosphere. By plotting
 1270 the peak flux as a function of bounce (not shown), it was found that 40 - 60 % of the
 1271 microburst electrons were lost on the first bounce, similar to the 33% loss per bounce
 1272 observed for a bouncing microburst observed by SAMPEX (Thorne et al., 2005).

1273

Analysis

1274 At the beginning of the FIREBIRD-II mission, two issues prevented the proper
 1275 analysis of the microburst's spatial scale size: the spacecraft clocks were not
 1276 synchronized, and their relative positions were not accurately known. We addressed
 1277 these issues with a cross-correlation time lag analysis described in detail in Appendix

1278 B. From this analysis, the time correction was 2.28 ± 0.12 s (applied to Fig. 3.1) and
 1279 the separation was 19.9 ± 0.9 km at the time of the microburst observation.

1280 Electron Bounce Period

1281 We used this unique observation of bouncing electrons to calculate the bounce
 1282 period, t_b as a function of energy and compare it to the energy-dependent t_b curves
 1283 derived from four magnetic field models, the results of which are shown in Fig. 3.2.
 1284 The observed t_b and uncertainties were calculated by fitting the baseline-subtracted
 1285 HiRes flux. The baseline flux used in this analysis is given in O'Brien et al. (2004)
 1286 as the flux at the 10th percentile over a specified time interval, which in this analysis
 1287 was taken to be 0.5 seconds. The flux was fitted with a superposition of Gaussians
 1288 for each energy channel, and the uncertainty in flux was calculated using the Poisson
 1289 error from the microburst and baseline fluxes summed in quadrature. Using the fit
 1290 parameters, the mean t_b for the lowest four energy channels is shown in Fig. 3.2. The
 1291 trend of decreasing t_b as a function of energy is evident in Fig. 3.2, which further
 1292 supports the assumption that the subsequent peaks are bounces, and not a train of
 1293 microbursts scattered by bouncing chorus.

1294 The decaying peaks in the 231-408 keV electron flux observed by FU3's lowest
 1295 two energy channels (see Fig. 3.1) were right-skewed. One explanation is that there
 1296 was in-channel energy dispersion within those channels. Since t_b of higher energy
 1297 electrons is shorter, a right-skewed peak implies that higher energy electrons were
 1298 more abundant within that channel e.g. in FU3's 231-300 keV channel, the 300 keV
 1299 electrons will arrive sooner than the 231 keV electrons, but will they will be binned
 1300 in the same channel. A Gaussian fit cannot account for this in-channel dispersion,
 1301 and as a first order correction, minima between peaks was used to calculate t_b , and
 1302 is shown in Fig. 3.2. The observed energy-dependent dispersion shown in Fig. 3.2

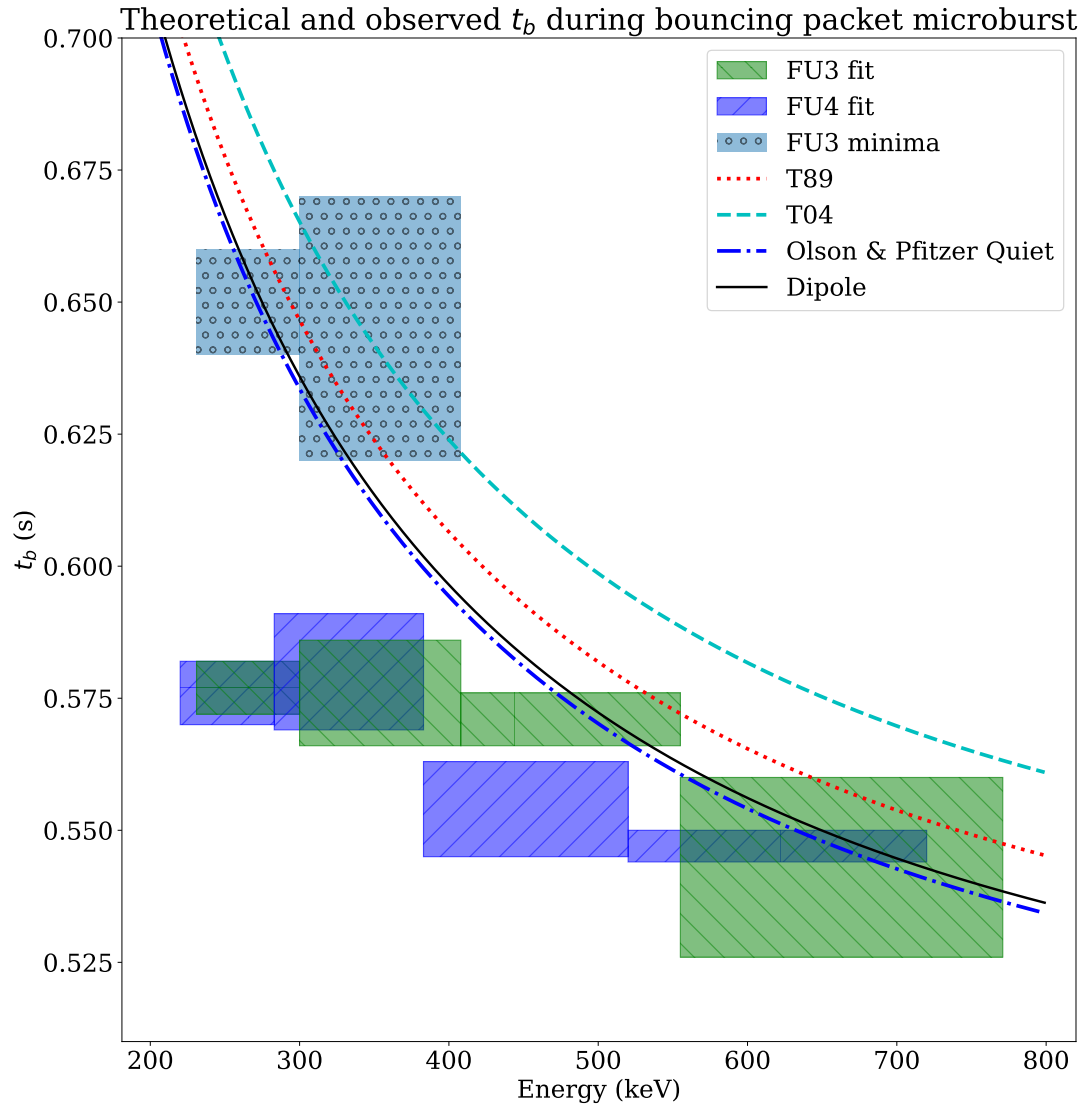


Figure 3.2: Observed and theoretical t_b for electrons of energies from 200 to 770 keV. The solid black line is t_b in a dipole magnetic field, derived in Schulz and Lanzerotti (1974). The red dotted and cyan dashed lines are the t_b derived using the T89, and T04 magnetic field models with IRBEM-Lib. Lastly, the blue dot-dash curve is the t_b derived using the Olson & Pfitzer Quiet model. The green and purple rectangles represent the observed t_b for FU3 and FU4 using a Gaussian fit, respectively. The blue rectangles represent the observed t_b calculated with the minima between the bounces. The width of the boxes represent the width of those energy channels, and the height represents the uncertainty from the fit.

1303 is consistent with higher energy peaks returning sooner. This dispersion consistency
 1304 further supports the assumption that the subsequent peaks are bounces, and not a
 1305 train of microbursts scattered by bouncing chorus.

1306 To compare the observed and modeled t_b , we superposed t_b curves for various
 1307 models including an analytical solution in a dipole (Schulz and Lanzerotti, 1974), and
 1308 numerical models: T89, Tsyganenko 2004 (T04) (Tsyganenko and Sitnov, 2005), and
 1309 Olson & Pfitzer Quiet (Olson and Pfitzer, 1982) in Fig. 3.2. The numerical t_b curves
 1310 were calculated using a wrapper for IRBEM-Lib. This code traces the magnetic field
 1311 line between mirror points, and calculates t_b assuming conservation of energy and the
 1312 first adiabatic invariant for electrons mirroring at FIREBIRD-II. With the empirical
 1313 t_b , the models agree within FIREBIRD-II's uncertainties, but the T04 model has the
 1314 largest discrepancy compared to the other models.

1315 Microburst Energy Spectra

1316 Next, we investigated the energy spectra of this microburst. The energy spectra
 1317 was modeled with an exponential that was fit to the peak flux derived from the
 1318 Gaussian fit parameters in section 3 to all but the highest energy channel. We found
 1319 that the E-folding energy, $E_0 \sim 100$ keV. This spectra is similar to spectra show
 1320 by Lee et al. (2005) from STSAT-1 and Datta et al. (1997) from sounding rocket
 1321 measurements. The energy spectra is soft for a typical microburst observed with
 1322 FIREBIRD-II and there was no statistically significant change in E_0 for subsequent
 1323 bounces.

1324 Microburst Scale Sizes

1325 Lastly, after we applied the time and separation corrections detailed in Appendix
 1326 B, we mapped the locations of FU3 and FU4 in Fig. 3.3. The locations where FU3 saw
 1327 peaks 1-5 and where FU4 saw peaks 1-4 are shown as P1-5 and P1-4, respectively.

1328 The lower bound on the latitudinal extent of the microburst was the difference in
 1329 latitude between P1 on FU3 and P4 on FU4 and was found to be 29 ± 1 km. The
 1330 uncertainty was estimated from the spacecraft separation uncertainty described in
 1331 Appendix B. This scale size is the largest reported by FIREBIRD-II.

1332 In section 3, we showed that the observed decaying peaks were likely due to
 1333 bouncing, so we assume that the observed electrons in subsequent bounces were the
 1334 drifted electrons from the initial microburst. Under this assumption, the scattered
 1335 electrons observed in the last bounce by FIREBIRD-II, must have drifted east from
 1336 their initial scattering longitude, allowing us to calculate the minimum longitudinal
 1337 scale size. Following geometrical arguments, the distance that electrons drift east in
 1338 a single bounce is a product of the circumference of the drift shell foot print, and the
 1339 fraction of the total drift orbit traversed in a single bounce and is given by,

$$d_{az} = 2\pi(R_E + A) \cos(\lambda) \frac{t_b}{\langle T_d \rangle} \quad (3.1)$$

where R_E is the Earth's radius, A is the spacecraft altitude, λ is the magnetic latitude,
 t_b is the electron bounce period, and $\langle T_d \rangle$ is the electron drift period. Parks (2003)
derived $\langle T_d \rangle$ to be,

$$\langle T_d \rangle \approx \begin{cases} 43.8/(L \cdot E) & \text{if } \alpha_0 = 90^\circ \\ 62.7/(L \cdot E) & \text{if } \alpha_0 = 0^\circ \end{cases} \quad (3.2)$$

1340 where E is the electron energy in MeV, L is the L shell, and α_0 is the equatorial pitch
 1341 angle. Electrons mirroring at FIREBIRD-II have $\alpha_0 \approx 3.7^\circ$ and so the $\alpha_0 = 0^\circ$ limit
 1342 was used.

1343 The microburst's longitudinal scale size is defined as the distance the highest
 1344 energy electrons drifted in the time between the observations of the first and last
 1345 peaks. This scale size is given by $D_{az} = n d_{az}$ where n is the number of bounces

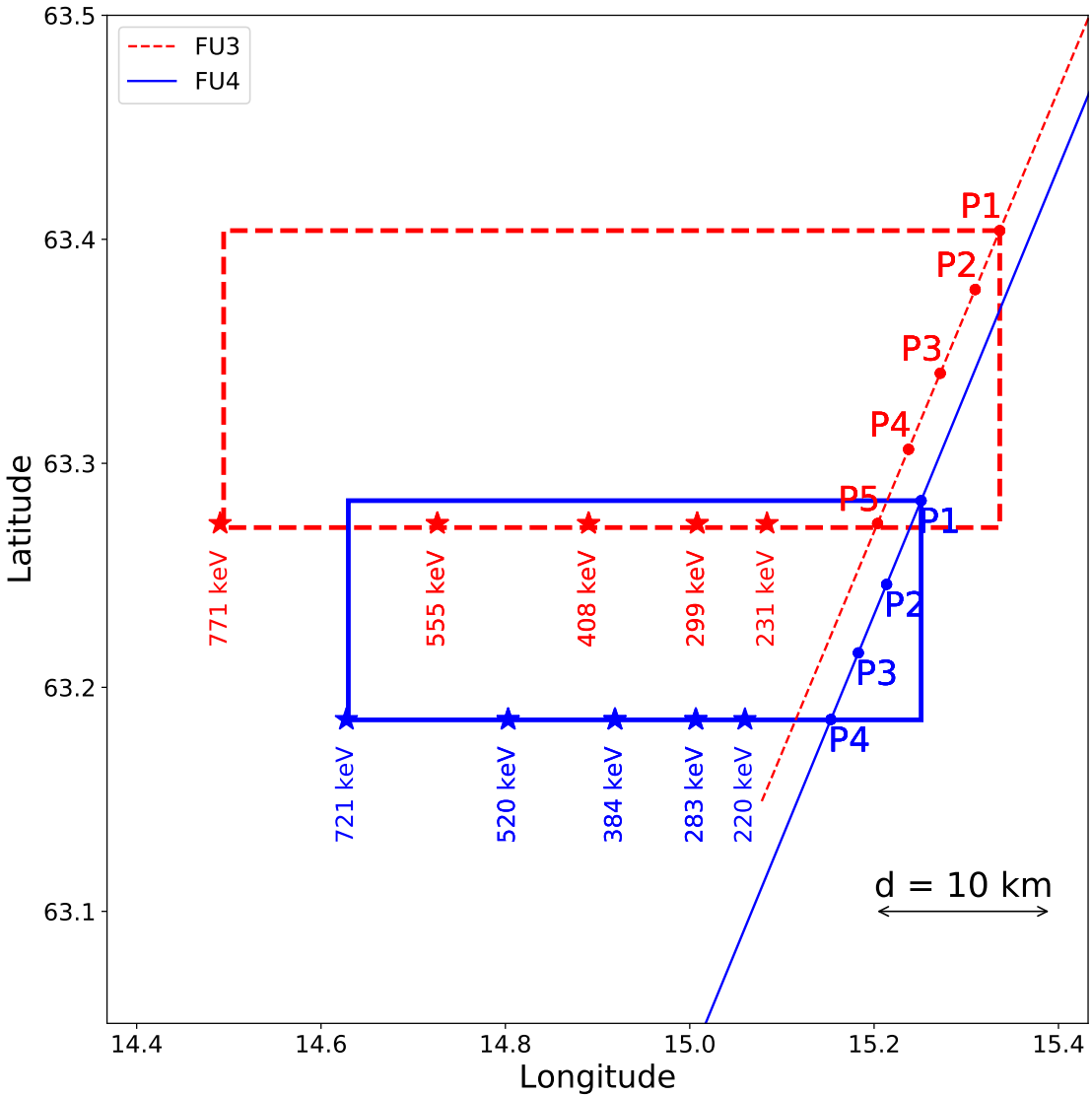


Figure 3.3: The topology of the FIREBIRD-II orbit and the multiple bounces of the microburst projected onto latitude and longitude with axis scaled to equal distance. Attributes relating to FU3 shown in red dashed lines, and FU4 with blue solid lines. The spacecraft path is shown with the diagonal lines, starting at the upper right corner. The labels P1-4 for FU4 and P1-5 for FU3 indicate where the spacecraft were when the N^{th} peak was seen in the lowest energy channel in the HiRes data. The stars with the accompanying energy labels represent the locations of the electrons with that energy that started at time of P1, and were seen at the last peak on each spacecraft. The rectangles represent the lower bound of the microburst scale size, assuming that the majority of the electrons were in the upper boundary of energy channel 4.

1346 observed. The stars in Fig. 3.3 (with labels corresponding to energy channel
 1347 boundaries) represent the locations when the microburst was observed at P1, such
 1348 that an electron of that energy would drift eastward to be seen at P5 for FU3 and P4
 1349 for FU4. Since FU3 observed more peaks it observed the larger longitudinal scale size
 1350 which is shown with the red dashed box in Fig. 3.3. FU3’s fourth energy channel’s
 1351 bounds are 555 keV and 771 keV, which correspond to longitudinal distances of 39 ± 1
 1352 km and 51 ± 1 , respectively. The uncertainty was estimated by propagating the
 1353 uncertainty in the bounce time Eq. 3.1. While the observed minimum longitudinal
 1354 scale size is dependent on FIREBIRD-II’s energy channels, the true scale size may
 1355 not be.

1356 To investigate how the microburst scale size compares to the scale sizes of chorus
 1357 waves near the magnetic equator, the microburst’s longitudinal and latitudinal scale
 1358 sizes and their uncertainties in LEO were mapped to the magnetic equator with T89.
 1359 The radial scale size (latitudinal scale mapped from LEO) was greater than 500 ± 10
 1360 km. The azimuthal scale size (longitudinal scale mapped from LEO) of 555 keV
 1361 electrons was greater than 450 ± 10 km and for the 771 keV electrons it was greater
 1362 than 530 ± 10 km. The lower bound microburst scale size is similar to the chorus
 1363 scale sizes derived by Agapitov et al. (2017, 2011), and is discussed below.

1364 Discussion and Conclusions

1365 We presented the first observation of a large microburst with multiple bounces
 1366 made possible by the twin FIREBIRD-II CubeSats. The microburst’s lower bound
 1367 LEO latitudinal and longitudinal scale sizes of 29 ± 1 km and 51 ± 1 km make
 1368 it one of the largest observed. The microburst’s LEO scale size was larger than
 1369 the latitudinal scale sizes of typical > 1 MeV microbursts reported in Blake et al.
 1370 (1996), approximately 10 times larger than reported in Dietrich et al. (2010), and

1371 approximately 2.6 times larger than other simultaneous microbursts observed by
 1372 FIREBIRD-II (Crew et al., 2016). Lastly, the scale sizes derived here were similar to
 1373 the scale sizes of \sim 15 keV microbursts observed with a high altitude balloon (Parks,
 1374 1967). No energy dependence on the minimum latitudinal scale size was observed,
 1375 while the observed energy dependence of the minimum longitudinal scale size is an
 1376 artifact of the technique we used to estimate their drift motion.

1377 The microburst scale size obtained in Section 3 and scaled to the geomagnetic
 1378 equator can be compared with the scales of chorus waves presumably responsible for
 1379 the rapid burst electron precipitation. Early direct estimates of the chorus source
 1380 scales were made by the coordinated measurement by ISEE-1, 2. The wave power
 1381 correlation scale was estimated to be about several hundred kilometers across the
 1382 background magnetic field (Gurnett et al., 1979). Furthermore, Santolik et al. (2003)
 1383 determined the correlation lengths of chorus-type whistler waves to be around 100
 1384 km based on multipoint CLUSTER Wide Band Data measurements near the chorus
 1385 source region at $L \approx 4$, during the magnetic storm of 18 April 2002. Agapitov et al.
 1386 (2017, 2011, 2010) recently showed that the spatial extent of chorus source region can
 1387 be larger, ranging from 600 km in the outer radiation belt to more than 1000 km in
 1388 the outer magnetosphere. The lower bound azimuthal and latitudinal scales obtained
 1389 in Section 3 and scaled to the magnetic equator, are similar to the whistler-mode
 1390 chorus source scale sizes reported in Agapitov et al. (2017, 2011).

1391 No wave measurements from nearby spacecraft were available at this time.
 1392 Nevertheless, during the hours before and after this observation, the Van Allen Probes'
 1393 (Mauk et al., 2013) Electric and Magnetic Field Instrument and Integrated Science
 1394 (Kletzing et al., 2013) observed strong wave power in the lower band chorus frequency
 1395 range, inside the outer radiation belt between 22 and 2 MLT. Furthermore, AE ~ 400
 1396 nT at this time, and relatively strong chorus waves were statistically more likely to

¹³⁹⁷ be present at FIREBIRD-II's MLT (Li et al., 2009b).

¹³⁹⁸ The empirically estimated and modeled t_b in this study agree within FIREBIRD-
¹³⁹⁹ II's uncertainties, confirming that the energy-dependent dispersion was due to
¹⁴⁰⁰ bouncing. The t_b curves are a proxy for field line length, and this agreement implies
¹⁴⁰¹ that they are comparable. This is expected since the magnetosphere is not drastically
¹⁴⁰² compressed at 8 MLT, but we expect a larger discrepancy near midnight, where the
¹⁴⁰³ magnetosphere is more stretched and difficult to accurately model. In future studies,
¹⁴⁰⁴ this analysis can be used as a diagnostic tool to validate field line lengths, and improve
¹⁴⁰⁵ magnetic field models.

¹⁴⁰⁶ The similarity of the microburst and chorus source region scale sizes, as well
¹⁴⁰⁷ as magnetospheric location and conditions, further support the causal relationship
¹⁴⁰⁸ between microbursts and chorus.

¹⁴⁰⁹

Acknowledgments

¹⁴¹⁰ This work was made possible with help from the FIREBIRD team, and the
¹⁴¹¹ members of the Space Sciences and Engineering Laboratory at Montana State
¹⁴¹² University for their hard work to make this mission a success. In addition, M.
¹⁴¹³ Shumko acknowledges Drew Turner for his suggestions regarding the bounce period
¹⁴¹⁴ calculations, and Dana Longcope for his proofreading feedback. The FIREBIRD-II
¹⁴¹⁵ data are available at http://solar.physics.montana.edu/FIREBIRD_II/. This analysis
¹⁴¹⁶ is supported by the National Science Foundation under Grant Numbers 0838034 and
¹⁴¹⁷ 1339414. Furthermore, the work of O. Agapitov was supported by the NASA grant
¹⁴¹⁸ NNX16AF85G.

1419

CHAPTER FOUR

1420

MICROBURST SIZE DISTRIBUTION DERIVED WITH AEROCUBE-6

1421

Contribution of Authors and Co-Authors

1422 Manuscript(s) in Chapter(s) 1

1423

1424 Author: [type author name here]

1425 Contributions: [list contributions here, single-spaced]

1426 Co-Author: [type co-author name here]

1427 Contributions: [list contributions here, single-spaced]

1428 Co-Author: [type co-author name here]

1429 Contributions: [list contributions here, single-spaced]

1430

1431

Manuscript Information

1432 [Type Author and Co-author(s) Names Here]

1433 Journal of Geophysical Research

1434 Status of Manuscript: **Officially submitted to a peer-reviewed journal**

1435 Wiley

1436

1437

Key Points

1438

- The dual AeroCube-6 CubeSats simultaneously observed > 35 keV microbursts at a variety of spatial separations ranging from 2 to ≈ 100 km.
- In low Earth orbit the majority of microbursts have a size on the order of a few tens of km.
- At the magnetic equator, the size of most microbursts corresponds to the size of whistler-mode chorus wave packets.

1444

Abstract

1445

Microbursts are an impulsive increase of electrons from the radiation belts into the atmosphere and have been directly observed in low Earth orbit and the upper atmosphere. Prior work has estimated that microbursts are capable of rapidly depleting the radiation belt electrons on the order of a day, hence their role to radiation belt electron losses must be considered. Losses due to microbursts are not well constrained, and more work is necessary to accurately quantify their contribution as a loss process. To address this question we present a statistical study of > 35 keV microburst sizes using the pair of AeroCube-6 CubeSats. The microburst size distribution in low Earth orbit and the magnetic equator was derived using both spacecraft. In low Earth orbit, the majority of microbursts were observed while the AeroCube-6 separation was less than a few tens of km, mostly in latitude. To account for the statistical effects of random microburst locations and sizes, a Monte Carlo and analytic models were developed to test hypothesized microburst size distributions. A family of microburst size distributions were tested and a Markov Chain Monte Carlo sampler was used to estimate the optimal distribution of the microburst size model

parameters. Finally, a majority of observed microbursts map to sizes less than 200 km at the magnetic equator. Since microbursts are widely believed to be generated by scattering of radiation belt electrons by whistler mode waves, the observed microburst size correlates to coherent whistler mode chorus sizes derived in prior literature.

1464

Introduction

Since the discovery of the Van Allen radiation belts in the 1960s by Van Allen (1959) and Vernov and Chudakov (1960), decades of research has made headway in understanding the various particle acceleration and loss mechanisms. One of the extensively studied mechanisms responsible for both acceleration and loss is wave-particle scattering between whistler-mode chorus waves and electrons (Abel and Thorne, 1998; Bortnik et al., 2008; Horne and Thorne, 2003; Meredith et al., 2002; Millan and Thorne, 2007; Thorne et al., 2005). Whistler-mode chorus waves are typically generated by a temperature anisotropy of low energy electrons up to tens of kiloelectronvolts (keV) and are typically found in the $\sim 0 - 12$ magnetic local times (MLT) (Li et al., 2009a,b). Whistler-mode chorus waves interact with radiation belt electrons, and are widely believed to cause electron precipitation termed microbursts (e.g. Millan and Thorne, 2007).

Microbursts are a subsecond impulse of electrons that are observed by high altitude balloons and satellites in low Earth orbit (LEO) on radiation belt magnetic footprints $\sim 4 - 8$ L-shell (L) (e.g. Anderson and Milton, 1964; Breneman et al., 2017; Crew et al., 2016; Greeley et al., 2019; Lorentzen et al., 2001a; Mozer et al., 2018; O'Brien et al., 2003; Tsurutani et al., 2013; Woodger et al., 2015), mostly in the dawn MLTs, and with an enhanced occurrence rate during disturbed magnetospheric times (Douma et al., 2017; O'Brien et al., 2003). Microburst's role as a radiation belt electron loss mechanism has been estimated to be significant, with total radiation belt

1485 electron depletion due to microbursts estimated to be on the order of a day (Breneman
 1486 et al., 2017; Lorentzen et al., 2001b; O'Brien et al., 2004; Thorne et al., 2005). These
 1487 average microburst loss estimates are not well constrained due to assumptions made
 1488 regarding the microburst precipitation region.

1489 One of the unconstrained microburst parameters that is critical to better
 1490 quantify the role of microbursts as an instantaneous loss mechanism (the number
 1491 of electrons lost per microburst) is their physical size. Historically, after the
 1492 bremsstrahlung X-ray signatures of microbursts were discovered by Anderson and
 1493 Milton (1964), numerous microburst size studies were done using other balloon flights
 1494 in the mid 1960s. Brown et al. (1965) used data from a pair of balloons separated
 1495 by 150 km, mainly in longitude, and found that one third of all microbursts observed
 1496 were temporally coincident. Trefall et al. (1966) then used the results from Brown
 1497 et al. (1965) to model the probability that a microburst will be observed by two
 1498 balloons as a function of the radius of the microburst, radius of the precipitating area
 1499 a balloon is sensitive to, and the balloon separation. Trefall et al. (1966) concluded
 1500 that the microbursts reported by Brown et al. (1965) must have had a diameter of
 1501 230 km assuming a balloon has a circular field of view with a 140 km diameter (for
 1502 electrons stopped at 100 km altitudes). Soon after, Barcus et al. (1966) used a pair of
 1503 balloons and concluded that a microburst must have a < 200 km longitudinal extent.
 1504 Then Parks (1967) used data from a single balloon with four collimated scintillators
 1505 oriented in different directions and found that the size of some mostly low energy
 1506 microbursts to have a diameter of 80 ± 28 km, and others were less than 40 km.

1507 Direct observations of microburst electrons are made by LEO spacecraft. Blake
 1508 et al. (1996) found a microburst with a size of a few tens of km using the the Solar
 1509 Anomalous and Magnetospheric Particle Explorer (SAMPEX) and concluded that
 1510 typically microbursts are less than a few tens of electron gyroradii in size (order of

1511 a few km in LEO). Recently, Dietrich et al. (2010) used SAMPEX observations in
1512 another case study and concluded that the observed microbursts were smaller than 4
1513 km. Crew et al. (2016) used the Focused Investigation of Relativistic Electron Bursts:
1514 Intensity, Range, and Dynamics (FIREBIRD-II) CubeSats and found an example of
1515 a microburst larger than 11 km. Lastly, Shumko et al. (2018) also used FIREBIRD-II
1516 to identify a microburst with a size greater than 51 ± 1 km. If anything, the large
1517 variance in prior results imply that there is a distribution of microburst scale sizes
1518 which this study aims to estimate.

1519 Besides addressing the instantaneous radiation belt electron losses due to
1520 individual microbursts, the microburst size distribution is useful to identify the wave
1521 mode(s) responsible for scattering microbursts. By mapping the microburst size
1522 distribution in LEO to the magnetic equator it can be compared to the wave sizes
1523 estimated in prior literature. This comparison can be used to identify the waves and
1524 their properties (e.g. amplitude or coherence) responsible for scattering microburst
1525 electrons.

1526 This paper addresses these two questions by expanding the prior microburst
1527 size case studies by analyzing microburst observations over a three year time period
1528 to estimate the microburst size distribution in LEO and the magnetic equator. The
1529 twin AeroCube-6 (AC6) CubeSats are utilized for this study because they were ideally
1530 equipped to observe microbursts simultaneously over a span of three years while their
1531 total separation varied between 2 and 800 km, mostly in latitude (in-track in orbit).
1532 This paper first describes the AC-6 mission, including their orbit and instrumentation
1533 in section 4. Section 4 develops the methodology used to identify microbursts observed
1534 by each spacecraft and how they were combined to make a list of simultaneously
1535 observed microbursts. Section 4 describes the methodology used to estimate the
1536 microburst size distributions in LEO and the magnetic equator as a function of AC6

1537 separation. Then a model is developed to shed light on how the compounding effects of
 1538 a hypothesized microburst shape, size distribution, and random microburst locations
 1539 will be observed by AC6, a two-point measurement platform. Lastly, in section 4
 1540 we discuss these results and compare the microburst sizes estimated here to the size
 1541 distribution of the whistler-mode chorus waves that are believed to cause microbursts.

1542

Instrumentation

1543 The AC6 mission consists of a pair of 0.5U (10x10x5 cm) CubeSats built by
 1544 The Aerospace Corporation and launched on June 19th, 2014 into a 620 x 700 km,
 1545 98° inclination orbit. The two satellites, designated as AC6-A and AC6-B, separated
 1546 after launch and drifted apart. Both AC6 units have an active attitude control system
 1547 which allows them to adjust the atmospheric drag experienced by each AC6 unit by
 1548 orienting their solar panel “wings” with respect to the ram direction. By changing
 1549 their orientation, AC6 was able to achieve fine separation control and maintain a
 1550 separation between 2-800 km. Figure 4.1a shows the AC6 separation for the duration
 1551 of the mission. Figure 4.1b shows where AC6 was taking 10 Hz data simultaneously
 1552 as a function of L and MLT which highlights that most data was taken at 8-12 MLT,
 1553 an ideal local time for observing microbursts. Lastly Fig. 4.1b shows that the AC6
 1554 orbit was roughly dawn-dusk, sun-synchronous and precessed only a few hours in
 1555 MLT over a three year period.

1556 Each AC6 unit is equipped with three Aerospace microdosimeters (licensed to
 1557 Teledyne Microelectronics, Inc). The dosimeter used for this study is dos1 and is
 1558 identical on both AC6 units. Dos1 has a 35 keV electron threshold and all dosimeters
 1559 sample at 1 Hz in survey mode, and 10 Hz in burst mode in the radiation belts. More
 1560 detailed technical information on AC6 is described in O’Brien et al. (2016b).

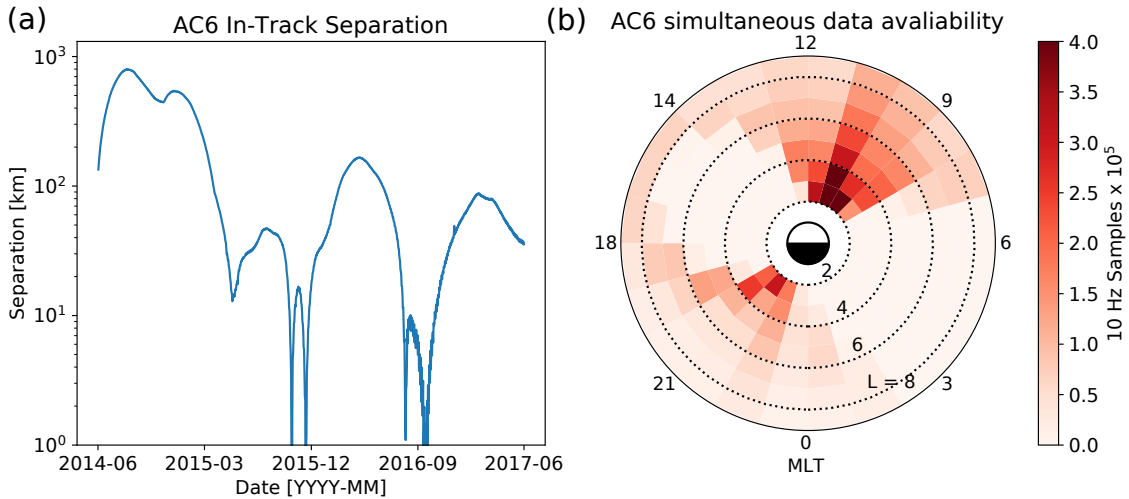


Figure 4.1: AC6 mission properties for (a) spacecraft separation and (b) number of simultaneous quality 10 Hz samples as a function of L and MLT.

1561

Methodology

1562 Microburst Detection

1563 The first step to find microbursts observed simultaneously by AC6 is to identify
 1564 them on each individual spacecraft. Microbursts were detected with two different
 1565 methods that yielded quantitatively similar results. The first method is the burst
 1566 parameter (O'Brien et al., 2003). This algorithm has been successfully used in other
 1567 microburst studies, mainly with the microbursts observed by SAMPEX (e.g. Blum
 1568 et al., 2015; Douma et al., 2017; O'Brien et al., 2003). For AC6, a burst parameter
 1569 threshold of 5 was determined to be a good trade-off between false positive and false
 1570 negative microburst detections. Another microburst detection algorithm based on
 1571 wavelet spectra frequency filtering was developed and the resulting list of microbursts
 1572 is similar to the list from the burst parameter.

1573 With the two microburst detection lists in hand, data cleaning to remove
 1574 microburst-like transmitter noise was necessary. The transmitters on AC6 can

cause unphysical count impulses in the dosimeters that resembles periodic trains of microbursts. One source of transmitter noise was observed at times when AC6 was in contact with the ground stations above the US for data downloads and commanding, thus the microburst detections made above the US that were mostly at low L were discarded.

Another source of noise is crosslink transmissions between AC6-A and AC6-B. These transmissions occurred when either spacecraft transitioned from the survey mode to 10 Hz mode. This noise is sometimes not caught by the data quality flag, so the following empirically-derived criteria were developed to remove those detections. The dosimeter with a 250 keV nominal electron threshold, dos2, was used because it had a nearly identical response to noise while rarely responded to microbursts. Since the transmitter noise is very periodic with a ≈ 0.2 s period, cross-correlation (CC) and autocorrelation (AC) methods were applied to the dos1 and dos2 time series. Detections were discarded if the following two criteria were met: either dos1 or dos2 time series had a AC peak at a 0.2 or 0.4 s lag and the dos1-dos2 CC was greater than 0.9. The AC lag criteria alone sometimes falsely removed legitimate trains of microbursts, so the second criteria insured that the detection was removed if there was also an unphysically high correlation across an order of magnitude in energy.

The lists of microbursts observed individually by AC6 were then merged into a list of temporally correlated microbursts, i.e. microbursts that were observed simultaneously by both AC6 units, with the following procedure. The general idea is that a microburst detected by one spacecraft will cross-correlate well with the time series from the other spacecraft if it observed a similar microburst, and poorly if there was no microburst observed by the other spacecraft. Each microburst detection made by either spacecraft was cross-correlated with the time series from the other spacecraft whether or not a microburst was observed by the other spacecraft. Cross-

1601 correlation windows with 1 and 1.2 s widths were chosen with slightly different
 1602 window sizes to account for random count variation due to Poisson noise. Microbursts
 1603 detections that had a cross-correlation greater than 0.8 were considered temporally
 1604 coincident. This CC threshold was chosen as it is low enough to accept user-identified
 1605 temporally coincident microbursts superposed with noise, and high enough to reject
 1606 most non-coincident events. Figure 4.2, panels (a), (c), (e), and (g) show examples
 1607 of microbursts observed by both AC6 units when they were separated by 5, 16, 37,
 1608 and 69 km, respectively.

1609 The last criteria requires that the temporal CC must be greater than the spatial
 1610 CC + 0.3. The spatial CC was calculated by shifting one spacecraft's time series
 1611 by the in-track lag to cross-correlate in the same spatial location, i.e. latitude.
 1612 This criteria was applied to remove curtains, stationary structures observed by AC6
 1613 that are narrow in latitude (Blake and O'Brien, 2016) that can be misidentified as
 1614 microbursts. Figure 4.2, panels (b), (d), (f), and (h) show the shifted time series to
 1615 confirm that there were no spatially correlated, non-microburst structures present.
 1616 Lastly the merged microburst list was spot checked by two authors to remove poorly
 1617 correlated and any duplicate events. After filtering out transmitter noise and applying
 1618 the CC criteria, 662 simultaneous microburst detections were found and used in this
 1619 study.

1620 Microburst Size Distribution in LEO and Magnetic Equator

1621 The temporally coincident microbursts, which from now on will be referred to
 1622 as microbursts, are now used to estimate the fraction of microbursts observed above
 1623 AC6 separation, s . When AC6 observes a microburst at s , the microburst's size
 1624 must be greater than s . This fact, along with the arguments presented in Section 4
 1625 in Joy et al. (2002) who studied the most probable Jovian magnetopause and bow

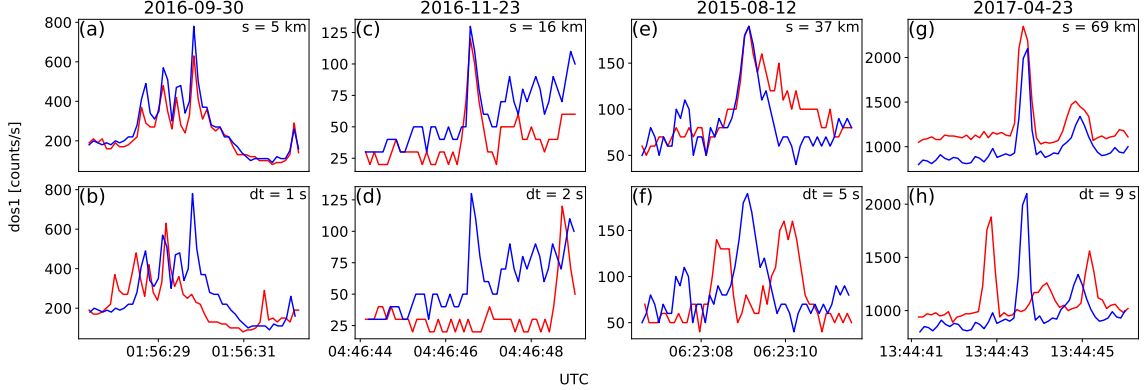


Figure 4.2: Examples of > 35 keV microbursts observed simultaneously by AC6-A in red and AC6-B in blue. Panels (a), (c), (e), and (g) show the temporally-aligned time series when AC6 were separated by $s = 5, 16, 37$, and 69 km, respectively. The corresponding panels (b), (d), (f), and (h) show the spatially-aligned time series which is made by shifting the AC6-A time series in the above panels by the in-track lag (annotated with dt) that show any spatially correlated structures. The clear temporal correlation and lack of spatial correlation demonstrates that these events are microbursts.

shock stand off distances, are used to investigate the dependence of the number of microbursts observed above s , as a function of s . This dependence is the microburst complementary cumulative distribution function $\bar{F}(s)$.

The cumulative fraction of microbursts observed above s is the ratio of $N(s)$, the normalized number of microbursts observed above s , to $N(0)$, the total number of microbursts observed

$$\bar{F}(s) = \frac{N(s)}{N(0)} \quad (4.1)$$

where $N(s)$ is defined by

$$N(s) = \sum_{i=s}^{\infty} n_i \left(\frac{S_{max}}{S_i} \right) \quad (4.2)$$

where n_i is the number of microbursts observed by AC6 in i th separation bin. The normalization term S_{max}/S_i is a ratio of the number of 10 Hz samples in

1632 the most sampled separation bin to the number of samples in the ith bin. This
 1633 normalization factor corrects AC6's non-uniform sampling in separation, thus $\bar{F}(s)$
 1634 can be interpreted as the fraction of microbursts observed above s assuming AC6
 1635 sampled evenly in separation. Microburst $\bar{F}(s)$ in LEO is shown by the black curve
 1636 in Fig. 4.3a for $4 < L < 8$ and split into one L-wide bins with the colored curves. The
 1637 separation bin width used in Fig. 4.3 is 5 km. To check for bias in $\bar{F}(s)$ due to the
 1638 choice of separation bins, $\bar{F}(s)$ was resampled using other bin widths and offsets. Bin
 1639 widths as large as 20 – 30 km and bin offsets did not qualitatively effect the curves
 1640 in Fig. 4.3a. The normalization i.e., the number of 10 Hz samples in each separation
 1641 bin, is shown in 4.3c.

1642 The overall trend in Fig. 4.3a shows a sudden cumulative probability drop off,
 1643 followed by a shoulder up to $s \approx 70$ km where $\bar{F}(s)$ drops to nearly zero. A large
 1644 negative gradient of $\bar{F}(s)$ at some separation implies that microbursts must be smaller
 1645 than that separation. To quantify this, Fig. 4.3b shows the microburst probability
 1646 density function (PDF), calculated by differentiating $\bar{F}(s)$. The microburst PDF
 1647 shows a peak at $s < 30$ km as well as a peak between 70 – 80 km separation. These
 1648 PDF peaks are evidence of a sub 30 km microburst population and larger microbursts
 1649 observed up 70–80 km separations. The shaded region around the black curves in Fig.
 1650 4.3a-b shows the standard error due to counting statistics. The uncertainty due to
 1651 false coincidence events i.e. two unrelated microbursts lining up in time by random
 1652 chance was also considered. The microburst duty cycle in a one minute window
 1653 ($\approx 1 L$) around each microburst was calculated. The false coincidence probability is
 1654 the square of the duty cycle and was found to be less than 5% for the majority of
 1655 microbursts. The false coincidence probability for each microburst was then used to
 1656 randomly remove microbursts and $\bar{F}(s)$ was recalculated in 10^4 trials. The spread in
 1657 the $\bar{F}(s)$ trial curves with microbursts randomly removed was much smaller than the

1658 uncertainty due to counting statistics alone.

1659 To compare the microburst size to the size of their hypothesized progenitor
1660 waves, the spacecraft locations during observed microbursts were mapped to the
1661 magnetic equator using the Olson-Pfitzer magnetic field model (Olson and Pfitzer,
1662 1982) which is implemented with a Python wrapper for IRBEM-Lib (Boscher et al.,
1663 2012). As previously stated, a microburst observed in LEO has a size larger than
1664 the spacecraft separation, hence that microburst would also have a size larger than
1665 the spacecraft separation after it was mapped to the magnetic equator. Thus
1666 the procedure to estimate $\bar{F}(s)$ is identical to the LEO size distribution but with
1667 a different normalization. The normalization factors were calculated by mapping
1668 every quality AC6 sample to the magnetic equator and binning them by equatorial
1669 separation into 100 km wide bins. Figure 4.4 shows the equatorial microburst size
1670 distribution in the same format as Fig. 4.3. The equatorial PDF trend is similar to
1671 LEO and most of the microbursts were observed when the AC6 equatorial separation
1672 was less than 200 km.

1673 The results in Figs. 4.3 and 4.4 show the fraction of microbursts observed above a
1674 spacecraft separation and do not fully represent the microbursts size distribution due
1675 to the compounding effects from the range of microburst sizes and random locations
1676 of microbursts with respect to AC6 i.e. even if the microburst size is much larger than
1677 the AC6 separation, some fraction of those microbursts will be only observed by one
1678 AC6 spacecraft. Thus modeling is necessary to capture the compounding influence
1679 of these statistical effects on AC6.

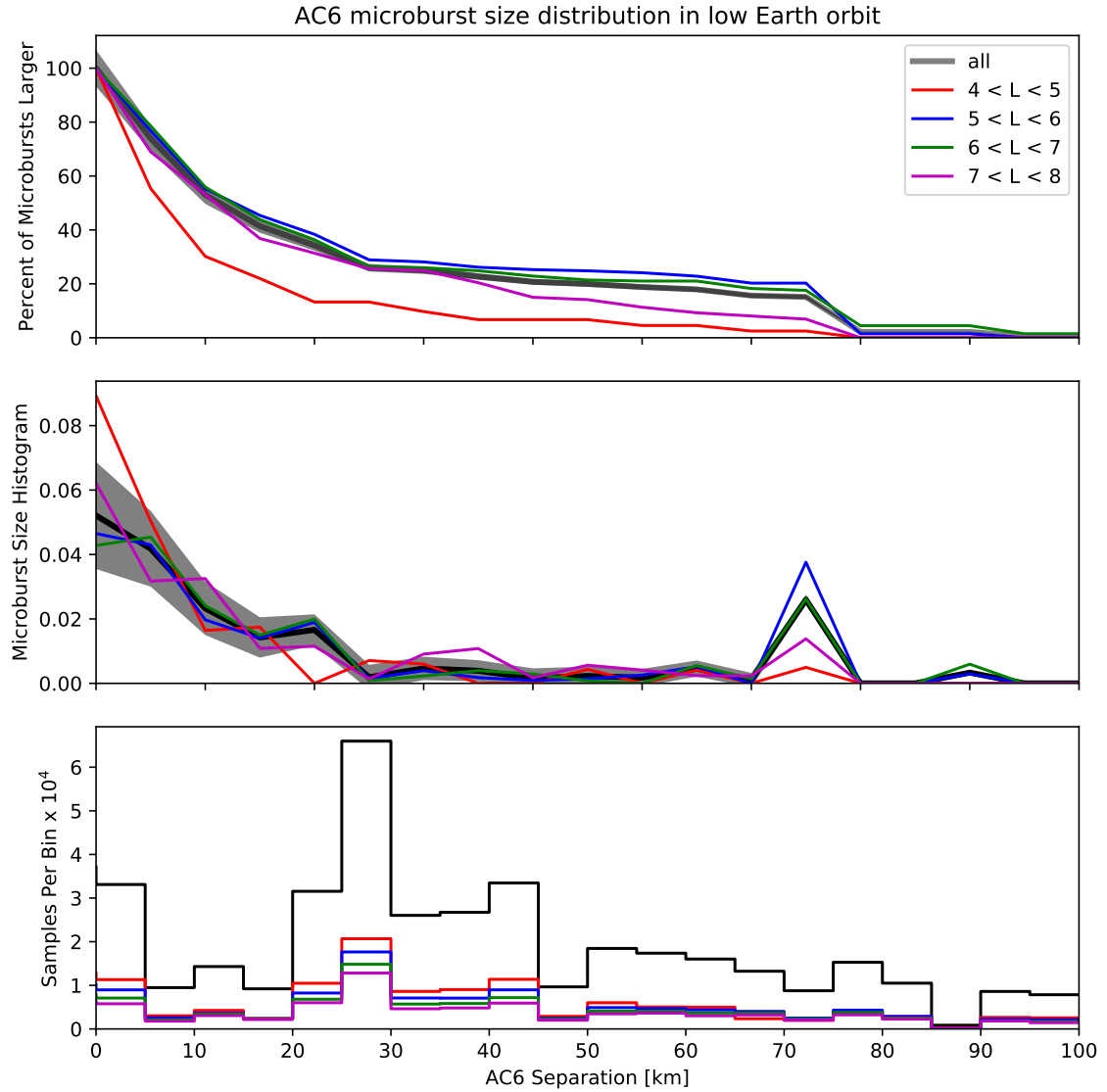


Figure 4.3: Microburst size distribution in low Earth orbit. Panel (a) shows the percent of microbursts observed above that separation after normalizing for the uneven AC6 sampling in separation. Panel (b) shows the microburst probability density (size histogram) as a function of separation. Lastly, panel (c) shows the normalization, i.e. number of simultaneous samples AC6 observed as a function of separation. The colored lines show the distributions binned by L , and the thick black curve for the entire radiation belt ($4 < L < 8$). The gray shading around the black curve shows the uncertainty due to counting statistics.

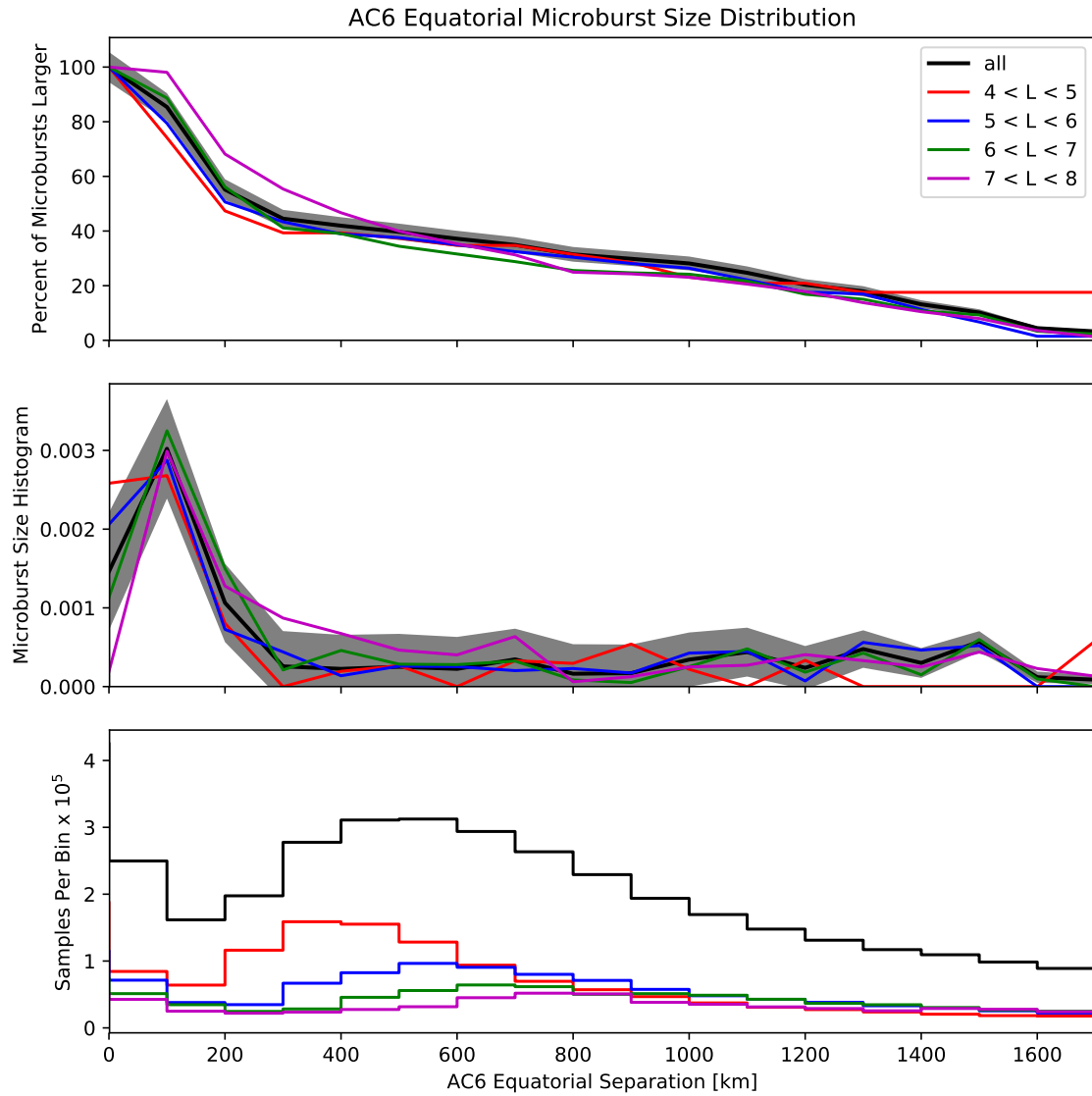


Figure 4.4: Microburst size distribution mapped to the magnetic equator in the same format as Fig. 4.3.

1680

Modeling the Distribution of Microburst Sizes1681 Monte Carlo and Analytic Models to Calculate $\bar{F}(s)$

1682 To account for the effects due to microbursts randomly occurring around
 1683 AC6 with an unknown distribution of microburst sizes, Monte Carlo (MC) and
 1684 analytic models were developed. These models assume a hypothesized distribution
 1685 of microburst sizes expressed with a probability density function $p(d|\theta)$ where θ are
 1686 the dependent variables, and a microburst footprint shape to estimate $\bar{F}(s)$. The
 1687 microburst footprint is assumed to be circular with a diameter d . $p(d|\theta)$ can be
 1688 understood as “the probability of observing a microburst of diameter d , given the
 1689 parameters θ ”. Various microburst size distributions were considered: a one-size and
 1690 two-size microburst populations, and continuous $p(d|\theta)$ such as Maxwell, Weibull,
 1691 and log-normal.

1692 The Monte Carlo model is the most intuitive. It first randomly scatters 10^5
 1693 microburst centers in a 400×400 km grid around AC6. Then each microburst
 1694 center was assigned a diameter, randomly picked from a $p(d|\theta)$ distribution after
 1695 θ parameters were specified. Spacecraft A is placed at the origin, and spacecraft B
 1696 is placed along the positive y-axis at distances from spacecraft A corresponding to
 1697 the AC6 separation bins used in Section 4. Then for each spacecraft B location, the
 1698 number of microbursts that encompass both spacecraft was counted. The modeled
 1699 fraction of microbursts observed above s is then

$$\bar{F}(s) = \frac{\sum_{\substack{i>s \\ i>0}} n_i}{\sum_{i>0} n_i}. \quad (4.3)$$

1700 where as before the number of microbursts observed by both spacecraft in the i th bin

₁₇₀₁ is n_i .

The analytic model, while identical to the MC model, highlights the geometrical concepts connecting $p(d|\theta)$ and $\bar{F}(s)$ with geometry arguments similar to Trefall et al. (1966). For a microburst with $d = 2r \geq s$, there is an area between AC6 where that microburst will be observed by both spacecraft if the microburst's center lands there. Figure 4.5a-c shows this geometry with the two spacecraft indicated with black dots with varying relations between r and s . All microbursts whose center lies inside the circular area of radius r surrounding either spacecraft will be observed by that spacecraft. If it exists, the intersection of the two circular areas around both spacecraft defines another area, $A(r, s)$ where a microburst will be observed by both spacecraft if the microburst center lands there. This area can be calculated using the circle-circle intersection area equation,

$$A(r, s) = 2r^2 \cos^{-1} \left(\frac{s}{2r} \right) - \frac{s}{2} \sqrt{4r^2 - s^2}. \quad (4.4)$$

₁₇₀₂ Example geometries where $A(r, s) > 0$ are shown in Fig. 4.5b and c. With this
₁₇₀₃ conceptual model and $A(r, s)$, the analytic form of $\bar{F}(s)$ can be found and is derived
₁₇₀₄ in the Supporting Information (SI) Text S1. To demonstrate the effects of random
₁₇₀₅ microburst locations near AC6, examples of the analytic and Monte Carlo $\bar{F}(s)$ curves
₁₇₀₆ are shown in Fig. 4.5d for a one-size, $d = 40$ km microburst population.

₁₇₀₇ Methods for estimating optimal θ parameters

₁₇₀₈ At this stage we have all of the ingredients to calculate $\bar{F}(s)$ given a prescribed
₁₇₀₉ $p(d|\theta)$. For each $p(d|\theta)$ tested, the optimal θ parameters are estimated in this study
₁₇₁₀ using the traditional least squares regression and Bayesian inference. While we
₁₇₁₁ report the θ parameters that minimize least squares, this section focuses on Bayesian
₁₇₁₂ inference because it seamlessly incorporates statistical uncertainty in the data. The

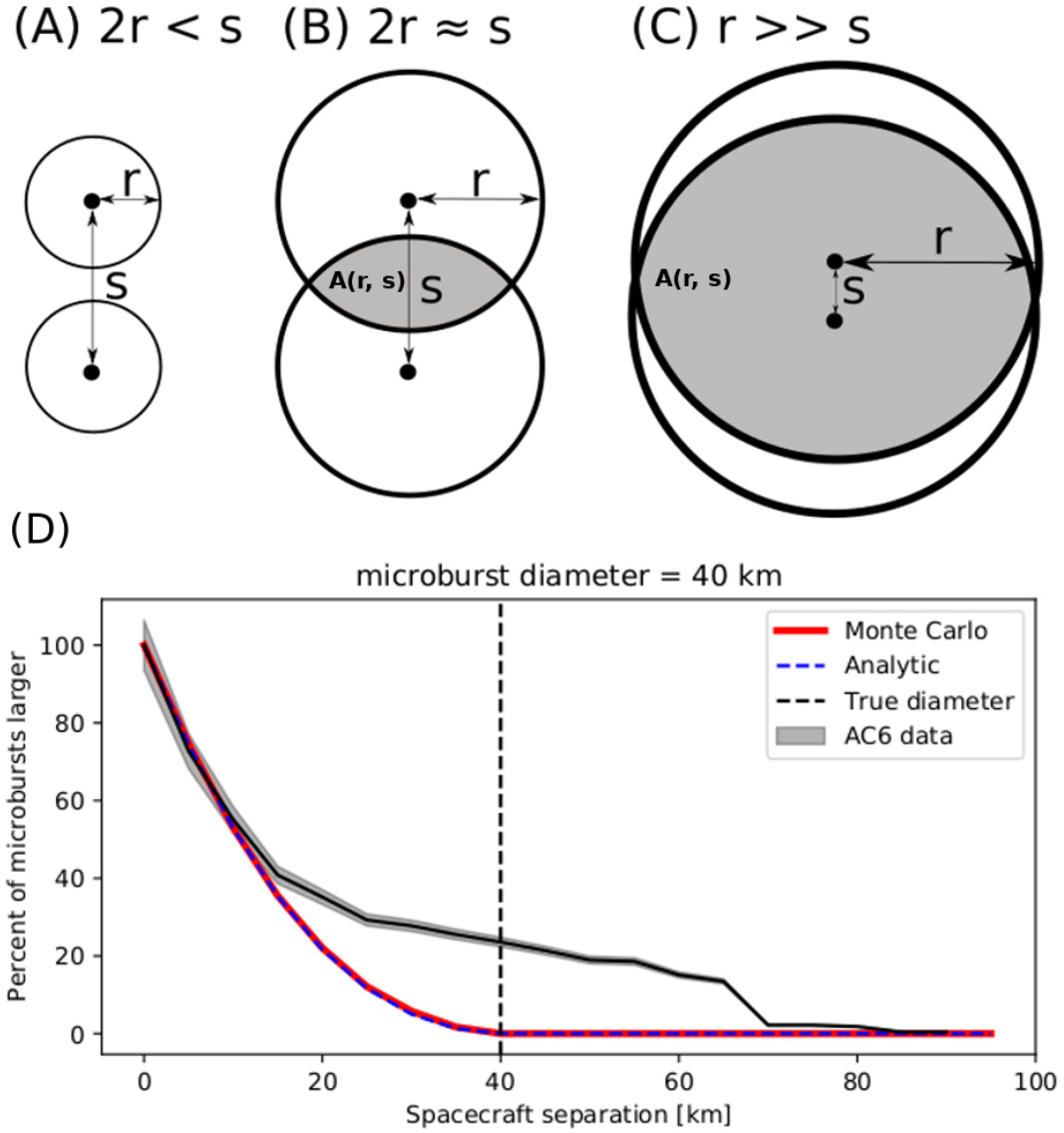


Figure 4.5: Panels A-C show the varying geometries of the analytic model. The two spacecraft are shown as black dots. The enclosing black circle around each spacecraft bounds the area where a microburst will be observed by one or both AC6 units if the microburst's center lies inside the circle. Panel (A) shows the case where microburst diameter is smaller than the AC6 separation and all microbursts will be observed by either unit A or B and never simultaneously. Panel (B) shows the intermediate case where the microburst diameter is comparable to the AC6 separation and some fraction of microbursts will be observed simultaneously. The fraction of the microbursts simultaneously observed is proportional to the circle intersection area $A(r, s)$ and is shown with grey shading. Panel (C) shows the case where the microburst diameter is much larger than the spacecraft separation and nearly all microbursts will be observed by both spacecraft. Lastly panel (D) shows $\bar{F}(s)$ from the AC6 data with a solid black line, and modeled MC and analytic $\bar{F}(s)$ curves for a single-sized microburst distribution with $d = 40$ km.

1713 uncertainty in the data is then propagated to θ which is then no longer an optimal
 1714 value, rather a distribution of values that is consistent with the observations and its
 1715 uncertainty.

1716 Bayesian inference is rooted in Bayes theorem of conditional probability. Given
 1717 the observed $\bar{F}(s)$ as y , and model's dependent variables as θ , Bayes theorem can be
 1718 written as

$$p(\theta|y) = \frac{p(y|\theta)p(\theta)}{p(y)}. \quad (4.5)$$

1719 $p(\theta)$ is the distribution of θ that describe our prior level of knowledge about that
 1720 parameter e.g. from earlier microburst size studies, a microburst size must less than
 1721 500 km in LEO. This is called the prior which is quantified by a PDF such as normal,
 1722 uniform, etc. Next term is the likelihood, $p(y|\theta)$, the conditional probability of
 1723 obtaining y given a particular θ . The likelihood probability is a probabilistic penalty
 1724 function that quantifies the discrepancy between the modeled and observed $\bar{F}(s)$ in
 1725 terms of the standard error. The resulting PDF of θ s consistent with the observations
 1726 is $p(\theta|y)$ known as the posterior distribution. The posterior is an update to our prior
 1727 distributions, modified by the likelihood i.e. the data and its uncertainties. Here, the
 1728 posterior is used to make inferences regarding the range of θ parameters that generate
 1729 a $\bar{F}(s)$ that is consistent with the observations. The last parameter in Bayes theorem
 1730 is $p(y)$. $p(y)$ is the marginal likelihood (evidence) that describes the probability of
 1731 obtaining y after marginalizing over all prior variables. Calculation of $p(y)$ is difficult,
 1732 and often not necessary for model parameter estimation.

1733 With all of the above terminology, the important takeaway is that the posterior
 1734 distribution for each model parameter is interpreted as the range of our model's
 1735 dependent parameters that are consistent with the observations. A 95% credible

1736 interval (CI) for each model parameter is reported here that is interpreted as:
 1737 assuming a hypothesized $p(d|\theta)$, there is a 95% probability that the true θ is inside
 1738 the CI. To sample the posterior distribution, the θ parameter space is explored with
 1739 a Markov Chain Monte Carlo (MCMC) sampler. In a nutshell a Markov Chain is a
 1740 process that samples random variables that depend on only the previous state of those
 1741 random variables. Hence a MCMC sampler is a Monte Carlo sampler that samples
 1742 the θ parameter space by picking random θ values based on the previous state of θ .

1743 The first and one of the most popular MCMC is the Metropolis-Hastings
 1744 sampler (Hastings, 1970; Metropolis et al., 1953). While the Metropolis-Hastings
 1745 sampler is explained in detail in Metropolis et al. (1953) and Hastings (1970) and
 1746 a good introduction given in Sambridge et al. (2006) as well as Sharma (2017), a
 1747 brief overview is warranted. The Metropolis-Hastings sampler samples the posterior
 1748 distribution in N trials. Once an initial set of θ is randomly picked from the prior,
 1749 the i^{th} trial involves the following steps. First calculate the posterior probability for
 1750 θ_i . Then pick a proposal θ_{i+1} to jump to, randomly picked near θ_i in parameter space.
 1751 If the θ_{i+1} posterior probability is higher than θ_i , the MCMC accepts the proposal
 1752 and moves to θ_{i+1} . If the posterior probability of θ_{i+1} is smaller than θ_i , there is a
 1753 random chance that θ_{i+1} will be accepted or rejected (if rejected, $\theta_{i+1} = \theta_i$ and a
 1754 new proposal is generated). This accept/reject criteria allows the sampler to trend
 1755 to more probable θ while also exploring the neighboring regions. After the N trials,
 1756 a histogram is made using the accepted θ s to produce the posterior distribution for
 1757 each model parameter.

1758 Estimating optimal parameters for various microburst size models

The MCMC sampler is first used to test the simplest microburst size model where
 all microbursts are one size and the MCMC will estimate that size. The microburst

size PDF for this model can be expressed as

$$p(d|d_0) = \delta(d - d_0) \quad (4.6)$$

where δ is the Dirac Delta function and d_0 is the diameter of all microbursts according to this model. The range of d that are consistent with the observed $\bar{F}(s)$ is shown in Fig. 4.6. Assuming this model, there is a 95% probability that the microburst diameter is between 38 and 129 km. As a sanity check the optimal size that minimizes least squares is 73 km.

A slight generalization of the one-size model is a two-size microburst population model that assumes the following microburst PDF

$$p(d|d_0, d_1, a) = a\delta(d - d_0) + (1 - a)\delta(d - d_1) \quad (4.7)$$

where the diameters of the two microburst populations are given by d_0 and d_1 and a is the parameter that quantifies the relative fractions of the two populations. The result of this model is shown in Fig. 4.7. The fit is slightly better than the one-size model, although that is to be expected given two more free model parameters. A majority, 98 %, of microbursts, have a diameter between 12 and 47 km with a rare population with a diameter between 76 and 234 km. The set of parameters that minimize least squares is 99.5 % of microbursts are small with a size of 21 km and the remaining 0.5 % of microbursts have a 140 km size.

Other, continuous PDFs were tested including: Maxwellian (Maxwell – Boltzmann), log-normal, and Weibull. The range of model parameters that are consistent with the observed $\bar{F}(s)$ are presented in the SI text S2. These distributions were chosen because they have the following properties that are most realistic: they are continuous, approach 0 in the limit as $r \rightarrow 0$ (lower bound microburst

1777 size is ultimately limited by the electron gyroradius), and can be symmetrical or
 1778 asymmetrical.

1779

Discussion

1780 The LEO microburst $\bar{F}(s)$ estimated in section 4 shows that a majority of
 1781 coincident microbursts were observed by AC6 when they were separated by less than
 1782 a few tens of km. This conclusion is consistent with prior literature and most similar
 1783 to Parks (1967) who reported that many > 15 keV microbursts are less than 40 km
 1784 in diameter while others were on average 80 ± 28 km in diameter. Furthermore, these
 1785 results are similar to the bouncing packet example shown in Blake et al. (1996) with
 1786 a size of “at least a few tens of kilometers”. The relatively small number of large
 1787 > 70 km microbursts observed by AC6 fit in well with the results from Barcus et al.
 1788 (1966) and Brown et al. (1965), although the AC6 separation is mostly latitudinal
 1789 while Barcus et al. (1966) and Brown et al. (1965) used data from pairs of balloons
 1790 separated predominantly in longitude.

1791 Without knowledge of the microburst shape, a direct comparison between the
 1792 AC6 and balloon observations is difficult. Trefall et al. (1966) discussed how a
 1793 hypothetical circular microburst at the scattering location near the magnetic equator
 1794 will be stretched into an ellipse with a semi-major axis in the longitudinal direction.
 1795 This stretching effect should be explored further as it introduces an ambiguity from
 1796 the eccentricity of the ellipse that prevents a direct latitudinal and longitudinal
 1797 comparison.

1798 When comparing our results to more recent studies, the AC6 microburst size
 1799 distribution is much larger than the sizes reported in Dietrich et al. (2010) who
 1800 used very low (VLF) frequency transmission paths and SAMPEX to conclude that
 1801 microbursts must be smaller than 4 km from a small number of microbursts observed

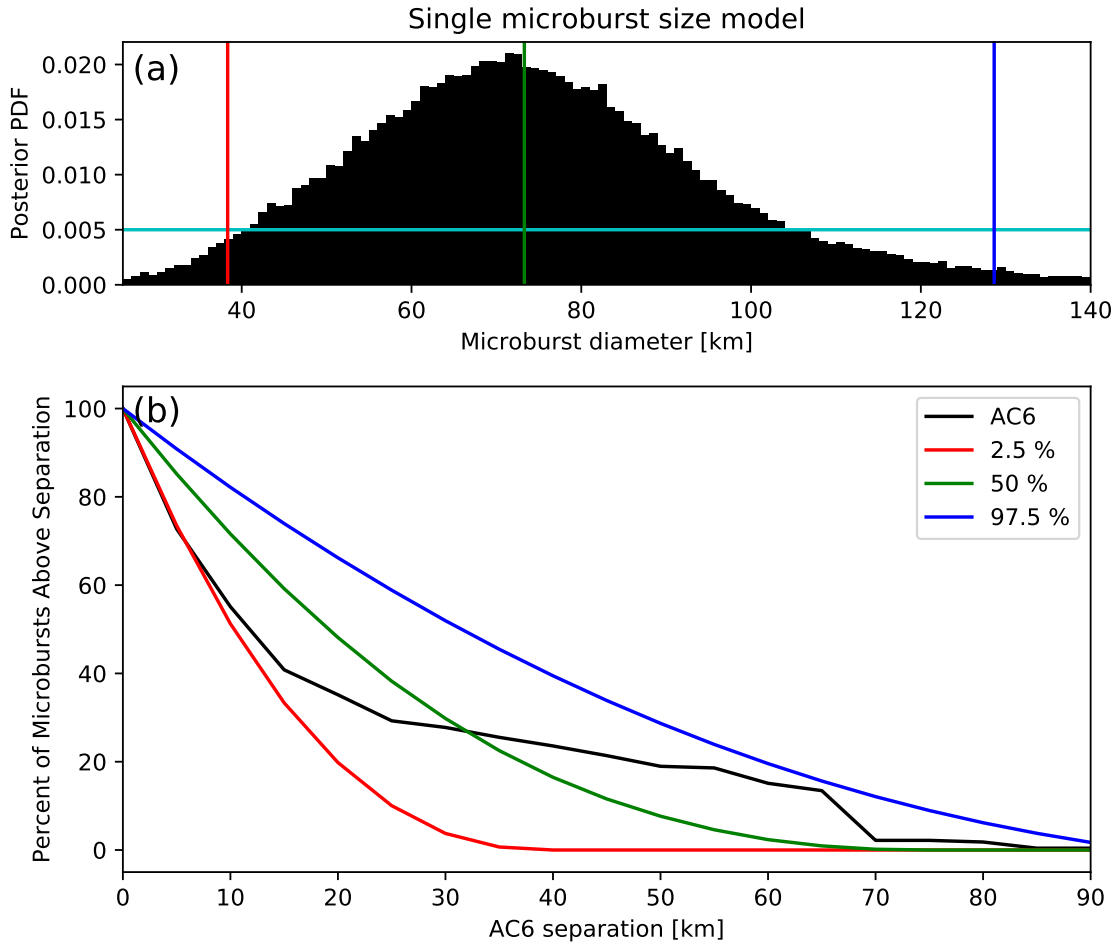


Figure 4.6: Range of plausible microburst sizes assuming all microbursts are one fixed size. Panel (a) shows the posterior probability density function of microburst diameters in black. The red, green, and blue vertical lines at 38, 73, and 129 km represent the 2.5, 50, and 97.5 posterior percentiles, respectively. A uniform prior between 0 and 200 km was assumed for this MCMC run and is shown in cyan. Panel (b) shows the percent of microbursts observed above an AC6 separation for $4 < L < 8$ in black. The 2.5, 50 and 97.5 size percentiles were estimated from the posterior and plotted in red, green, and blue curves, respectively.

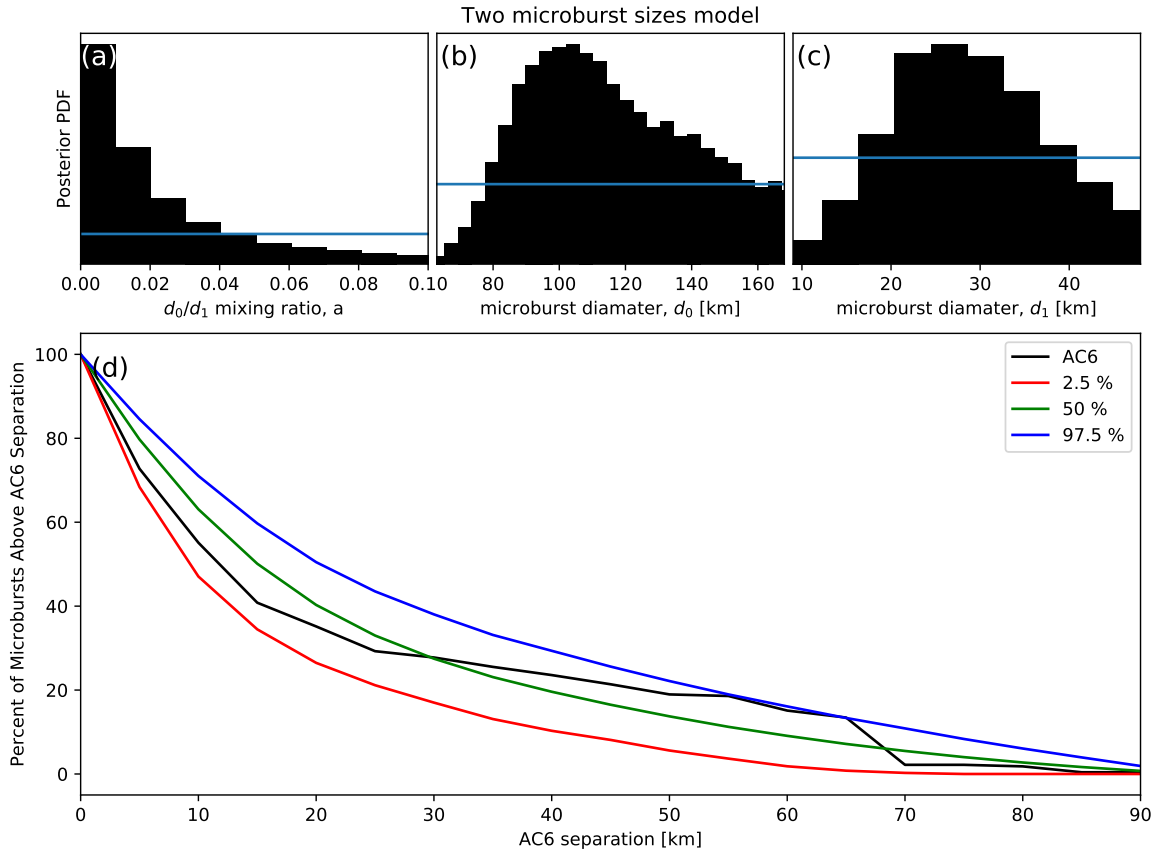


Figure 4.7: Plausible microburst percent curves assuming microburst size distribution is bimodal consisting of two sizes d_0 and d_1 with a mixing term that quantifies the relative occurrence of the d_0 to d_1 microburst populations. Panel (a) shows the posterior distribution for the microburst population mixing term, a with a median value of 0.02. The a prior was uniform between 0 and 0.2. Panel (b) shows the posterior distribution for d_0 , the larger microburst population estimated with a uniform prior between 50 and 200 km and the posterior median diameter of 122 km. Panel (c) shows the posterior distribution for d_1 , the smaller microburst population, estimated using a uniform prior between 0 and 50 km with a median diameter of 28 km. Panel (d) is similar to Fig. 4.6b and shows the AC6 microburst fraction for $4 < L < 8$ in black. A set of 1000 random parameter triples (a , d_0 , and d_1) were drawn from the posterior and used to generate a family of $\bar{F}(s)$ curves. At each s the range of consistent $\bar{F}(s)$ were quantified by the 2.5, 50 and 97.5 percentiles and shown with the red, green, and blue curves, respectively.

1802 during one SAMPEX radiation belt pass. Dietrich et al. (2010) arrived at their
 1803 conclusion by looking for temporal coincidence of microbursts and FAST events,
 1804 subsecond VLF transmission perturbations, but the connection between FAST events
 1805 and microbursts is not well understood. Lastly, our results are consistent with
 1806 FIREBIRD-II observations of a > 11 km microburst reported by Crew et al. (2016),
 1807 and the minority of microbursts observed by AC6 up to $s \approx 70$ km are consistent
 1808 with the > 51 km bouncing packet microburst reported in Shumko et al. (2018).

1809 The microburst PDF shown in Fig. 4.3b suggests that the microburst size
 1810 distribution is bimodal. This has been suggested before by Blake et al. (1996) who
 1811 noted that the > 150 keV and > 1 MeV microbursts are not always well correlated
 1812 e.g. Fig. 10 in Blake et al. (1996). The quality of the AC6 data is insufficient to
 1813 definitively conclude that there are two distinct microburst populations. The different
 1814 microburst population hypothesis can be better tested with an AC6-like mission with
 1815 better energy resolution and homogeneous MLT coverage.

1816 The model results from section 4 emphasize that care must be taken when
 1817 comparing the $\bar{F}(s)$ curves observed by AC6 and the true microburst size distribution
 1818 due to the compounding effect of an unknown microburst size distribution, unknown
 1819 microburst shape, and random microburst locations near AC6. By assuming there is
 1820 only one microburst size, the results in Fig. 4.6 suggest that there is a 95% probability
 1821 that the microburst diameter is somewhere between 38 and 129 km, a relatively wide
 1822 range of values. On the other hand, the two-size model has a smaller variance around
 1823 the AC6 $\bar{F}(s)$, which is expected with the addition of two more free parameters. The
 1824 two size model is interpreted as 98% of microbursts diameters are between 12 and 47
 1825 km and larger microbursts are very uncommon.

1826 A variety of continuous $p(d)$ such as the Maxwellian, Weibull and log-normal
 1827 were also tested. While the continuous microburst PDFs are more realistic, there is

no clear choice of which microburst PDF nature prefers. The one and two-size model are simple to interpret, and the two-size model qualitatively fits the observations the best out of all $p(d)$ tested. Surely nature does not only have two discrete microburst sizes. Rather, the current evidence and reasoning supports a bimodal and continuous PDF hypothesis. Due to lack of prior observations and theoretical predictions, it is difficult to identify and test a more appropriate $p(d)$ hypothesis at this time.

The equatorial microburst $\bar{F}(s)$ estimated in section 4 and Fig. 4.4b in particular shows that the majority of microbursts were observed when the equatorial AC6 separation was less than 200 km. We will now explore how these results compare to prior multi-point measurements of chorus source sizes made near the magnetic equator. The International Sun-Earth Explorers (ISEE 1 and 2) were used by Gurnett et al. (1979) to make one of the first direct chorus source scale measurements. Gurnett et al. (1979) estimated that the wave power correlation scale was on the order of a few hundred km across the background magnetic field. Using the Cluster Wide Band Data measurements Santolik et al. (2003) found the correlation scale of whistler mode chorus waves to be around 100 km near the source region at $L \approx 4$ and midnight MLT sector. Furthermore, Turner et al. (2017) used the four satellites comprising the Magnetospheric Multiscale Mission and found that rising tone whistler mode chorus elements were phase coherent up to 70 km at $L \approx 8$. Lastly, Agapitov et al. (2017, 2011, 2010, 2018) used multiple sets of spacecraft missions with wave measurements near the chorus source region to statistically show that the extent of chorus source region can extend from 600 km in the outer radiation belt to greater than 1,000 km in the outer magnetosphere.

The equatorial microburst size of less than a few hundred km shows that the waves responsible for scattering microburst electrons must have correlated properties on those scales. The wave properties necessary for scattering microburst electrons

1854 e.g. coherence, polarization, wave normal angle, etc. can be identified by studying
 1855 the waves properties that are only observed by multiple equatorial spacecraft at
 1856 small separations. These properties can then aid wave-particle scattering model
 1857 development by constraining the wave properties and scattering modes responsible for
 1858 scattering microburst electrons. In turn, future models could then make predictions
 1859 regarding the distribution of microburst sizes in LEO.

1860

Conclusions

1861 In conclusion, the twin AC6 CubeSats enabled the detailed statistical study
 1862 of microburst sizes from a two point measurement platform. Roughly 60% of
 1863 the > 35 keV microbursts were simultaneously observed while AC6 was separated
 1864 by less than 20 km and the rest were observed up to ≈ 70 km separation.
 1865 Modeling the microburst cumulative distribution function is essential to quantify
 1866 the relationship between the number of microbursts observed as a function of
 1867 separation to a hypothesized microburst size distributions. The AC6 microburst
 1868 data, together with modeling, has hinted at the existence of a bimodal microburst
 1869 size PDF with the majority of microbursts with a diameter smaller than 40 km and
 1870 a rare microburst population with a diameter around 100 km. The bimodal size
 1871 hypothesis may be more comprehensively addressed from LEO spacecraft with more
 1872 simultaneous microburst observations, homogeneous MLT coverage, and differential
 1873 energy channels. Moreover, to disentangle the compounding effect that affects two-
 1874 point microburst measurements, a X-ray imager on a high altitude balloon can observe
 1875 the atmospheric microburst footprint and determine the microburst size, shape, and
 1876 any spatial correlations with little ambiguity.

1877 When mapped to the magnetic equator, most microbursts were observed while
 1878 the mapped AC6 separation was less than 200 km. This correlates well with the sizes

1879 of highly correlated chorus waves and it suggests that the wave properties crucial for
1880 scattering microbursts must be correlated over relatively small regions. By studying
1881 the wave properties that are correlated on a few hundred km scales, the dominant
1882 wave scattering modes may be identified.

1883

Acknowledgments

1884 This work was made possible with the help from the many engineers and
1885 scientists at The Aerospace Corporation who designed, built, and operated AC6. M.
1886 Shumko was supported by NASA Headquarters under the NASA Earth and Space
1887 Science Fellowship Program - Grant 80NSSC18K1204. D.L. Turner is thankful for
1888 support from the Van Allen Probes mission and a NASA grant (Prime award number:
1889 80NSSC19K0280). **Other Aerospace and MSU funding sources...** The AC6 data is
1890 available at <http://rbspgway.jhuapl.edu/ac6> and the IRBEM-Lib version used for this
1891 analysis can be downloaded from <https://sourceforge.net/p/irbem/code/616/tree/>.

1892

CONCLUSIONS AND FUTURE WORK

1893 In this dissertation we have explored the microburst scattering mechanism
1894 directly in Chapter 2 and indirectly in Chapters 3 and 4. In Chapter 2 we
1895 used numerous particle and wave instruments on the Van Allen Probes and found
1896 signatures of microbursts with the Magnetic Electron Ion Spectrometer. To these
1897 observations we applied the relativistic theory of wave-particle resonant diffusion
1898 and found that the motion of the microburst electrons was not along single-wave
1899 particle characteristics in momentum phase space, given the spacecraft position and
1900 orientation and most probable wave and plasma parameters. This result at first
1901 appears to contradict the belief that many members of the community hold, that
1902 microburst precipitation is due to a diffusive process. In reality both are probably
1903 valid on different time scales. Individual microbursts are probably not scattered
1904 diffusively, but the combined contribution of an ensemble of microbursts will have
1905 properties that are well modeled as a diffusion process.

1906 The microburst sizes estimated in prior literature as well as Chapters 3 and
1907 4 show that there is a large variability in microburst sizes although microbursts
1908 are relatively small. The study in Ch. 3 gave us a glimpse into the dynamics
1909 of a rarely observed bouncing packet microburst from a dual point measurement
1910 platform. This study has shed light on the lower bound latitudinal and longitudinal
1911 sizes of that microburst, and it was found to be larger than microburst sizes reported
1912 in recent literature, and somewhat smaller than the microburst sizes observed with
1913 high altitude balloons in the mid 1960s. Although this is probably an apples to
1914 oranges comparison because the microburst shape is still unknown and FIREBIRD
1915 was separated in latitude while balloons were separated mostly in longitude.

1916 The AC6 microburst study in Ch. 4 showed that in LEO, 60% of the 662

1917 microbursts were observed while the AC6 separation was less than a few tens of
 1918 km while a minority of microbursts were observed up to ≈ 100 km separation.
 1919 These conclusions agree with prior literature from high altitude balloons and LEO
 1920 spacecraft, although as mentioned before the microburst shape makes comparisons
 1921 somewhat ambiguous. What shape does a microburst have then? A circular
 1922 microburst is easy to interpret and model due to its symmetry, but nature is not
 1923 likely to be so perfect. For example, a circular microburst near the scattering region
 1924 will be deformed into an ellipse when it gets to LEO by the changing topology of
 1925 Earth's magnetic field lines. Microbursts may also have an exotic shape, but this can
 1926 not be further investigated without direct observations of the microburst footprint.
 1927 One feasible solutions exists: a X-ray imager on a high altitude balloon which will be
 1928 discussed in the next section.

1929

Future Work

1930 An extension of the case study in Chapter 2 will be a statistical study using the
 1931 Van Allen Probes. Other microburst-like events have already been identified by eye.
 1932 These other events were also simultaneously observed with enhanced wave activity,
 1933 hence they may be related and a further investigation is warranted. A microburst
 1934 detection scheme similar to the one used in Chapter 4 can be easily implemented to
 1935 automatically identify other microbursts for further study. A few compelling questions
 1936 that can be addressed with this study are: what is the typical pitch angle extent of
 1937 microbursts? Do these microbursts have a similar MLT distribution to microbursts
 1938 observed in LEO? What fraction of microbursts were observed during enhanced wave
 1939 activity? What wave modes and properties are observed during these events? And
 1940 lastly, what fraction of microbursts can be modeled with a diffusive process?

1941 Another study related to the electron bounce period analysis done in Ch. 3 can

1942 be used to verify magnetic field models and in particular the length of magnetic field
 1943 lines. Current magnetospheric magnetic field models assume that Earth's magnetic
 1944 field is relatively static e.g. the International Geomagnetic Reference Field, and
 1945 superpose that field with a highly dynamic field model who's dynamics are driven by
 1946 the plasma environment in the magnetosphere and the solar wind. The difficulty lies
 1947 in accurately modeling this dynamic field, and verifying these models is somewhat
 1948 difficult. One verification technique involves identifying bouncing packet microbursts
 1949 observed by SAMPEX and FIREBIRD, and then estimate the electron bounce period.
 1950 Then a similar analysis to the one in Ch. 3 can be applied to quantify model accuracy
 1951 for a family of magnetospheric models via the length of the magnetic field line between
 1952 the bounce points. Identifying the bouncing packet microbursts is not easy, but may
 1953 be possible with an auto-correlation or machine learning approaches e.g. a neural
 1954 network.

1955 The last project described here that can be done with existing data is to test
 1956 the hypothesis that curtains, that were briefly described in Ch. 4, are the remnants
 1957 of microbursts in the drift loss cone. One way to test this hypothesis is to look for
 1958 the occurrence rates of curtains eastward and westward of the SAA. If curtains are
 1959 electrons in the drift loss cone then the SAA will remove curtains as they drift to the
 1960 east. Thus under the proposed hypothesis the number of curtains should be greater
 1961 just to the west of the SAA than to the east of the SAA. An alternative approach
 1962 to test this hypothesis is to estimate how the flux in each curtain changes between
 1963 the two AC6 units. If curtains are drifting and have a falling energy spectra, then
 1964 the larger number of slower-drifting electrons will appear as an enhancement in the
 1965 curtain flux for the trailing spacecraft. If such a trend is apparent then curtains must
 1966 be drifting, otherwise they may be actively scattered in the same location. Then one
 1967 idea to entertain is the relation of curtains to precipitation bands reported in prior

1968 literature.

1969 Another approach to determine if microburst scattering is a diffusive or a non-
 1970 linear process can be done in LEO where the transport of microburst electrons inside
 1971 the loss cone can be more easily observed. In contrast to particle measurements
 1972 made near the magnetic equator where the local loss cone is only a few degrees, the
 1973 loss cone in LEO is $\approx 60^\circ$ which is much easier to resolve with an instrument with
 1974 multiple look directions. With this measurement, different scattering mechanisms
 1975 can be discriminated. If the scattering process is diffusive, then the microburst flux
 1976 will be monotonically decreasing (or flat) deeper into the loss cone. A non-linear
 1977 scattering process, on the other hand, will have a more complex pitch angle vs flux
 1978 profile e.g. a relative maximum at 0° , followed by decreasing flux towards the loss
 1979 cone boundary. One mission that plans to make this measurement is The Relativistic
 1980 Electron Atmospheric Loss (REAL) CubeSat. This CubeSat, planned to launch in
 1981 2021, will sample the inside and outside of the loss cone with a solid state detector
 1982 with a five look direction collimator.

1983 Lastly, as previously mentioned the microburst shape is an unknown parameter
 1984 that adds ambiguity when comparing the results from the AC6 study in Ch. 4 and
 1985 prior literature from balloons. Imaging microburst precipitation is one of the most
 1986 feasible ways to see the microburst shape. This imaging is possible because when
 1987 microburst electrons impact the atmosphere, they scatter with Earth's atmosphere
 1988 and generate bremsstrahlung X-rays. These X-rays have a relatively long mean
 1989 free path above the Pforzheim maximum above which a balloon-borne imager will
 1990 predominately observe primary X-rays emitted directly from the microburst electrons.
 1991 This idea is the basis for the upcoming Balloon Observations Of Microburst Scales
 1992 (BOOMS) mission. The idea of BOOMS is to fly a set of X-ray pinhole imagers
 1993 containing a scintillator crystal (to convert from X-rays to visible light) and a grid

1994 of photomultiplier tubes (PMT) underneath to record the distribution of light. With
1995 triangulation techniques, this distribution of light across the grid of PMTs together
1996 with instrument modeling can be used to convert between the PMT signal and the
1997 angular position for each observed X-ray. When exposed for a longer duration, a
1998 probabilistic image can then be constructed of the microburst X-ray source. Then
1999 the shape, and any spatial correlations e.g., a microburst train is moving north to
2000 south, can also be observed.

- 2002 Abel, B. and Thorne, R. M. (1998). Electron scattering loss in earth's inner
2003 magnetosphere: 1. dominant physical processes. *Journal of Geophysical Research: Space Physics*, 103(A2):2385–2396.
- 2005 Agapitov, O., Blum, L. W., Mozer, F. S., Bonnell, J. W., and Wygant, J. (2017).
2006 Chorus whistler wave source scales as determined from multipoint van allen probe
2007 measurements. *Geophysical Research Letters*, pages n/a–n/a. 2017GL072701.
- 2008 Agapitov, O., Krasnoselskikh, V., Dudok de Wit, T., Khotyaintsev, Y., Pickett,
2009 J. S., Santolik, O., and Rolland, G. (2011). Multispacecraft observations of chorus
2010 emissions as a tool for the plasma density fluctuations' remote sensing. *Journal of Geophysical Research: Space Physics*, 116(A9):n/a–n/a. A09222.
- 2012 Agapitov, O., Krasnoselskikh, V., Zaliznyak, Y., Angelopoulos, V., Le Contel, O.,
2013 and Rolland, G. (2010). Chorus source region localization in the earth's outer
2014 magnetosphere using themis measurements. *Annales Geophysicae*, 28(6):1377–
2015 1386.
- 2016 Agapitov, O., Mourenas, D., Artemyev, A., Mozer, F., Bonnell, J., Angelopoulos, V.,
2017 Shastun, V., and Krasnoselskikh, V. (2018). Spatial extent and temporal correlation
2018 of chorus and hiss: Statistical results from multipoint themis observations. *Journal of Geophysical Research: Space Physics*, 123(10):8317–8330.
- 2020 Anderson, B., Shekhar, S., Millan, R., Crew, A., Spence, H., Klumpar, D., Blake, J.,
2021 O'Brien, T., and Turner, D. (2017). Spatial scale and duration of one microburst
2022 region on 13 August 2015. *Journal of Geophysical Research: Space Physics*.
- 2023 Anderson, K. A. and Milton, D. W. (1964). Balloon observations of X rays in the
2024 auroral zone: 3. High time resolution studies. *Journal of Geophysical Research*,
2025 69(21):4457–4479.
- 2026 Barcus, J., Brown, R., and Rosenberg, T. (1966). Spatial and temporal character of
2027 fast variations in auroral-zone x rays. *Journal of Geophysical Research*, 71(1):125–
2028 141.
- 2029 Baumjohann, W. and Treumann, R. A. (1997). *Basic space plasma physics*. World
2030 Scientific.
- 2031 Blake, J., Carranza, P., Claudepierre, S., Clemons, J., Crain, W., Dotan, Y.,
2032 Fennell, J., Fuentes, F., Galvan, R., George, J., et al. (2013). The magnetic electron
2033 ion spectrometer (MagEIS) instruments aboard the radiation belt storm probes
2034 (RBSP) spacecraft. *Space Science Reviews*, 179(1-4):383–421.

- 2035 Blake, J.,Looper, M., Baker, D., Nakamura, R., Klecker, B., and Hovestadt, D.
 2036 (1996). New high temporal and spatial resolution measurements by sampex of the
 2037 precipitation of relativistic electrons. *Advances in Space Research*, 18(8):171 – 186.
- 2038 Blake, J. B. and O'Brien, T. P. (2016). Observations of small-scale latitudinal
 2039 structure in energetic electron precipitation. *Journal of Geophysical Research: Space Physics*, 121(4):3031–3035. 2015JA021815.
- 2041 Blum, L., Li, X., and Denton, M. (2015). Rapid MeV electron precipitation as
 2042 observed by SAMPEX/HILT during high-speed stream-driven storms. *Journal of Geophysical Research: Space Physics*, 120(5):3783–3794. 2014JA020633.
- 2044 Bortnik, J., Thorne, R., and Inan, U. S. (2008). Nonlinear interaction of energetic
 2045 electrons with large amplitude chorus. *Geophysical Research Letters*, 35(21).
- 2046 Boscher, D., Bourdarie, S., O'Brien, P., Guild, T., and Shumko, M. (2012). Irbem-lib
 2047 library.
- 2048 Breneman, A., Crew, A., Sample, J., Klumpar, D., Johnson, A., Agapitov, O.,
 2049 Shumko, M., Turner, D., Santolik, O., Wygant, J., et al. (2017). Observations
 2050 directly linking relativistic electron microbursts to whistler mode chorus: Van allen
 2051 probes and FIREBIRD II. *Geophysical Research Letters*.
- 2052 Breneman, A. W., Halford, A., Millan, R., McCarthy, M., Fennell, J., Sample, J.,
 2053 Woodger, L., Hospodarsky, G., Wygant, J. R., Cattell, C. A., et al. (2015). Global-
 2054 scale coherence modulation of radiation-belt electron loss from plasmaspheric hiss.
 2055 *Nature*, 523(7559):193.
- 2056 Brown, R., Barcus, J., and Parsons, N. (1965). Balloon observations of auroral zone
 2057 x rays in conjugate regions. 2. microbursts and pulsations. *Journal of Geophysical
 2058 Research (U.S.)*.
- 2059 Capannolo, L., Li, W., Ma, Q., Shen, X.-C., Zhang, X.-J., Redmon, R., Rodriguez,
 2060 J., Engebretson, M., Kletzing, C., Kurth, W., et al. (2019). Energetic electron
 2061 precipitation: multi-event analysis of its spatial extent during emic wave activity.
 2062 *Journal of Geophysical Research: Space Physics*.
- 2063 Claudepierre, S., O'Brien, T., Looper, M., Blake, J., Fennell, J., Roeder, J.,
 2064 Clemons, J., Mazur, J., Turner, D., Reeves, G., et al. (2019). A revised look
 2065 at relativistic electrons in the earth's inner radiation zone and slot region. *Journal
 2066 of Geophysical Research: Space Physics*, 124(2):934–951.
- 2067 Comess, M., Smith, D., Selesnick, R., Millan, R., and Sample, J. (2013). Duskside
 2068 relativistic electron precipitation as measured by sampex: A statistical survey.
 2069 *Journal of Geophysical Research: Space Physics*, 118(8):5050–5058.

- 2070 Crew, A. B., Spence, H. E., Blake, J. B., Klumpar, D. M., Larsen, B. A., O'Brien,
 2071 T. P., Driscoll, S., Handley, M., Legere, J., Longworth, S., Mashburn, K.,
 2072 Mosleh, E., Ryhajlo, N., Smith, S., Springer, L., and Widholm, M. (2016). First
 2073 multipoint in situ observations of electron microbursts: Initial results from the
 2074 NSF FIREBIRD II mission. *Journal of Geophysical Research: Space Physics*,
 2075 121(6):5272–5283. 2016JA022485.
- 2076 Datta, S., Skoug, R., McCarthy, M., and Parks, G. (1997). Modeling of microburst
 2077 electron precipitation using pitch angle diffusion theory. *Journal of Geophysical
 2078 Research: Space Physics*, 102(A8):17325–17333.
- 2079 Dietrich, S., Rodger, C. J., Clilverd, M. A., Bortnik, J., and Raita, T. (2010).
 2080 Relativistic microburst storm characteristics: Combined satellite and ground-based
 2081 observations. *Journal of Geophysical Research: Space Physics*, 115(A12).
- 2082 Douma, E., Rodger, C., Blum, L., O'Brien, T., Clilverd, M., and Blake, J. (2019).
 2083 Characteristics of relativistic microburst intensity from sampex observations.
 2084 *Journal of Geophysical Research: Space Physics*.
- 2085 Douma, E., Rodger, C. J., Blum, L. W., and Clilverd, M. A. (2017). Occurrence
 2086 characteristics of relativistic electron microbursts from SAMPEX observations.
 2087 *Journal of Geophysical Research: Space Physics*, 122(8):8096–8107. 2017JA024067.
- 2088 Eastwood, J., Hietala, H., Toth, G., Phan, T., and Fujimoto, M. (2015). What
 2089 controls the structure and dynamics of earths magnetosphere? *Space Science
 2090 Reviews*, 188(1-4):251–286.
- 2091 Fang, X., Randall, C. E., Lummerzheim, D., Wang, W., Lu, G., Solomon, S. C., and
 2092 Frahm, R. A. (2010). Parameterization of monoenergetic electron impact ionization.
 2093 *Geophysical Research Letters*, 37(22).
- 2094 Funsten, H., Skoug, R., Guthrie, A., MacDonald, E., Baldonado, J., Harper, R.,
 2095 Henderson, K., Kihara, K., Lake, J., Larsen, B., et al. (2013). Helium, Oxygen,
 2096 Proton, and Electron (HOPE) mass spectrometer for the radiation belt storm
 2097 probes mission. *Space Science Reviews*, 179(1-4):423–484.
- 2098 Greeley, A., Kanekal, S., Baker, D., Klecker, B., and Schiller, Q. (2019). Quantifying
 2099 the contribution of microbursts to global electron loss in the radiation belts. *Journal
 2100 of Geophysical Research: Space Physics*.
- 2101 Gurnett, D., Anderson, R., Scarf, F., Fredricks, R., and Smith, E. (1979). Initial
 2102 results from the iese-1 and-2 plasma wave investigation. *Space Science Reviews*,
 2103 23(1):103–122.
- 2104 Hastings, W. K. (1970). Monte carlo sampling methods using markov chains and
 2105 their applications.

- 2106 Hendry, A. T., Rodger, C. J., and Clilverd, M. A. (2017). Evidence of sub-mev
 2107 emic-driven electron precipitation. *Geophysical Research Letters*, 44(3):1210–1218.
- 2108 Hoots, F. R. and Roehrich, R. L. (1980). Models for propagation of norad element
 2109 sets. Technical Report 3, Spacetrack.
- 2110 Horne, R., Glauert, S., Meredith, N., Boscher, D., Maget, V., Heynderickx, D., and
 2111 Pitchford, D. (2013). Space weather impacts on satellites and forecasting the earth's
 2112 electron radiation belts with spacecast. *Space Weather*, 11(4):169–186.
- 2113 Horne, R., Thorne, R., Meredith, N., and Anderson, R. (2003). Diffuse auroral
 2114 electron scattering by electron cyclotron harmonic and whistler mode waves during
 2115 an isolated substorm. *Journal of Geophysical Research: Space Physics*, 108(A7).
- 2116 Horne, R. B. and Thorne, R. M. (2003). Relativistic electron acceleration and
 2117 precipitation during resonant interactions with whistler-mode chorus. *Geophysical
 2118 Research Letters*, 30(10). 1527.
- 2119 Horne, R. B., Thorne, R. M., Shprits, Y. Y., Meredith, N. P., Glauert, S. A., Smith,
 2120 A. J., Kanekal, S. G., Baker, D. N., Engebretson, M. J., Posch, J. L., et al.
 2121 (2005). Wave acceleration of electrons in the van allen radiation belts. *Nature*,
 2122 437(7056):227.
- 2123 Joy, S., Kivelson, M., Walker, R., Khurana, K., Russell, C., and Ogino, T. (2002).
 2124 Probabilistic models of the jovian magnetopause and bow shock locations. *Journal
 2125 of Geophysical Research: Space Physics*, 107(A10):SMP–17.
- 2126 Kasahara, S., Miyoshi, Y., Yokota, S., Mitani, T., Kasahara, Y., Matsuda, S.,
 2127 Kumamoto, A., Matsuoka, A., Kazama, Y., Frey, H., et al. (2018). Pulsating
 2128 aurora from electron scattering by chorus waves. *Nature*, 554(7692):337.
- 2129 Kletzing, C., Kurth, W., Acuna, M., MacDowall, R., Torbert, R., Averkamp, T.,
 2130 Bodet, D., Bounds, S., Chutter, M., Connerney, J., et al. (2013). The electric and
 2131 magnetic field instrument suite and integrated science (EMFISIS) on RBSP. *Space
 2132 Science Reviews*, 179(1-4):127–181.
- 2133 Klumpar, D., Springer, L., Mosleh, E., Mashburn, K., Berardinelli, S., Gunderson,
 2134 A., Handly, M., Ryhajlo, N., Spence, H., Smith, S., Legere, J., Widholm, M.,
 2135 Longworth, S., Crew, A., Larsen, B., Blake, J., and Walmsley, N. (2015). Flight
 2136 system technologies enabling the twin-cubesat firebird-ii scientific mission.
- 2137 Lee, J. J., Parks, G. K., Lee, E., Tsurutani, B. T., Hwang, J., Cho, K. S., Kim, K.-H.,
 2138 Park, Y. D., Min, K. W., and McCarthy, M. P. (2012). Anisotropic pitch angle
 2139 distribution of 100 keV microburst electrons in the loss cone: measurements from
 2140 STSAT-1. *Annales Geophysicae*, 30(11):1567–1573.

- 2141 Lee, J.-J., Parks, G. K., Min, K. W., Kim, H. J., Park, J., Hwang, J., McCarthy,
 2142 M. P., Lee, E., Ryu, K. S., Lim, J. T., Sim, E. S., Lee, H. W., Kang, K. I., and
 2143 Park, H. Y. (2005). Energy spectra of 170–360 keV electron microbursts measured
 2144 by the korean STSAT-1. *Geophysical Research Letters*, 32(13). L13106.
- 2145 Li, W., Thorne, R., Angelopoulos, V., Bonnell, J., McFadden, J., Carlson, C.,
 2146 LeContel, O., Roux, A., Glassmeier, K., and Auster, H. (2009a). Evaluation of
 2147 whistler-mode chorus intensification on the nightside during an injection event
 2148 observed on the THEMIS spacecraft. *Journal of Geophysical Research: Space
 2149 Physics*, 114(A1).
- 2150 Li, W., Thorne, R., Bortnik, J., Tao, X., and Angelopoulos, V. (2012). Characteristics
 2151 of hiss-like and discrete whistler-mode emissions. *Geophysical Research Letters*,
 2152 39(18).
- 2153 Li, W., Thorne, R. M., Angelopoulos, V., Bortnik, J., Cully, C. M., Ni, B., LeContel,
 2154 O., Roux, A., Auster, U., and Magnes, W. (2009b). Global distribution of whistler-
 2155 mode chorus waves observed on the THEMIS spacecraft. *Geophysical Research
 2156 Letters*, 36(9). L09104.
- 2157 Li, X., Selesnick, R., Schiller, Q., Zhang, K., Zhao, H., Baker, D. N., and Temerin,
 2158 M. A. (2017). Measurement of electrons from albedo neutron decay and neutron
 2159 density in near-earth space. *Nature*, 552(7685):382.
- 2160 Lorentzen, K. R., Blake, J. B., Inan, U. S., and Bortnik, J. (2001a). Observations
 2161 of relativistic electron microbursts in association with VLF chorus. *Journal of
 2162 Geophysical Research: Space Physics*, 106(A4):6017–6027.
- 2163 Lorentzen, K. R., Looper, M. D., and Blake, J. B. (2001b). Relativistic electron
 2164 microbursts during the GEM storms. *Geophysical Research Letters*, 28(13):2573–
 2165 2576.
- 2166 Lyons, L. R. and Thorne, R. M. (1973). Equilibrium structure of radiation belt
 2167 electrons. *Journal of Geophysical Research*, 78(13):2142–2149.
- 2168 Manweiler, J. W. and Zwiener, H. M. (2018). Science Operations Center (SOC)
 2169 RBSPICE Science Data Handbook Revision: e. Technical report, Fundamental
 2170 Technologies, LLC.
- 2171 Mauk, B., Fox, N. J., Kanekal, S., Kessel, R., Sibeck, D., and Ukhorskiy, A. (2013).
 2172 Science objectives and rationale for the radiation belt storm probes mission. *Space
 2173 Science Reviews*, 179(1-4):3–27.
- 2174 Meredith, N., Horne, R., Summers, D., Thorne, R., Iles, R., Heynderickx, D., and
 2175 Anderson, R. (2002). Evidence for acceleration of outer zone electrons to relativistic
 2176 energies by whistler mode chorus. In *Annales Geophysicae*, volume 20, pages 967–
 2177 979.

- 2178 Metropolis, N., Rosenbluth, A. W., Rosenbluth, M. N., Teller, A. H., and Teller, E.
 2179 (1953). Equation of state calculations by fast computing machines. *The journal of
 2180 chemical physics*, 21(6):1087–1092.
- 2181 Millan, R. and Thorne, R. (2007). Review of radiation belt relativistic electron losses.
 2182 *Journal of Atmospheric and Solar-Terrestrial Physics*, 69(3):362 – 377.
- 2183 Millan, R. M., Lin, R., Smith, D., Lorentzen, K., and McCarthy, M. (2002). X-
 2184 ray observations of mev electron precipitation with a balloon-borne germanium
 2185 spectrometer. *Geophysical research letters*, 29(24).
- 2186 Mitchell, D., Lanzerotti, L., Kim, C., Stokes, M., Ho, G., Cooper, S., Ukhorskiy, A.,
 2187 Manweiler, J., Jaskulek, S., Haggerty, D., et al. (2013). Radiation belt storm probes
 2188 ion composition experiment (RBSPICE). *Space Science Reviews*, 179(1-4):263–308.
- 2189 Mozer, F. S., Agapitov, O. V., Blake, J. B., and Vasko, I. Y. (2018). Simultaneous
 2190 observations of lower band chorus emissions at the equator and microburst
 2191 precipitating electrons in the ionosphere. *Geophysical Research Letters*.
- 2192 Nakamura, R., Baker, D. N., Blake, J. B., Kanekal, S., Klecker, B., and Hovestadt,
 2193 D. (1995). Relativistic electron precipitation enhancements near the outer edge of
 2194 the radiation belt. *Geophysical Research Letters*, 22(9):1129–1132.
- 2195 Nakamura, R., Isowa, M., Kamide, Y., Baker, D., Blake, J., and Looper, M. (2000).
 2196 Observations of relativistic electron microbursts in association with VLF chorus.
 2197 *J. Geophys. Res*, 105:15875–15885.
- 2198 Nishimura, Y., Bortnik, J., Li, W., Thorne, R., Chen, L., Lyons, L., Angelopoulos,
 2199 V., Mende, S., Bonnell, J., Le Contel, O., et al. (2011). Multievent study of the
 2200 correlation between pulsating aurora and whistler mode chorus emissions. *Journal
 2201 of Geophysical Research: Space Physics*, 116(A11).
- 2202 O'Brien, T., Claudepierre, S., Blake, J., Fennell, J. F., Clemons, J., Roeder, J.,
 2203 Spence, H. E., Reeves, G., and Baker, D. (2014). An empirically observed pitch-
 2204 angle diffusion eigenmode in the earth's electron belt near $\lambda^* = 5.0$. *Geophysical
 2205 Research Letters*, 41(2):251–258.
- 2206 O'Brien, T., Claudepierre, S., Guild, T., Fennell, J., Turner, D., Blake, J., Clemons,
 2207 J., and Roeder, J. (2016a). Inner zone and slot electron radial diffusion revisited.
 2208 *Geophysical Research Letters*, 43(14):7301–7310.
- 2209 O'Brien, T. and Moldwin, M. (2003). Empirical plasmapause models from magnetic
 2210 indices. *Geophysical Research Letters*, 30(4).
- 2211 O'Brien, T. P., Blake, J. B., and W., G. J. (2016b). Aerocube-6 dosimeter data
 2212 readme. Technical Report TOR-2016-01155, The Aerospace Corporation.

- 2213 O'Brien, T. P., Looper, M. D., and Blake, J. B. (2004). Quantification of relativistic
 2214 electron microburst losses during the GEM storms. *Geophysical Research Letters*,
 2215 31(4). L04802.
- 2216 O'Brien, T. P., Lorentzen, K. R., Mann, I. R., Meredith, N. P., Blake, J. B., Fennell,
 2217 J. F., Looper, M. D., Milling, D. K., and Anderson, R. R. (2003). Energization of
 2218 relativistic electrons in the presence of ULF power and MeV microbursts: Evidence
 2219 for dual ULF and VLF acceleration. *Journal of Geophysical Research: Space*
 2220 *Physics*, 108(A8).
- 2221 Olson, W. P. and Pfitzer, K. A. (1982). A dynamic model of the magnetospheric
 2222 magnetic and electric fields for july 29, 1977. *Journal of Geophysical Research: Space*
 2223 *Physics*, 87(A8):5943–5948.
- 2224 Ozaki, M., Miyoshi, Y., Shiokawa, K., Hosokawa, K., Oyama, S.-i., Kataoka, R.,
 2225 Ebihara, Y., Ogawa, Y., Kasahara, Y., Yagitani, S., et al. (2019). Visualization of
 2226 rapid electron precipitation via chorus element wave–particle interactions. *Nature*
 2227 *communications*, 10(1):257.
- 2228 Ozaki, M., Yagitani, S., Ishizaka, K., Shiokawa, K., Miyoshi, Y., Kadokura, A.,
 2229 Yamagishi, H., Kataoka, R., Ieda, A., Ebihara, Y., Sato, N., and Nagano, I. (2012).
 2230 Observed correlation between pulsating aurora and chorus waves at Syowa Station
 2231 in Antarctica: A case study. *Journal of Geophysical Research: Space Physics*,
 2232 117(A8).
- 2233 Parks, G. (2003). *Physics Of Space Plasmas: An Introduction, Second Edition*.
 2234 Westview Press.
- 2235 Parks, G. K. (1967). Spatial characteristics of auroral-zone X-ray microbursts. *Journal*
 2236 *of Geophysical Research*, 72(1):215–226.
- 2237 Reeves, G., Spence, H. E., Henderson, M., Morley, S., Friedel, R., Funsten, H., Baker,
 2238 D., Kanekal, S., Blake, J., Fennell, J., et al. (2013). Electron acceleration in the
 2239 heart of the van allen radiation belts. *Science*, 341(6149):991–994.
- 2240 Reeves, G. D., McAdams, K. L., Friedel, R. H. W., and O'Brien, T. P. (2003). Ac-
 2241 celeration and loss of relativistic electrons during geomagnetic storms. *Geophysical*
 2242 *Research Letters*, 30(10):n/a–n/a. 1529.
- 2243 Sambridge, M., Gallagher, K., Jackson, A., and Rickwood, P. (2006). Trans-
 2244 dimensional inverse problems, model comparison and the evidence. *Geophysical*
 2245 *Journal International*, 167(2):528–542.
- 2246 Santolik, O., Gurnett, D., Pickett, J., Parrot, M., and Cornilleau-Wehrlin, N. (2003).
 2247 Spatio-temporal structure of storm-time chorus. *Journal of Geophysical Research:*
 2248 *Space Physics*, 108(A7).

- 2249 Santolk, O., Parrot, M., and Lefevre, F. (2003). Singular value decomposition
 2250 methods for wave propagation analysis. *Radio Science*, 38(1):n/a–n/a. 1010.
- 2251 Schulz, M. and Lanzerotti, L. J. (1974). *Particle Diffusion in the Radiation Belts*.
 2252 Springer.
- 2253 Selesnick, R. S., Blake, J. B., and Mewaldt, R. A. (2003). Atmospheric losses of
 2254 radiation belt electrons. *Journal of Geophysical Research: Space Physics*, 108(A12).
 2255 1468.
- 2256 Seppälä, A., Douma, E., Rodger, C., Verronen, P., Clilverd, M. A., and Bortnik, J.
 2257 (2018). Relativistic electron microburst events: Modeling the atmospheric impact.
 2258 *Geophysical Research Letters*, 45(2):1141–1147.
- 2259 Sharma, S. (2017). Markov chain monte carlo methods for bayesian data analysis in
 2260 astronomy. *Annual Review of Astronomy and Astrophysics*, 55:213–259.
- 2261 Shprits, Y. Y., Meredith, N. P., and Thorne, R. M. (2007). Parameterization
 2262 of radiation belt electron loss timescales due to interactions with chorus waves.
 2263 *Geophysical Research Letters*, 34(11):n/a–n/a. L11110.
- 2264 Shprits, Y. Y. and Thorne, R. M. (2004). Time dependent radial diffusion modeling
 2265 of relativistic electrons with realistic loss rates. *Geophysical Research Letters*,
 2266 31(8):n/a–n/a. L08805.
- 2267 Shumko, M., Sample, J., Johnson, A., Blake, B., Crew, A., Spence, H., Klumpar, D.,
 2268 Agapitov, O., and Handley, M. (2018). Microburst scale size derived from multiple
 2269 bounces of a microburst simultaneously observed with the firebird-ii cubesats.
 2270 *Geophysical Research Letters*, 45(17):8811–8818.
- 2271 Spence, H. E., Blake, J. B., Crew, A. B., Driscoll, S., Klumpar, D. M., Larsen,
 2272 B. A., Legere, J., Longworth, S., Mosleh, E., O'Brien, T. P., Smith, S., Springer,
 2273 L., and Widholm, M. (2012). Focusing on size and energy dependence of electron
 2274 microbursts from the van allen radiation belts. *Space Weather*, 10(11).
- 2275 Summers, D., Thorne, R. M., and Xiao, F. (1998). Relativistic theory of wave-particle
 2276 resonant diffusion with application to electron acceleration in the magnetosphere.
 2277 *Journal of Geophysical Research: Space Physics*, 103(A9):20487–20500.
- 2278 Takahashi, K. and Denton, R. E. (2007). Magnetospheric seismology using multi-
 2279 harmonic toroidal waves observed at geosynchronous orbit. *Journal of Geophysical
 2280 Research: Space Physics*, 112(A5).
- 2281 Thorne, R. M. (2010). Radiation belt dynamics: The importance of wave-particle
 2282 interactions. *Geophysical Research Letters*, 37(22). L22107.

- 2283 Thorne, R. M. and Andreoli, L. J. (1981). *Mechanisms for Intense Relativistic
2284 Electron Precipitation*, pages 381–394. Springer Netherlands, Dordrecht.
- 2285 Thorne, R. M., O'Brien, T. P., Shprits, Y. Y., Summers, D., and Horne, R. B. (2005).
2286 Timescale for MeV electron microburst loss during geomagnetic storms. *Journal
2287 of Geophysical Research: Space Physics*, 110(A9). A09202.
- 2288 Trefall, H., Bjordal, J., Ullaland, S., and Stadsnes, J. (1966). On the extension of
2289 auroral-zone x-ray microbursts. *Journal of Atmospheric and Terrestrial Physics*,
2290 28(2):225–233.
- 2291 Tsurutani, B. T. and Lakhina, G. S. (1997). Some basic concepts of wave-particle
2292 interactions in collisionless plasmas. *Reviews of Geophysics*, 35(4):491–501.
- 2293 Tsurutani, B. T., Lakhina, G. S., and Verkhoglyadova, O. P. (2013). Energetic
2294 electron ($\gtrsim 10$ kev) microburst precipitation, $\sim 5\text{--}15$ s x-ray pulsations, chorus,
2295 and wave-particle interactions: A review. *Journal of Geophysical Research: Space
2296 Physics*, 118(5):2296–2312.
- 2297 Tsyganenko, N. (1989). A solution of the chapman-ferraro problem for an ellipsoidal
2298 magnetopause. *Planetary and Space Science*, 37(9):1037 – 1046.
- 2299 Tsyganenko, N. A. and Sitnov, M. I. (2005). Modeling the dynamics of the inner
2300 magnetosphere during strong geomagnetic storms. *Journal of Geophysical Research:
2301 Space Physics*, 110(A3).
- 2302 Turner, D., Lee, J., Claudepierre, S., Fennell, J., Blake, J., Jaynes, A., Leonard,
2303 T., Wilder, F., Ergun, R., Baker, D., et al. (2017). Examining coherency
2304 scales, substructure, and propagation of whistler mode chorus elements with
2305 magnetospheric multiscale (mms). *Journal of Geophysical Research: Space Physics*,
2306 122(11).
- 2307 Ukhorskiy, A. Y., Anderson, B. J., Brandt, P. C., and Tsyganenko, N. A. (2006).
2308 Storm time evolution of the outer radiation belt: Transport and losses. *Journal of
2309 Geophysical Research: Space Physics*, 111(A11):n/a–n/a. A11S03.
- 2310 Van Allen, J. A. (1959). The geomagnetically trapped corpuscular radiation. *Journal
2311 of Geophysical Research*, 64(11):1683–1689.
- 2312 Vernov, S. and Chudakov, A. (1960). Investigation of radiation in outer space. In
2313 *International Cosmic Ray Conference*, volume 3, page 19.
- 2314 Walker, A. D. M. (1993). *Plasma waves in the magnetosphere*, volume 24. Springer
2315 Science & Business Media.

- 2316 Woodger, L., Halford, A., Millan, R., McCarthy, M., Smith, D., Bowers, G., Sample,
2317 J., Anderson, B., and Liang, X. (2015). A summary of the BARREL campaigns:
2318 Technique for studying electron precipitation. *Journal of Geophysical Research:*
2319 *Space Physics*, 120(6):4922–4935.

APPENDIX: APPENDIX A

2321 This appendix contains Figs. A.1 and A.2. Figure A.1 shows evidence that
2322 supports our claim that the “hiss-like” chorus wave observed at 11:17:03 UT with
2323 EMFISIS WFR instrument on RBSP-A was parallel propagating. The polar angle
2324 of the wave vector and the supporting planarity of the magnetic field polarization
2325 shown in Fig. A.1 was calculated using the singular value decomposition (SVD)
2326 method (Santolk et al., 2003).

2327 Figure A.2 supports the claim that RBSPICE-A observed a 10-80% increase in
2328 the count rates at the microburst times and pitch angles. Figure A.2 shows the ratio
2329 of the RBSPICE-A’s EBR count rates during the four microbursts to the quiet time
2330 one spin before, at the same pitch angles.

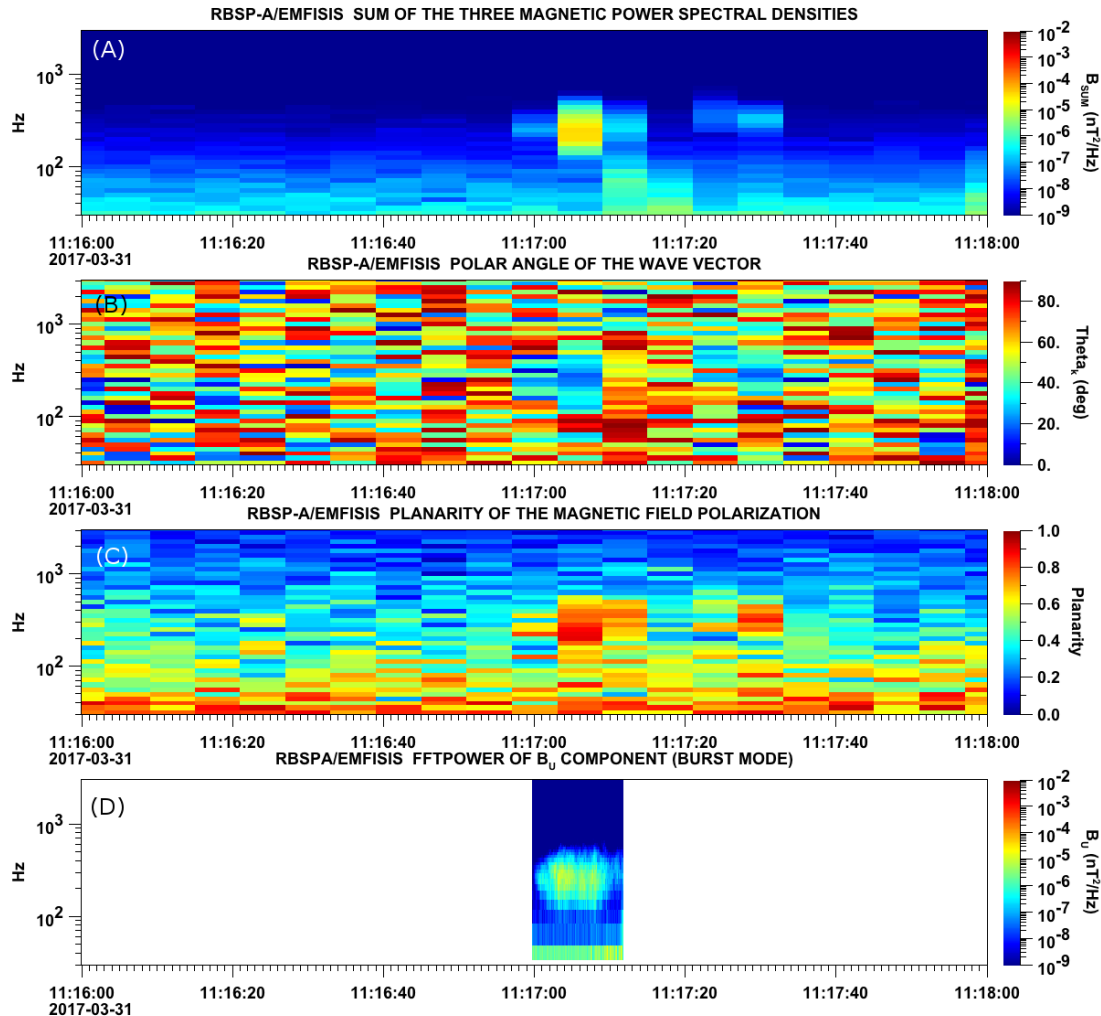


Figure A.1: Panel (A) shows the magnetic power spectral density as a function of frequency and time from the EMFISIS WFR instrument on board RBSP-A. The “hiss-like” wave used for the resonant diffusion analysis was observed starting at 11:17:03 UT. In the same format as panel (A), panel (B) shows the polar angle of the wave vector for this time period. The wave of interest had a normal wave vector, $\theta_k < 30^\circ$. Since the results in panel (B) are valid only for high planarity, panel (C) shows planarity in the same format as panels (A) and (B). The wave of interest was found to have a planarity of > 0.8 . Lastly, panel (D) shows the available burst mode data.

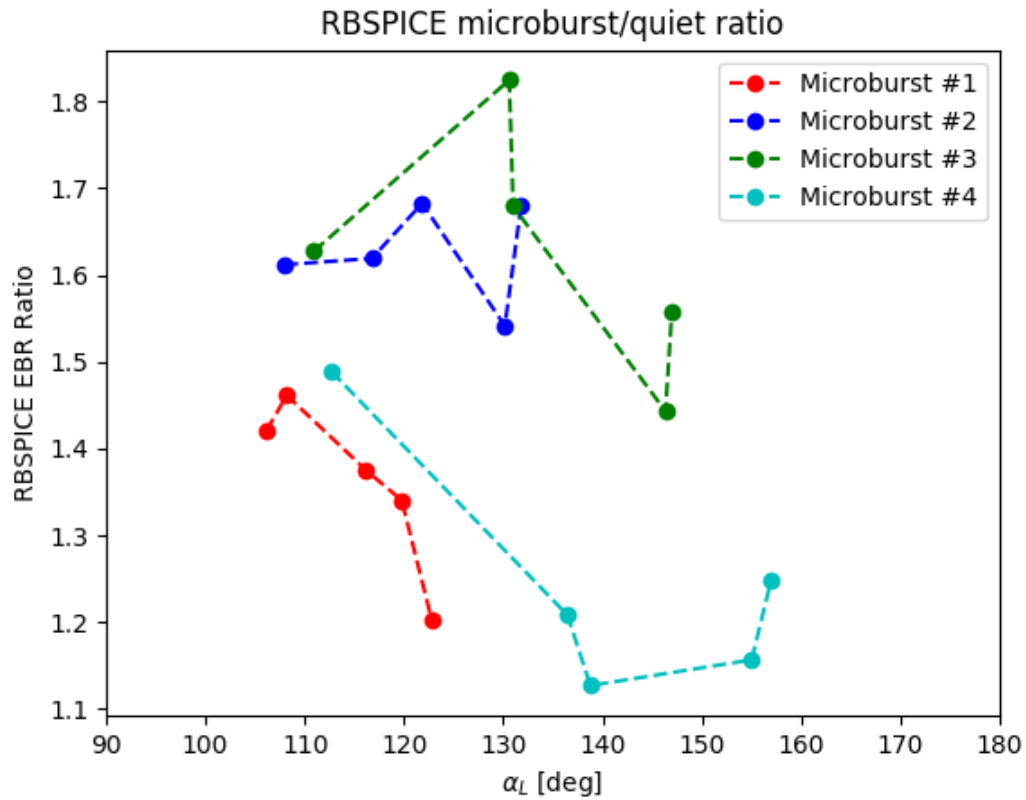


Figure A.2: Ratio of the RBSPICE EBR at microburst times indicated with the black vertical arrows in Fig. 2, to the EBR at the same pitch angles one spin prior (quiet time). The microburst flux was enhanced by 10-80% across $100^\circ < \alpha_L < 160^\circ$ PA, and appear to be peaked closer to $\alpha_L = 90^\circ$.

2331

APPENDIX: APPENDIX B

2332 This appendix describes the method we used to calculate the time difference and
 2333 separation between FU3 and FU4 at 06:12 UT on February 2nd, 2015. We used the
 2334 following method to calculate the clock difference, δt_c and separation, d between FU3
 2335 and FU4 at 06:12 UT on February 2nd, 2015.

2336 The relative clock difference was calculated with a cross-correlation time
 2337 lag analysis on uniquely-identified trains of microbursts that hit both spacecraft
 2338 simultaneously. Four time periods with coincident microbursts were hand-picked on
 2339 February 2nd, 2015 and are shown in Figs. B.1-B.4, panels (a) and (b). The cross-
 2340 correlation time lag analysis was applied to the HiRes time series in panels (a) and
 2341 (b), and the resulting normalized cross-correlation coefficient as a function of time is
 2342 shown in panel (c). To validate the peak lag identified in panel (c), FU3's time series
 2343 was shifted by that lag and is shown in panel (d).

2344 The clock differences from the simultaneous microbursts in Figs. B.1-B.4 were
 2345 linearly fit to account for the relative clock drift (≈ 20 ms/hour at this time), giving
 2346 a value of $\delta t_c = 2.28 \pm 0.12$ s at the time of the microburst analyzed here. This time
 2347 shift was applied to the HiRes data in Fig. 1. A clock difference of $\delta t_c = 2.45^{+0.51}_{-0.98}$ s
 2348 was independently calculated with the FIREBIRD-II telemetry beacon time stamps
 2349 that were downlinked during operational passes.

2350 We calculate the spacecraft separation, by applying same the cross-correlation
 2351 time lag analysis on structures assumed to be spatial and are shown in Figs. B.5
 2352 and B.6. The lag from the peak cross-correlation between these events is a sum of
 2353 the clock difference and time lag due to the spacecraft separation. We interpret the
 2354 time lag due to the spacecraft separation as the time difference between when the
 2355 leading satellite observed a stationary spatial feature, to when the trailing satellite
 2356 observed the same stationary spatial feature. With the method described above, we
 2357 find the spatial time lag to be $\delta t_d = 2.64 \pm 0.12$ s (after we account for the clock
 2358 difference and its uncertainty). To convert from a spatial time lag to a spacecraft
 2359 separation, we calculate the satellite velocity. We calculate the velocity using a Two
 2360 Line Element (TLE), a data format containing the orbit parameters that are used
 2361 for orbit propagation. With the TLE derived spacecraft velocity, $v = 7.57$ km/s, the
 2362 spacecraft separation was $d = 19.9 \pm 0.9$ km.

2363 An independent method to calculate the spacecraft separation was developed.
 2364 The separation was calculated using TLEs. The TLE from February 2nd was
 2365 anomalous and was not used in this analysis. Instead, seven TLEs released up to
 2366 five days after the microburst event were backpropagated, using the SGP-4 algorithm
 2367 (Hoots and Roehrich, 1980) that calculates orbital state vectors with perturbations
 2368 such as Earth's atmosphere, as well as gravitational effects from the moon and sun.
 2369 Then the predicted spacecraft separations at the time of the microburst event were

2370 averaged to derive a separation of $d = 18.4 \pm 1.5$ km. These two methods give
2371 similar separations, which implies that the stationary event assumption used in the
2372 cross-correlation time lag analysis is reasonable.

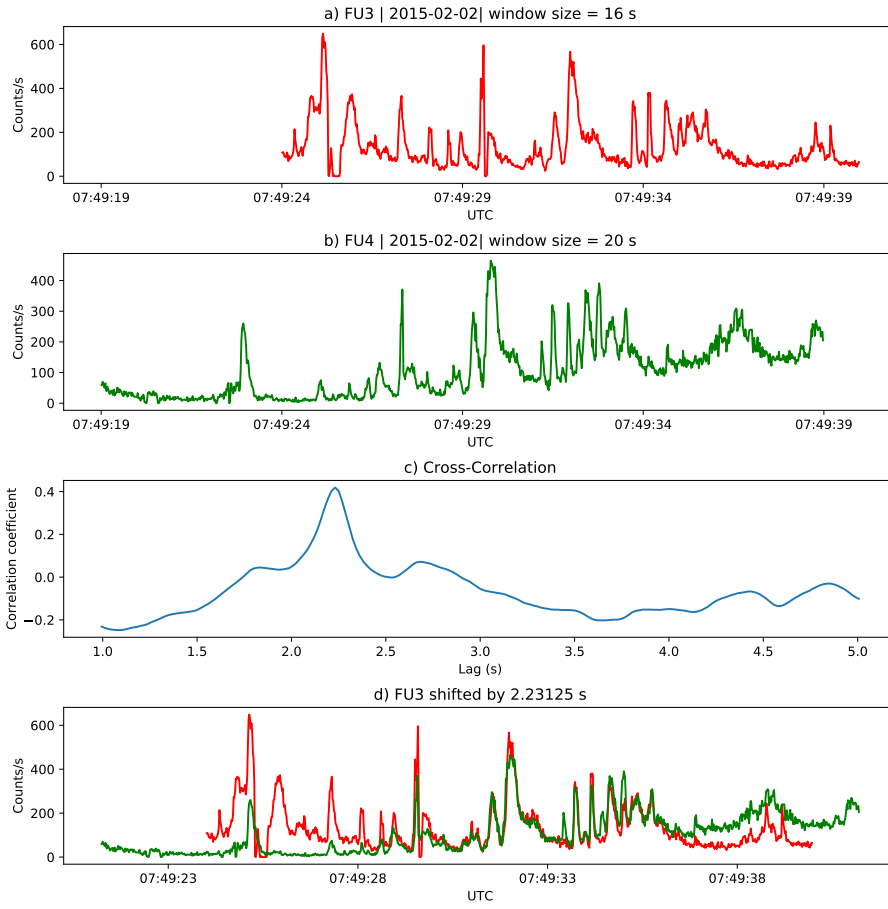


Figure B.1: Cross-correlation time lag analysis applied to a train of microbursts. Panel (a) and (b) show the count rate from the lowest energy channel. Panel (c) shows the cross-correlation coefficient as a function of time lag. Panel (d) shows the shifted timeseries. Clock difference was 2.23 s.

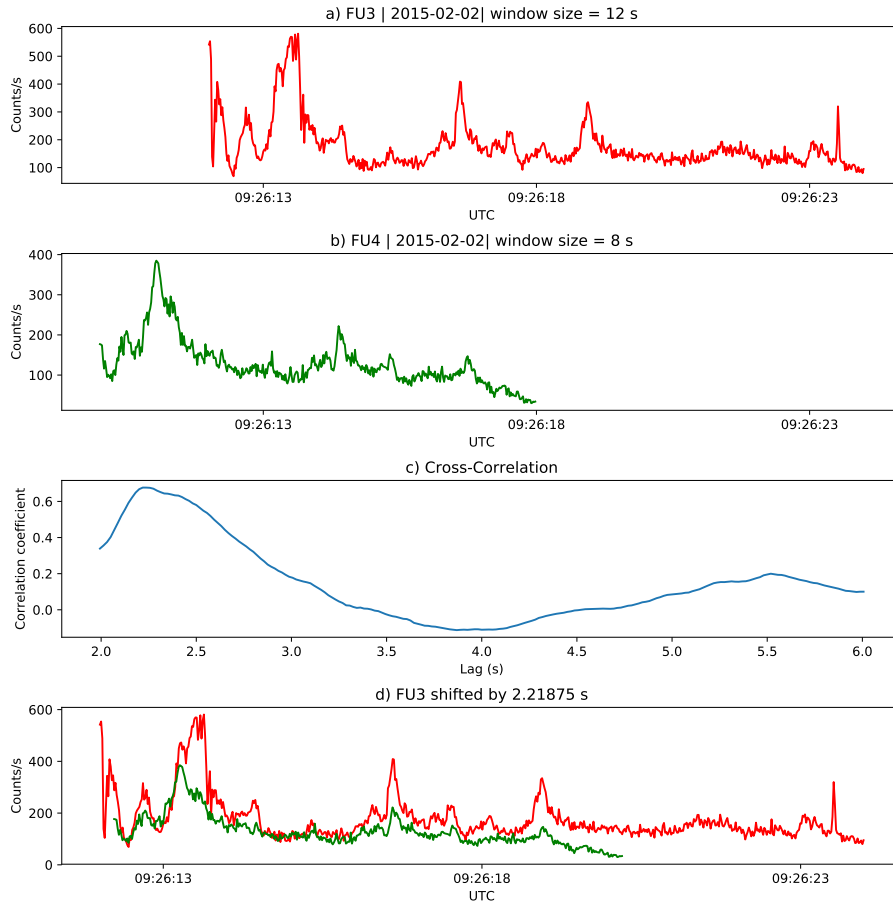


Figure B.2: Same analysis as Fig. B.1 on a different time period. Clock difference was 2.21 s.

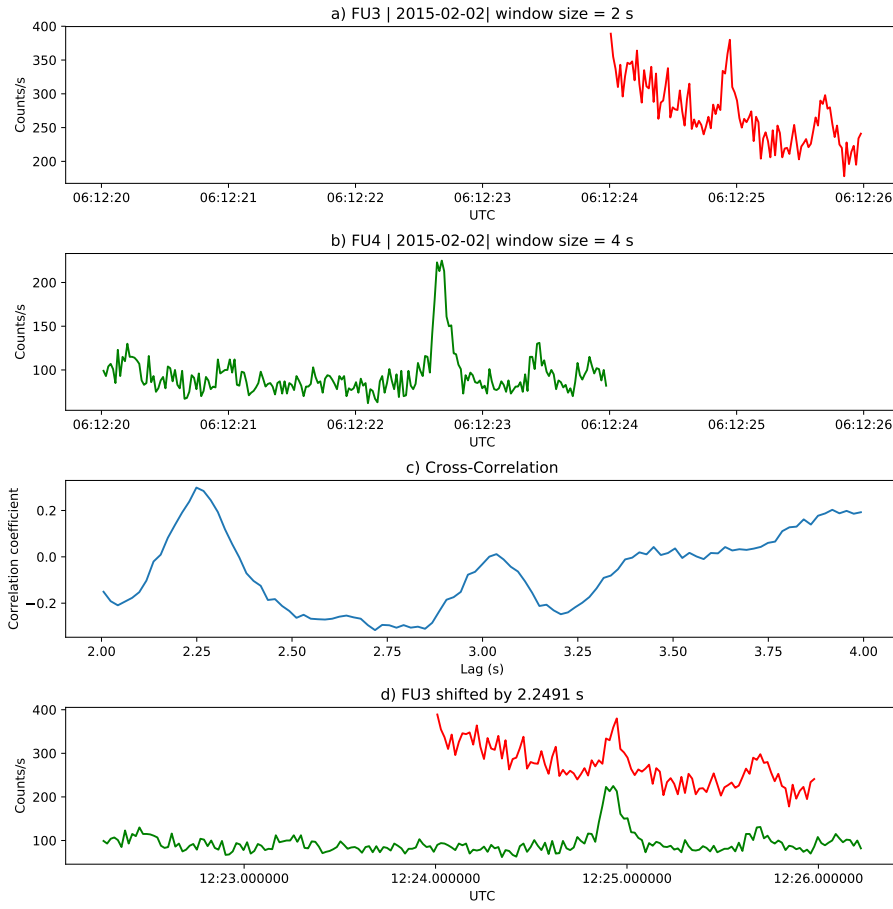


Figure B.3: Same analysis as Fig. B.1 on a different time period. Clock difference was 2.25 s.

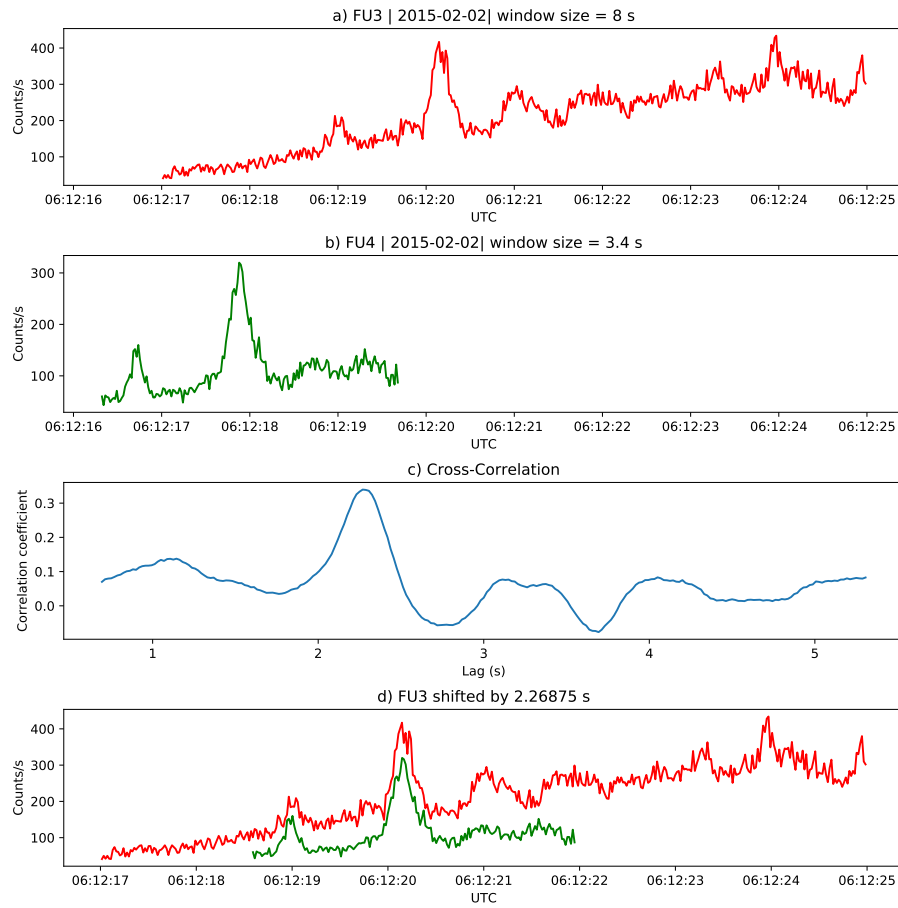


Figure B.4: Same analysis as Fig. B.1 on a different time period. Clock difference was 2.27 s.

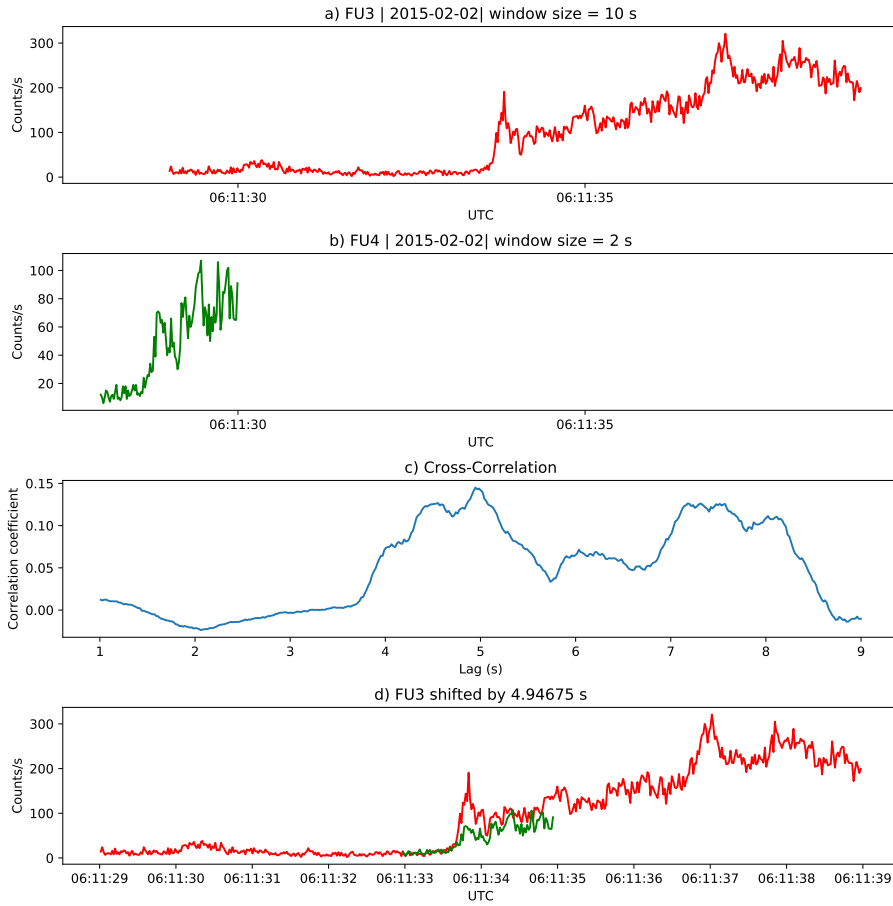


Figure B.5: Same cross-correlation time lag analysis applied to stationary spatial structures. The cross-correlation lag between these events is a sum of the clock difference and time lag due to the spacecraft separation. The lag derived at this time was 4.95 s.

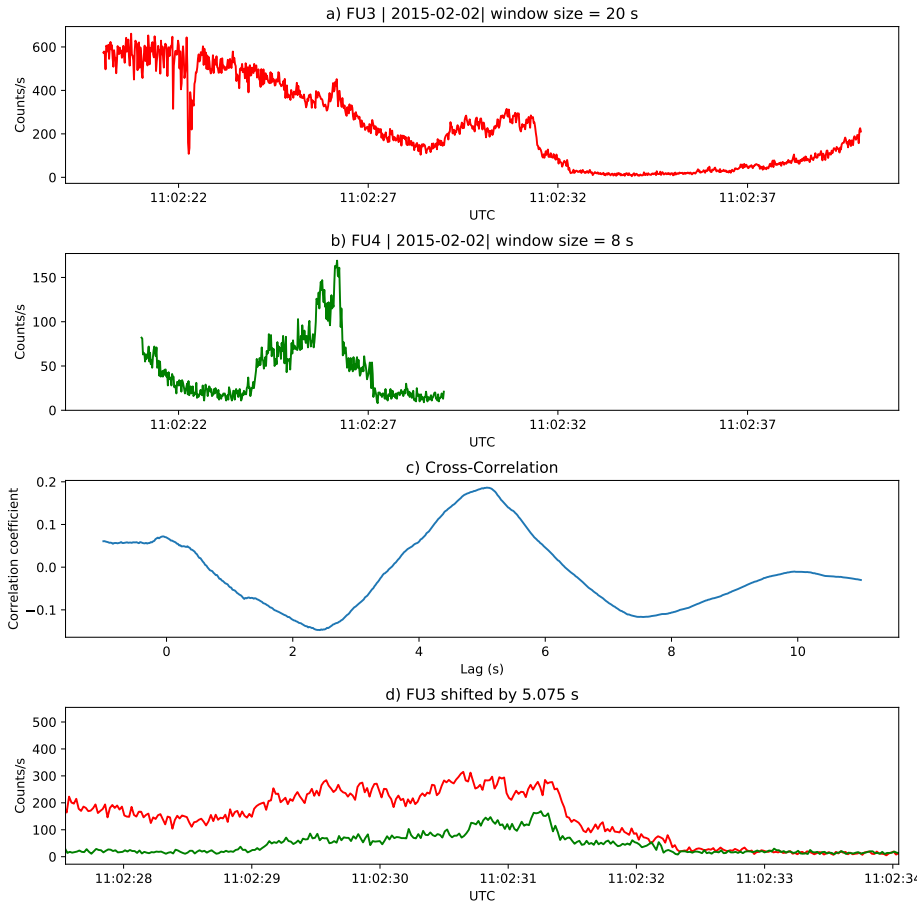


Figure B.6: Same analysis as Fig. B.5 applied to a different stationary spatial feature. The lag derived at this time was 5.01 s.

2374 This appendix contains texts S1-S3. Text S1 derives the analytic model that
2375 transforms a prescribed microburst PDF into a \bar{F} curve as a function of AC6
2376 separation, s . Text S2 expands on the two-sized microburst model results presented
2377 in Section 5.3 and the range of optimal model parameters assuming continuous
2378 microburst PDFs such as the log-normal, Weibull, and Maxwellian. Lastly, text
2379 S3 presents the percent of microbursts observed in each separation bin, as a function
2380 of separation and compares it to the observed scale size of chorus waves as a function
2381 of wave amplitude.

2382 **Text S1: Analytic Derivation of $\bar{F}(s)$** Here we derive the integral form of $\bar{F}(s)$
2383 under the following assumptions:

- 2384 1. microbursts are circular with radius r
2385 2. microbursts are randomly and uniformly distributed around AC6.

First recall the area $A(r, s)$, given in Eq. 4 in the main text and copied here for convenience

$$A(r, s) = 2r^2 \cos^{-1} \left(\frac{s}{2r} \right) - \frac{s}{2} \sqrt{4r^2 - s^2}. \quad (\text{C.1})$$

2386 A circular microburst who's center lies in $A(r, s)$ will be observed by both AC6 units
2387 and is counted in $\bar{F}(s)$. Now we derive the integral form of $\bar{F}(s)$ that accounts for
2388 the different spacecraft separations and microburst sizes that are distributed by a
2389 hypothesized PDF $p(r, \theta)$.

2390 First we will account for the effects of various spacecraft separation, assuming all
2391 microbursts are one size. For reference choose of radius, r_0 and spacecraft separation,
2392 s_0 such that $A(r_0, s_0) > 0$ which implies that some number of microbursts, n_0 will be
2393 simultaneously observed. Now, if for example the spacecraft separation (or microburst
2394 radius) is changed such that the area doubles, the second assumption implies that the
2395 number of microbursts observed during the same time interval must double as well.
2396 This can be expressed as

$$\frac{n_0}{A(r_0, s_0)} = \frac{n}{A(r, s)} \quad (\text{C.2})$$

2397 and interpreted as the conservation of the microburst area density. By rewriting Eq.
2398 C.2 as

$$n(r, s) = \left(\frac{n_0}{A(r_0, s_0)} \right) A(r, s) \quad (\text{C.3})$$

2399 it is more clear that the number of microbursts of size r observed at separation s is
2400 just $A(r, s)$ scaled by the reference microburst area density. The cumulative number
2401 of microbursts observed above s is then

$$N(r, s) = \int_s^\infty n(r, s') ds' = \left(\frac{n_0}{A(r_0, s_0)} \right) \int_s^\infty A(r, s') ds'. \quad (\text{C.4})$$

2402 Lastly, $\bar{F}(s)$ for a single r is then

$$\bar{F}(s) = \frac{N(s)}{N(0)} = \frac{\int_s^\infty A(r, s') ds'}{\int_0^\infty A(r, s') ds'} \quad (\text{C.5})$$

2403 To incorporate a continuous microburst PDF such as $p(r) = p_1\delta(r - r_1) + p_2\delta(r -$
2404 $r_2) + \dots$ we sum up the weighted number of microbursts that each size contributes to

₂₄₀₅ $N(s)$ i.e.

$$N(s) = \left(\frac{n_0}{A(r_0, s_0)} \right) \left(\int_s^\infty p_1 A(r_1, s') ds' + \int_s^\infty p_2 A(r_2, s') ds' + \dots \right) \quad (\text{C.6})$$

₂₄₀₆ The last step is to convert the sum of Dirac Delta functions into a continuous
₂₄₀₇ PDF $p(r)$ after which

$$N(s) = \left(\frac{n_0}{A(r_0, s_0)} \right) \int_s^\infty \int_0^\infty A(r, s') p(r) dr ds'. \quad (\text{C.7})$$

₂₄₀₈ With these considerations, $\bar{F}(s)$ is then given by

$$\bar{F}(s, \theta) = \frac{\int_s^\infty \int_0^\infty A(r, s') p(r, \theta) dr ds'}{\int_0^\infty \int_0^\infty A(r, s') p(r, \theta) dr ds'} \quad (\text{C.8})$$

Text S2: Most probable parameter values for continuous microburst PDFs

Besides the one and two-size microburst models described in the main text, continuous PDFs such as the log-normal, Weibull, and Maxwellian were fit and their optimal parameters presented here.

For the Maxwellian PDF, we assumed the following form

$$p(r|a) = \sqrt{\frac{2}{\pi}} \frac{r^2 e^{-r^2/(2a^2)}}{a^3}. \quad (\text{C.9})$$

The range of a consistent with the observed data was found to be between 0 and 35 km. Next, the log-normal distribution of the following form was used

$$p(r|\mu, \sigma) = \frac{1}{\sigma r \sqrt{2\pi}} e^{\left(-\left(\ln(r) - \ln(\mu)\right)^2 / (2\sigma^2)\right)} \quad (\text{C.10})$$

and the results are summarized in C.1. Lastly the Weibull distribution of the following form was tested

$$p(r|c, r_0, \lambda) = c \left(\frac{r - r_0}{\lambda} \right)^{c-1} \exp \left(- \left(\frac{r - r_0}{\lambda} \right)^c \right). \quad (\text{C.11})$$

for which the model parameters are summarized in Table C.2.

Table C.1: Range of log-normal model parameters consistent with the observed AC6 $\bar{F}(s)$

percentile (%)	μ	σ
2.5	1.8	0
50	21.8	0.4
97.5	52.0	1.1

Table C.2: Range of Weibull model parameters consistent with the observed AC6 $\bar{F}(s)$

percentile (%)	c	r_0	λ
2.5	0.6	1.3	2.7
50	5.5	26.2	32
97.5	19.3	72.5	72.2

2415 **Text S3: Comparison of microburst to whistler mode chorus $\bar{F}(s)$**
2416 **TBD**